Corrosion Behavior in Friction Stir Processed Austenitic Stainless Steel

A Thesis

Presented in Partial Fulfilment of the Requirements for the

Degree of Master of Science

with a

Major in Nuclear Engineering

in the

College of Graduate Studies

University of Idaho

by

David Zirker

Major Professor: Indrajit Charit, Ph.D.

Committee Members:

Krishnan Raja, Ph.D.; Amin Mirkouei, Ph.D.; Michael McMurtrey, Ph.D

Department Administrator: Indrajit Charit, Ph.D.

August 2023

Abstract

Chloride induced stress corrosion cracking (CISCC) is particularly deleterious to 300 series stainless steels. Examples of CISCC have been reported on the surfaces of Type 304, 304L, and 316L stainless steel components in a variety of environments where chloride is present. Localized pitting generally precedes CISCC, and therefore improving the pitting resistance of a material generally improves resistance to CISCC. Friction stir processing is a proposed technique to repair and mitigate material chloride induced stress cracks by adding molybdenum to the base material. Molybdenum improves pitting resistance and that is why it is used in this study. Friction stir processed samples were made by adding 316L and molybdenum powder to 304L stainless steel via friction stir processing. By using electrochemical techniques, an evaluation of the friction stir processed samples was performed to evaluate corrosion resistant qualities of the material. Cyclic polarization results suggests that the addition of the molybdenum through FSP was not beneficial to pitting resistance of the samples. The FSP 304L sample had a pitting potential around 0.3342 V whereas the FSP 304L+Mo sample only had a pitting potential of around 0.2872 V. Friction stir processing was beneficial in decreasing the corrosion current and in the case of the FSP 304L+Mo increasing the linear polarization significantly. U-bend samples were also made and tested in an open circuit potential and a 0.2 V static potential. The FSP 304L+316L and FSP 304L+Mo were more noble than the 304L in the open circuit potential analysis and did not fail in the U-bend test yet the surface crack density was higher in the FSP samples. The experiment was terminated at 2472 hours and the FSP 304L+316L and FSP 304L+Mo were removed from the 2.5 M sulfuric acid + 0.5 M sodium chloride solution with no failure. By contrast, the 304L base U-bend sample had a low surface crack density yet failed at 267.5 hours. The potentiostatic analysis revealed that the FSP 304L+Mo sample had improved passivation kinetics.

Acknowledgements

This work was made possible because of the help and support of many individuals, both professional and personal, government agencies, and academic entities. I wish to acknowledge the Nuclear Energy University Programs for providing funding (project DE-NE0008776) for much of the research performed in this thesis. I would like to thank the members of my committee Dr. Krishnan Raja, Dr. Amin Mirkouei, and Dr. Michael McMurtrey. They have been instrumental in guiding me with actions and words to explore and become a better scientist. I would like to acknowlede Dr. Indrajit Charit for his willingness to take me on as one of his students and thank him for being an example of what it means to be a scientist. This journey was made possible because of Dr. Charit and I will always be grateful of what I learned from him. I would like to thank Dr. Saumyadeep Jana for his help with the friction stir welding/processing runs performed at the Pacific Northwest National Laboratory. I wish to acknowledge the Idaho Department of Commerce (IGEM-Commerce Grant #5358) for funding my graduate research assistantship the last year of my education and Idaho Strategic Resources Inc. (IDR) for their resources and support. There are many individuals who helped with the technical minutia of this project and without their help, this project would have not risen to its full potential. To acknowledge them all would be impossible but I would like to highlight a few that added a something special to this thesis. Bryan Forsmann and Arvin Cunningham from the Idaho National Laboratory who came to my rescue when things didn't work the way I had hoped and Mark "the machinist" Deveraux who took my rough drawings and turned them into beautiful samples. Finally, I would like to acknowledge my dad. Larry Zirker, for talking me through some of the hard days and helping me "see" through the problem.

Dedication

To Lindsey, my wife is the reason that I was able to finish this thesis and deserves praise for supporting me through this temporary insanity.

Contents

List of Figures

List of Tables

CHAPTER 1

Introduction

The Nuclear Regulatory Commission has identified chloride-induced stress corrosion cracking (CISCC) of austenitic stainless steel dry cask storage systems (DCSS) as an area of great concern. Dry storage systems are used for long-term storage of spent nuclear fuels (SNF). The storage systems consist of stainless steel (SS) cylindrical canisters encased in a concrete over pack The canister is fabricated using either AISI 304/304L type or 316/316L type austenitic stainless steel. The DCSS have passive cooling capabilities that remove decay heat from the SNF but chloride salts carried by the dust will deliquesce on the surface of the canister and attack the steel corrosively through pitting and (CISCC). CISCC reduces the life of these DCSS significantly and poses a threat of accidental breach of containment and release of radioactive waste products. This thesis discusses as a solution to CISCC using a friction stir repair technique that repairs and strengthens 300 series steel effected by CISCC. This technique uses friction stir processing (FSP) to heal the crack and add elements resistant to CISCC. Molybdenum will be added to 304L via FSP and then tested using eletro-chemical techniques to compare its corrosion resistance to the 304L base metal.

1.1 Thesis Outline

This thesis will be organized into three major sections

1. Background and Literature Review

2. Cyclic Polarization of Friction Stir Alloyed Austenitic Stainless Steel

3. U-bend Analysis of Friction Stir Alloyed Austenitic Stainless Steel

Background and Literature Review This section will expound on the problem and the techniques used to solve the problem

Cyclic Polarization of Friction Stir Alloyed Austenitic Stainless Steel This section will use the electro-chemical technique of cyclic polarization to highlight and compare the material characteristics that make up corrosion resistance

U-bend Analysis of Friction Stir Alloyed Austenitic Stainless Steel This section will use U-bend samples in open circuit potential and static potential to test the materials resistance to CISCC

1.2 Objectives

The objectives of this thesis research are as summarized below.

1. Understand the pitting resistance effects of adding molybdenum and 316L via friction stir processing.

2. Understand the CISCC resistance effect of adding molybdenum and 316L via friction stir processing.

CHAPTER 2

Background and Literature Review

2.1 Introduction

In the late 1970's, as wet storage of spent nuclear fuel began to reach capacity, the need for additional storage capability became apparent. Storage pools cannot be enlarged because of the risk of compromising the structural integrity of the containment and so the Nuclear Regulatory Commission (NRC) has allowed that spent nuclear fuel (SNF) be stored out of wet storage in dry storage casks. There are two styles of dry fuel storage used in the United States at this time, Dual-Purpose Canister (DPC) systems and Bare fuel Cask storage systems. DPC's are the most common type in the United States with about 92% of SNF being stored in this type of system [1]. Dry storage of SNF is an essential part of the US nuclear program, yet there are some risks associated with the integrity of the casks where research is lacking. The NRC has identified chloride-induced stress corrosion cracking (CISCC) of the stainless steel components of the cask as an area of great concern. Chloride salts in the air are deposited on the surface of the austenitic stainless steel canister during the cooling process. As the chloride salts deliquesce, the chloride induces corrosion attacks such as pitting and CISCC. These attacks threaten the integrity of the dry storage systems and risk breach of containment.

2.2 Dry Storage Casks

When SNF is removed from a reactor, it is placed into cooling pools to remove residual from nuclear fission. Once the SNF has cooled sufficiently in wet storage, the fuel

assemblies are placed in a borated aluminum baskets or "egg-crate" as can be seen in in Figure 2.1. The design of the basket separates the fuel assemblies and aids in excess heat removal. Once full, the basket is placed inside a steel canister and the interstitial spaces are filled with an inert gas. The use of an inert gas is critical to minimize the corrosive environment within the canister. Helium is generally used because of its heat capacity but nitrogen has also been used. The steel canister is then sealed shut with bolts or by welding [2].

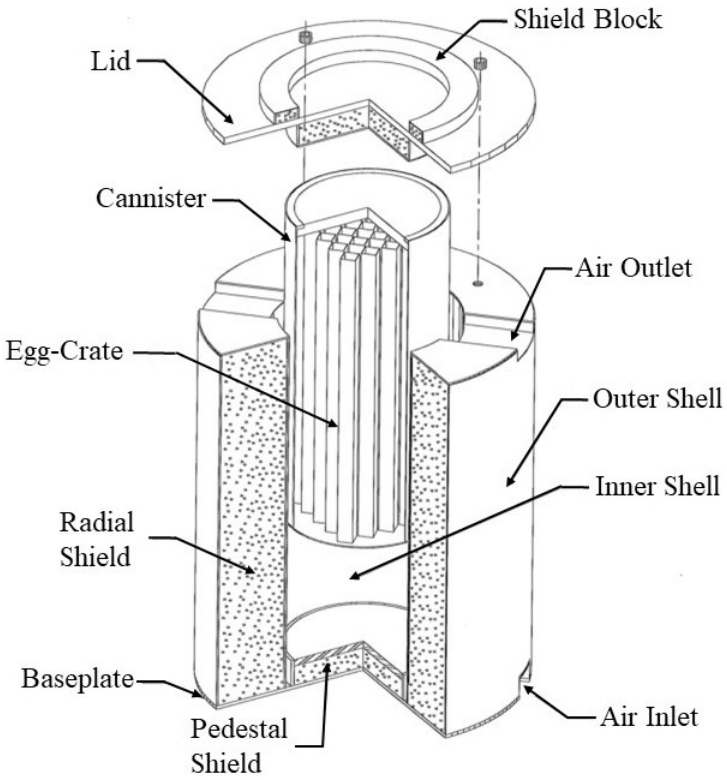

Figure 2.1: Example of a free-standing upright design of a dry storage cask with air inlets and outlets [3]

After being sealed the inner canister is placed inside a concrete and steel storage cask, or overpack, with an air gap between the steel canister and the overpack, as can be seen in Figure 2.2. James D. Werner in his CRS report for congress stated that "as of December 2011, more than 67,000 metric tons of [spent nuclear fuel] in

more than 174,000 assemblies, is stored at 77 sites (including 4 Department of Energy (DOE) facilities) in the United States located in 35 states" [4]. Approximately 27% of the SNF is stored in some form of dry storage cask, whether on concrete pads above ground or in a vault. Convective airflow in the air gap, caused by the thermal gradient due to decay heat and air inlets and outlets ducts cools the air gap between the steel canister and the overpack. This feature of cooling the storage cask without power makes it passively safe [4] but outside air that contains chloride salts is allowed to deposit salts on the surface of the canister. These salts create a corrosive environment which threaten the integrity of the containment.

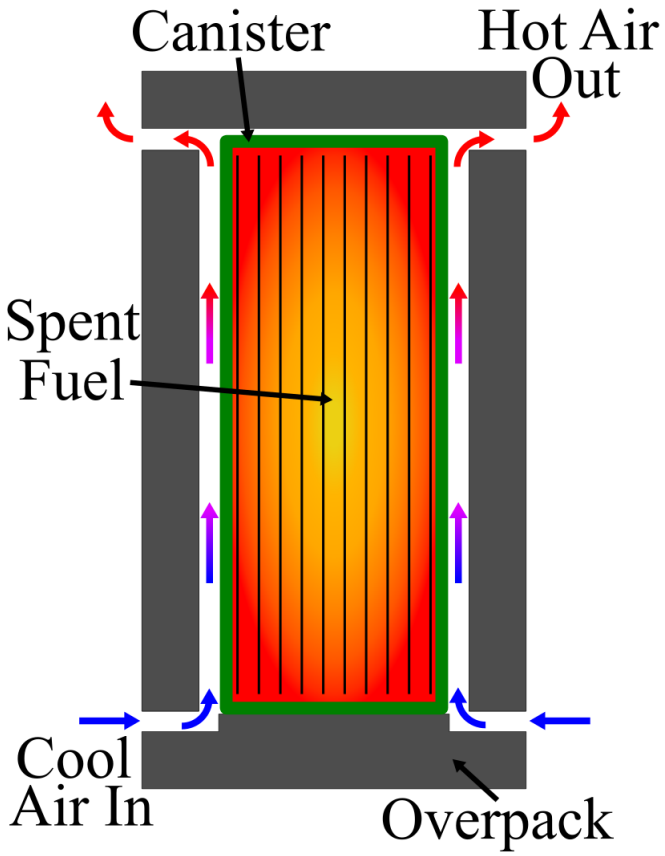

Figure 2.2: A cross-section of a DPC that highlights the passive cooling system. Adapted from [1]

2.3 Chloride Induced Stress Corrosion Cracking

Chloride induced stress-corrosion cracking (CISCC), is one process by which the integrity of the cask is threatened. CISCC is a corrosion mechanism in which the initiation and growth of cracks is exacerbated in a chloride-dominated corrosive environment, generally due to chlorine salts. The cracking typically develops following the formation and growth of corrosive pits [5][6]. Stress corrosion cracks are microscopic in early stages of development which makes it difficult to identify without the use of special techniques. In 300 series stainless steel crack nucleation is heavily environment dependant [7] [8] [9]. CISCC can manifest as intergranular or transgranular depending on the material or environment. Mayuzumi et al observed that austenitic steel that has been sensitized will nucleate intergranular cracks at ambient temperatures but if the temperature is increased past 54 °C then transgranular cracking will form [10]. For CISCC to occur, three conditions are generally required

1. A corrosive environment.
2. A material that is vulnerable to CISCC.
3. The material must be subjected to tensile stresses.

Corrosive Environment Because of the passive cooling features in a DCSS, the steel canister is in direct contact with the atmosphere. The air that cools the DCSS also contains salt particles, which are deposited on the surface of the steel [10]. Depending on temperature and humidity [11] the salt deposits will deliquesce and create an aqueous chloride solution. Water is an essential component of CISCC and if absent CISCC cannot be sustained [12]. Aqueous chloride solutions induces pit nucleation because the chloride ions encourage passive layer break down by stimulating the oxidation reaction [13] which causes dissolution of metal.

$$M \rightarrow M^{+} + e^{-} \tag{2.1}$$

Because chloride ions are so mobile in solution, they migrate to any area where metal dissolution is high to balance the excess positive charge. This concentration of metal ions and chloride ions creates insoluble metal hydroxide and free acid.

$$M^{+}Cl^{-} + H_2O = MOH + H^{+}Cl^{-} \tag{2.2}$$

As chloride ions concentrate to areas with high concentrations of metal ions this can create a localized area of corrosion called a pit. Pitting corrosion is an extremely localized form of corrosion that causes a hole or cavity in the metal as shown in Figure 2.3. It is particularly deleterious to structural integrity because it can cause failure with only a small percentage of mass loss. As pits nucleate they create an autocatalytic process that perpetuates and exacerbates corrosion damage by depleting the pit of oxygen which inhibits the reduction reaction shown in Equation. 2.3 [13] [14]. The reduction reaction continues on the surface of the metal and suppresses corrosion of the base metal surface.

$$O_2 + 2H_2O + 4e^{-} \rightarrow 4OH^{-} \tag{2.3}$$

$$2Cr + H_2O \rightarrow Cr_2O_3 + 6H^{+} + 6e^{-} \tag{2.4}$$

Despite this depletion of oxygen in the newly formed pit, the oxidation reaction, Equation. 2.1, and hydrolysis reaction, Equation. 2.2, still continue. It is this autocatalytic behavior that encourages pit growth. The pit creates a stress riser on the surface of the metal which encourages the formation of cracks, and exacerbates the

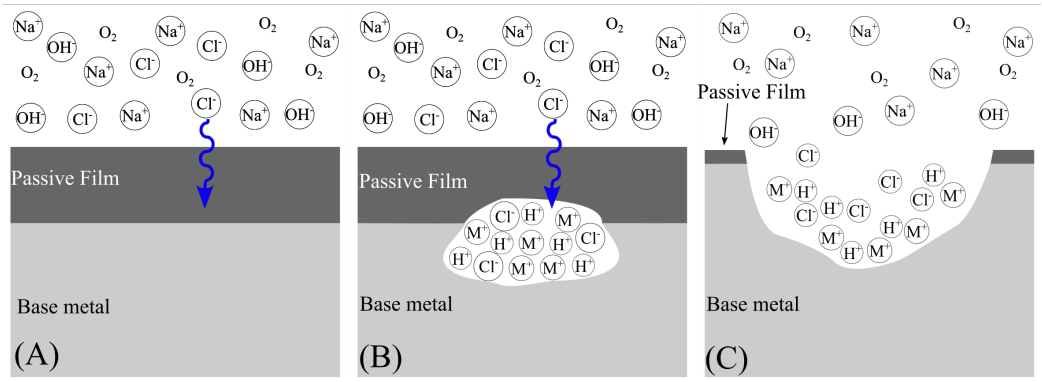

Figure 2.3: (A) Chloride ions are attracted to the metal ions being dissolved and are able to exploit defects in the passive layer; (B) The chloride ions accelerates the oxidation and hydrolysis reaction creating a small pocket between the passive layer and the bare metal; (C) This small pocket becomes autocatalytic and grows in size

production of free acid as shown in Figure 2.4. Once the internal stresses are sufficient for a crack to form, it reveals bare metal free of any passive layer. This combined with the anodic oxidation of chromium into chromium oxide which promotes a buildup of acidity at the tip of the crack, encourages the crack to grow [12].

Material Vulnerable to CISCC 300 series stainless steels are particularly susceptible to CISCC in chloride environments. This may be because the protective passive layer common in stainless steels protects the majority of the surface but the slightest defect in the surface of the passive layer like an inclusions, tramp elements, or a slip step can begin the autocatalytic effect of pit corrosion [15]. Examples of CISCC have been reported on the surfaces of Type 304, 304L, and 316L stainless steel components in chemical reactor vessels, urea plant vessels, rock climbing equipment, and at nuclear power plants [16]. Although some localized pitting or crevice corrosion generally precedes CISCC, the amount of pitting or crevice attack may be so small as to be undetectable. stress corrosion is difficult to detect while in progress, even when pervasive and can lead to rapid catastrophic failure of pressurized equipment. The addition of molybdenum in austenitic stainless steel have been shown to

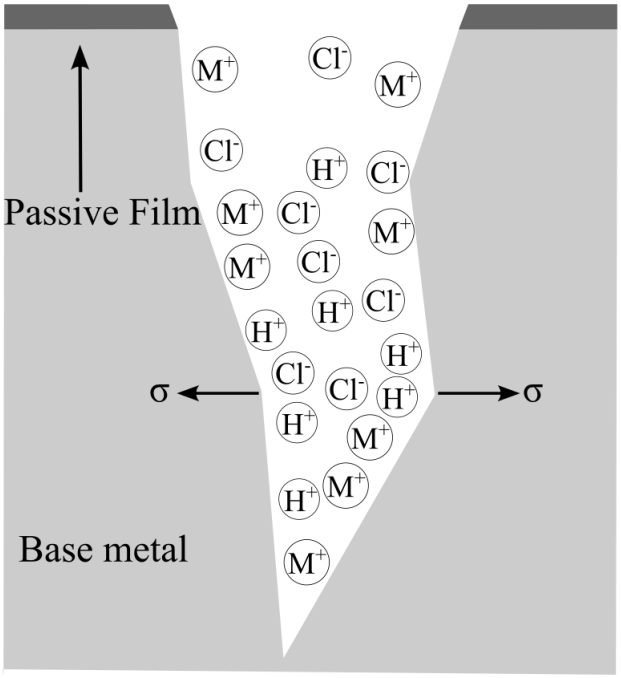

Figure 2.4: As the pit continues to grow the stress riser induces a crack. The confined volume of the crack tip encourages the anodic reaction Equation. 2.4 further accelerating crack growth

improve corrosion resistance [17][18][19][8].

The use of materials resistant to CISCC could be used in future designs of casks to mitigate the effects of CISCC. Research shows that materials with increased resistance to pitting are more suitable for environments that encourage CISCC [5][10][12]. This resistance can be described with the pitting resistance equivalent number (PREN) [20].

$$PREN = \%wtCr + 3.3 \times (\%wtMo + 0.5\%wtW) + 16 \times \%wtN \tag{2.5}$$

The larger the PREN the better a specific steel will be at resisting pit nucleation. From Equation. 2.5 we see that additions of chromium, molybdenum, tungsten and nitrogen will increase the resistance to pitting. Research performed by Mayuzumi et

al provides evidence that stainless steel alloys with higher amounts of PREN elements have improved resistance to pitting as shown in Figure 2.5. The pitting potentials of UNS S31260 and UNS S31254 stainless steels were much higher than that of UNS S30403 or UNS S31603. UNS S31260 and UNS S31254 have more chromium, molybdenum, tungsten and nitrogen compared with UNS S30403 or UNS S31603. UNS S31603. UNS S31260 performed better than UNS S30403 and UNS S31260 against CISCC, Therefore, it was concluded that the superior CISCC resistance is attributable to the higher resistance to pitting corrosion of UNS S31260 and UNS S31254 SS [10]. We can theorize that the increased resistance to pitting corrosion is attributed to increased levels of chromium, molybdenum, tungsten and nitrogen, which increases the PREN of the material [17][18].

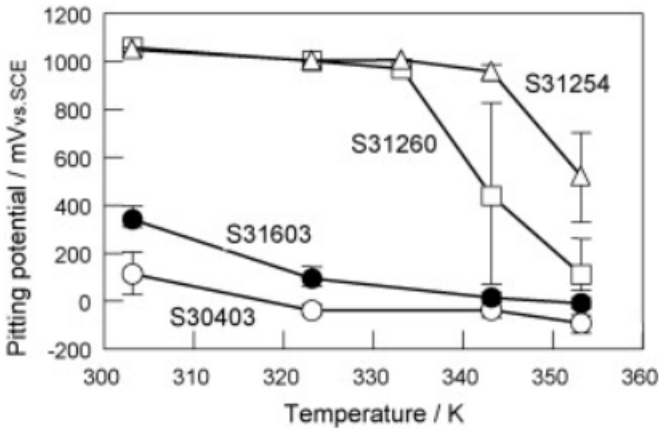

Figure 2.5: The pitting potentials of UNS S31260 and UNS S31254 SS [10]

Research also indicates that CISCC is initiated by breakdown of the passive film on the surface by emerging slip steps. Stacking fault energy of the stainless steel plays a vital role in the CISCC resistance. If slip planes are spaced widely apart as determined by a low stacking fault energy (normally observed in 304 SS), the slip step is sufficient to break the passive film completely and expose bare metal surface which leads to oxidative dissolution as schematically illustrated in Figure 2.6. (a) and (b).

The dissolution of bare metal exposed by passive film breakdown is considered to be a rate determining step in the CISCC process [19]. When the stacking fault energy is high, the slip planes are closely spaced due to cross-slip which leads to emergence of finer slip steps as depicted in Figure 2.6 (c). The fine slip steps are not sufficient to cause a complete breakdown of the passive film and therefore, no bare metal is exposed. This process may delay occurrence of the SCC. Addition of boron, nitrogen, and molybdenum could increase the stacking fault energy [21].

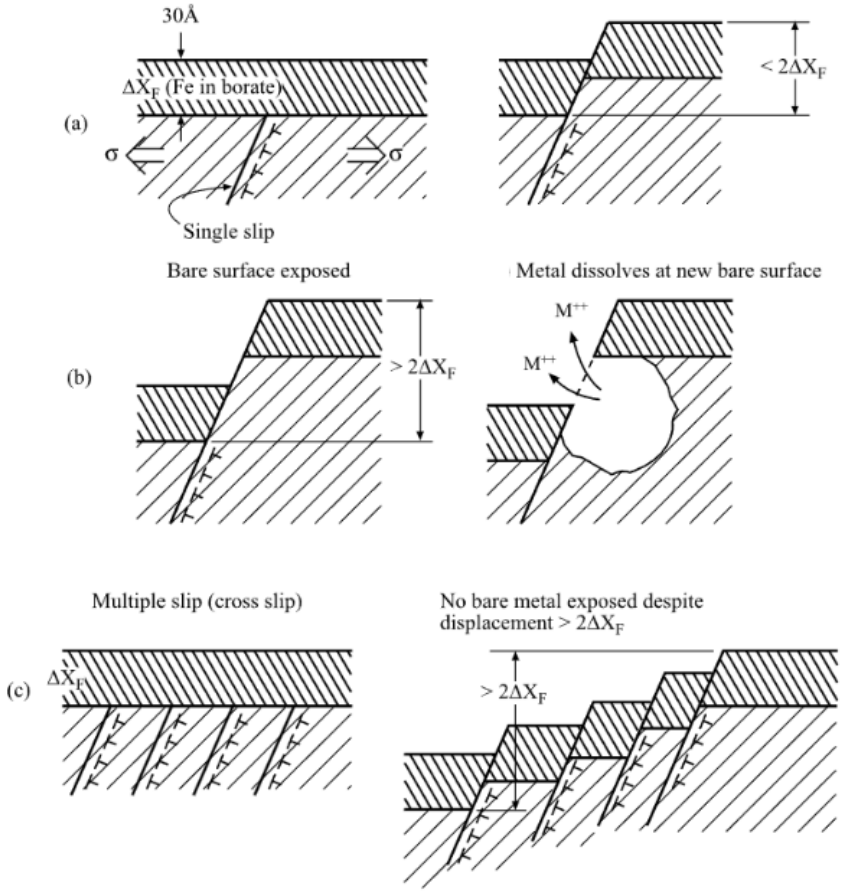

Figure 2.6: Relation between stacking fault energy – slip step and passivity break down. Low stacking fault energy results in widely spaced slip planes and increased slip steps that cause complete breakdown of passive film exposing bare metal surface as depicted in (a) and (b). High stacking fault energy promotes cross slip (c) and smaller slip steps (bottom right) that are not sufficient to cause complete breakdown of the passive film and do not expose the bare metal surface [19].

Internal Stresses There can be no CISCC if there is no stress within the material. The stress state of the canister, particularly in the weld and the weld heat affected zone (HAZ), where tensile stress in the canisters are expected to be the most pronounced, can have an adverse effect on the materials resistance to CISCC [5][11][16][22]. Research has shown that when conventional fussion welding is used, weld toe has the most amount of stresses in the proximity of the weld and can be seen in Figure 2.7[23]. The residual stresses from welding are likely sufficient for CISCC [24]

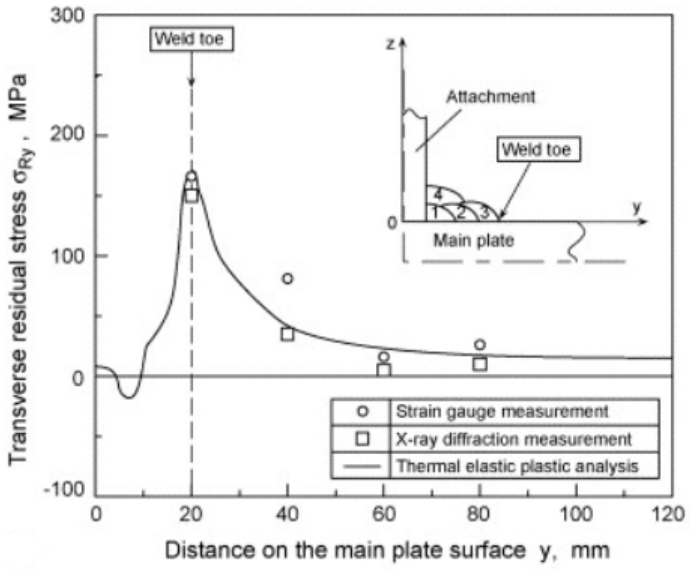

Figure 2.7: Transverse residual stress on the main plate surface in a fillet joint type weld. Note that the peak stress in the weld is located at the weld toe [23].

High stresses in the weld toe, alloying element segregation, and chromium depleted zones degrade the corrosion resistance of the material [25] and encourage CISCC.

2.4 Friction Stir Alloying

Friction stir welding (FSW) is a solid-state joining process that uses frictional heat and severe plastic deformation to weld two pieces of material together without melting

the material. This technique was invented and patented in 1991 by The Welding Institute (TWI) in the UK [26].

In FSW, a rotating tool with a non-consumable pin is inserted into the material joint, and the tool is moved along the joint line, as seen in Figure 2.8. The frictional heat generated by the tool softens the material and causes it to become plastically deformed, allowing the two pieces to be joined together [27]. The tool also stirs the material, producing a mixing effect that helps to homogenize the microstructure of the joint and eliminate defects such as voids and porosity.

FSW is commonly used to join materials that are difficult to weld by traditional fusion welding techniques, such as aluminum alloys, magnesium alloys, and copper alloys. It is also used in applications where the welded joint must have high strength and good fatigue resistance, such as in aerospace, automotive, and marine industries. FSW has many advantages over traditional welding techniques, including lower distortion, reduced porosity, a narrower heat-affected zone, and improved microstructure [27].

Welding parameters like tool rotation rate (ω), traverse speed (ν), and tool tilt are critical to achieving a mechanically sound weld. Tool rotation generates the friction required to heat the material and the mixing of parent material. By changing the rotation rate the intensity of mixing and stirring can be controlled. Traverse speed controls the method that mixed material is moved from the front of the tool to the rear of the tool. Tool tilt changes how the shoulders are engaged and the degree of mixing that occurs on the top surface of the weld [27].

Friction stir techniques are ideal for DPC's because it introduces significantly less stress than conventional joining techniques [27] [28]. Friction stir alloying (FSA) is a

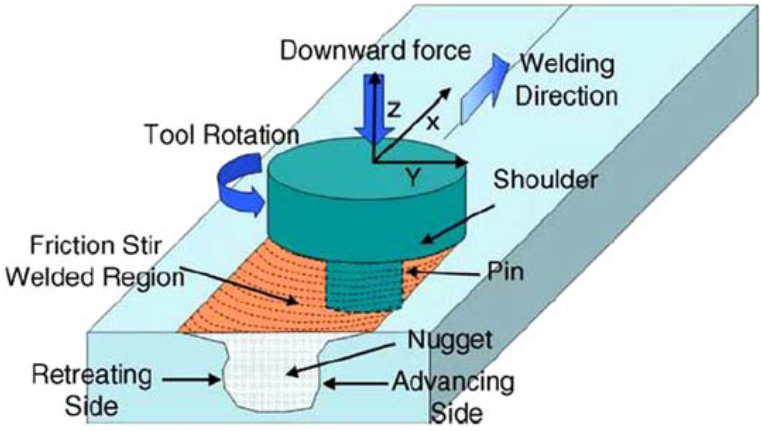

Figure 2.8: Friction stir welding process [27]

solid-state processing technique that uses frictional heat and mechanical deformation to introduce an alloying element into the surface layer of a base material. This process is similar to friction stir welding, but instead of joining two pieces of material together, it modifies the surface layer of a single material.

In FSA, a rotating tool with an alloying element is inserted into the surface of the base material, and the tool is moved along the surface. The frictional heat generated by the tool softens the material and causes it to become plastically deformed, allowing the alloying element to be mixed into the surface layer of the base material. The tool also stirs the material, producing a mixing effect that helps to homogenize the microstructure of the modified surface layer.

FSA is commonly used to improve the surface properties of materials, such as wear resistance, corrosion resistance, and hardness. It can also be used to tailor the surface properties of a material to a specific application, such as introducing a biocompatible layer on a medical implant. FSA has many advantages over traditional surface modification techniques, including a lower processing temperature, reduced distortion, and a more uniform distribution of the alloying element.

2.5 Ball Milling

Ball milling is a process where different elements, often in powder form, are mechanically alloyed to form homogeneous mixtures with custom elemental contents. combined in a vessel called a vial. The vial is filled with a grinding media, balls made from materials like 52100 steel (Figure 2.9), alumina, tungsten carbide, or agate to name a few, and the sample elements that are intended for milling. During the ball

Figure 2.9: Ball mill vial[29]

milling process, the grinding media and the material to be ground are placed inside the vial and are subjected to high-energy collisions caused by the rotating motion of the mill. These collisions result in the reduction of the particle size of the material, as well as the deformation and fracturing of the particles. The duration and intensity of the milling process can be adjusted to achieve the desired particle size and morphology.

Ball milling can be used to produce a wide range of powders, including metal powders, ceramic powders, and composite powders. It is an effective method for producing powders with a narrow size distribution and a high degree of homogeneity, which is important in many applications of powdered metallurgy.

Bibliography

[1] EJ Bonano. "Spent Nuclear Fuel Storage R&D at Sandia National Laboratories". Feb. 7, 2019. URL: https://www.osti.gov/servlets/purl/1598436.

[2] Moamen G. El-Samrah, A. F. Tawfic, and Samir E. Chidiac. "Spent nuclear fuel interim dry storage; Design requirements, most common methods, and evolution: A review". In: *Annals of Nuclear Energy* 160 (Sept. 15, 2021), p. 108408. ISSN: 0306-4549. DOI: 10.1016/j.anucene.2021.108408.

[3] *Holtec International Final Safety Analysis Report for the HI-STORM 100 Cask System*. Safety Report HI-2002444. Holtec International, Mar. 31, 2016. URL: https://www.nrc.gov/docs/ML1613/ML16138A100.pdf.

[4] James D Werner. "U.S. Spent Nuclear Fuel Storage". In: *Congressional Research Service* (R42513 May 24, 2012).

[5] Lloyd Hackel et al. "Preventing Stress Corrosion Cracking of Spent Nuclear Fuel Dry Storage Canisters". In: *Procedia Structural Integrity*. Fatigue Design 2019, International Conference on Fatigue Design, 8th Edition 19 (Jan. 1, 2019), pp. 346–361. ISSN: 2452-3216. DOI: 10.1016/j.prostr.2019.12.038. URL: https://www.sciencedirect.com/science/article/pii/S2452321619305062 (visited on 09/28/2022).

[6] Kristina L. Banovac. *Summary Of August 5, 2014, Public Meeting With The Nuclear Energy Institute On Chloride Induced Stress Corrosion Cracking Regulatory Issue Resolution Protocol*. NRC, Sept. 2014. URL: https://www.nrc.gov/docs/ML1425/ML14258A081.pdf.

[7] Longkui Zhu. "Probing intergranular mixed transgranular stress corrosion cracking under the high constant load". In: *Scientific Reports* 12.1 (July 20, 2022).

Number: 1 Publisher: Nature Publishing Group, p. 12390. ISSN: 2045-2322. DOI: 10.1038/s41598-022-16390-1. URL: https://www.nature.com/articles/s41598-022-16390-1 (visited on 07/14/2023).

[8] H Fujikawa and N Maruyama. "Corrosion behaviour of austenitic stainless steels in the high chloride-containing environment". In: *Materials Science and Engineering: A*. Proceedings of the 2nd International symposium on High Temperature Corrosion of Advanced Materials and Coatings 120-121 (Nov. 15, 1989), pp. 301–306. ISSN: 0921-5093. DOI: 10.1016/0921-5093(89)90754-5. (Visited on 04/12/2023).

[9] NACE International. *NACE Basic Corrosion Course*. 12th. NACE, 1982. 448 pp.

[10] M. Mayuzumi, J. Tani, and T. Arai. "Chloride induced stress corrosion cracking of candidate canister materials for dry storage of spent fuel". In: *Nuclear Engineering and Design*. Concrete Cask Storage of Spent Fuel -Challenge of Economic Storage Technology 238.5 (May 1, 2008), pp. 1227–1232. ISSN: 0029-5493. DOI: 10.1016/j.nucengdes.2007.03.038. URL: https://www.sciencedirect.com/science/article/pii/S0029549307002518 (visited on 11/09/2022).

[11] L. Caseres and T.S. Mintz. "NUREG/CR-7030, "Atmospheric Stress Corrosion Cracking Susceptibility of Welded and Unwelded 304, 304L, and 316L Austenitic Stainless Steels Commonly Used for Dry Cask Storage Containers Exposed to Marine Environments."" In: (Oct. 2010), p. 90.

[12] P. R. Rhodes. "Mechanism of Chloride Stress Corrosion Cracking of Austenitic Stainless Steels". In: *Corrosion* 25.11 (Nov. 1, 1969), pp. 462–472. ISSN: 1938-159X, 0010-9312. DOI: 10.5006/0010-9312-25.11.462. URL: https://meridian.allenpress.com/corrosion/article/25/11/462/158324/

Mechanism - of - Chloride - Stress - Corrosion - Cracking - of (visited on 04/12/2023).

[13] Mars G. Fontana. *Corrosion Engineering*. 3rd edition. New York: McGraw-Hill Book Company, Nov. 1, 1985. 556 pp. ISBN: 978-0-07-021463-7.

[14] Robert Kelly. "Passivity and Localized Corrosion". In: Robert Kelly et al. *Electrochemical Techniques in Corrosion Science and Engineering*. Series Title: Corrosion Technology. CRC Press, Sept. 13, 2002. ISBN: 978-0-203-90913-3. DOI: 10.1201/9780203909133.ch3. (Visited on 05/02/2023).

[15] U. R. Evans. "Stress Corrosion: Its Relation to Other Types of Corrosion". In: *CORROSION* 7.7 (July 1951), pp. 238–244. ISSN: 0010-9312, 1938-159X. DOI: 10.5006/0010-9312-7.7.238. URL: http://corrosionjournal.org/doi/10.5006/0010-9312-7.7.238 (visited on 05/17/2023).

[16] Tae M Ahn, Greg Oberson, and Sara DePaula. "Chloride-Induced Stress Corrosion Cracking of Austenitic Stainless Steel Used for Dry Storage of Spent Nuclear Fuel". In: *ECS Transactions* 50.31 (May 1, 2013), pp. 211–226. ISSN: 1938-5862, 1938-6737. DOI: 10.1149/05031.0211ecst. URL: https://iopscience.iop.org/article/10.1149/05031.0211ecst (visited on 09/28/2022).

[17] K. Sugimoto and Y. Sawada. "The role of molybdenum additions to austenitic stainless steels in the inhibition of pitting in acid chloride solutions". In: *Corrosion Science* 17.5 (Jan. 1977), pp. 425–445. ISSN: 0010938X. DOI: 10.1016/0010-938X(77)90032-4.

[18] M. A. Streicher. "Pitting Corrosion of 18Cr-8Ni Stainless Steel". In: *Journal of The Electrochemical Society* 103.7 (1956), p. 375. ISSN: 00134651. DOI: 10.

1149/1.2430359. URL: https://iopscience.iop.org/article/10.1149/1.2430359 (visited on 05/02/2023).

[19] Roger W. Staehle. "Transient stability of passive films in aqueous solutions". In: *Corrosion Science*. Progress in Corrosion Research in Commemoration of Centenary of Birth of Professor Go Okamoto 49.1 (Jan. 1, 2007), pp. 7–19. ISSN: 0010-938X. DOI: 10.1016/j.corsci.2006.05.006. URL: https://www.sciencedirect.com/science/article/pii/S0010938X06001144 (visited on 11/09/2022).

[20] Scott D Cramer and Bernard S. Covino. *ASM Handbook Volume 13B, Corrosion: Materials - ASM International*. Nov. 2005.

[21] K. H. Lo, C. H. Shek, and J. K. L. Lai. "Recent developments in stainless steels". In: *Materials Science and Engineering: R: Reports* 65.4 (May 29, 2009), pp. 39–104. ISSN: 0927-796X. DOI: 10.1016/j.mser.2009.03.001. URL: https://www.sciencedirect.com/science/article/pii/S0927796X09000461 (visited on 12/16/2022).

[22] R Parrott and H Pitts. *Chloride stress corrosion cracking in austenitic stainless steel*. Research RR902. Health and Safety Executive, Nov. 2011, p. 52.

[23] Masahito Mochizuki. "Control of welding residual stress for ensuring integrity against fatigue and stress–corrosion cracking". In: *Nuclear Engineering and Design* 237.2 (Jan. 1, 2007), pp. 107–123. ISSN: 0029-5493. DOI: 10.1016/j.nucengdes.2006.05.006. URL: https://www.sciencedirect.com/science/article/pii/S0029549306003748 (visited on 11/09/2022).

[24] Darrell S Dunn. "Chloride-Induced Stress Corrosion Cracking Tests and Example Aging Management Program". In: (2014), p. 26.

[25] B. T. Lu et al. "Pitting and stress corrosion cracking behavior in welded austenitic stainless steel". In: *Electrochimica Acta* 50.6 (Jan. 30, 2005). ISSN: 0013-4686. DOI: 10.1016/j.electacta.2004.08.036. (Visited on 11/09/2022).

[26] G. Çam. "Friction stir welded structural materials: beyond Al-alloys". In: *International Materials Reviews* 56.1 (Jan. 1, 2011), pp. 1–48. ISSN: 0950-6608. DOI: 10.1179/095066010X12777205875750. (Visited on 04/26/2023).

[27] R. S. Mishra and Z. Y. Ma. "Friction stir welding and processing". In: *Materials Science and Engineering: R: Reports* 50.1 (Aug. 31, 2005), pp. 1–78. ISSN: 0927-796X. DOI: 10.1016/j.mser.2005.07.001.

[28] A. Heidarzadeh et al. "Friction stir welding/processing of metals and alloys: A comprehensive review on microstructural evolution". In: *Progress in Materials Science* 117 (Apr. 1, 2021), p. 100752. ISSN: 0079-6425. DOI: 10.1016/j.pmatsci.2020.100752. URL: https://www.sciencedirect.com/science/article/pii/S007964252030116X (visited on 12/23/2021).

[29] *Spex SamplePrep 8001 Grinding Vial Set, Hardened Steel, 65 mL; 1/EA from Cole-Parmer*. URL: https://www.coleparmer.com/ (visited on 04/26/2023).

CHAPTER 3

Localized Corrosion of Friction Stir Alloyed Austenitic Stainless Steel

Abstract

stainless steels, particularly 300 series, are susceptible to chloride induced stress corrosion cracking (CISCC) in chloride environments. Examples of CISCC have been reported on the surfaces of Type 304, 304L, and 316L stainless steel components in a variety of enviroments where chloride is present. Localized pitting or crevice corrosion probably precedes CISCC, and therefore improving the pitting resistance of a material should improve resistance to CISCC. Friction stir processing is a proposed technique to repair and strengthen material that has developed chloride induced stress cracks by adding molybdenum to the base material. By using Electro-chemical techniques, an evaluation of 304L that has been friction stir process with molybdenum has been performed. Research suggests that the addition of molybdenum should improve pitting resistance but the results do not agree. The results suggests that the addition of the molybdenum through FSP was not beneficial to pitting resistance of the samples but was beneficial in decreasing the corrosion current and in the case of the FSP 304L+Mo increasing the linear polarization significantly. These improvements are important because it slows down the corrosion kinetics. Cyclic polarization did reveal that the FSP 304L sample did show the most improvement in pitting potential when compared with the other samples.

3.1 Introduction

The Nuclear Regulatory Commission has identified chloride-induced stress corrosion cracking (CISCC) of austenitic stainless steel dry cask storage systems (DCSS) as an area of great concern. Dry storage systems are used for long-term storage (up to 100 years) of spent nuclear fuels. These DCSS are made of 300 series austenitic stainless steel that has general corrosion resistance but are particularly susceptible to chloride induced corrosion. Examples of CISCC have been reported on the surfaces of Type 304, 304L, and 316L stainless steel components in chemical reactor vessels, urea plant vessels, rock climbing equipment, and at nuclear power plants [1].

Because of the passive cooling features in a DCSS, the steel canister is in direct contact with the atmosphere. The air that cools the DCSS also contains salt particles, which are deposited on the surface of the steel [2]. Depending on temperature and humidity [3] the salt deposits will deliquesce and create an aqueous chloride solution. Water is an essential component of CISCC and if absent CISCC cannot be sustained [4]. Aqueous chloride solutions induces pit nucleation because the chloride ions encourage passive layer break down by stimulating the oxidation reaction [5] which causes dissolution of metal.

$$M \rightarrow M^{+} + e^{-} \tag{3.1}$$

Because chloride ions are so mobile in solution, they migrate to any area where metal dissolution is high to balance the excess positive charge. This concentration of metal ions and chloride ions creates insoluble metal hydroxide and free acid.

$$M^+Cl^- + H_2O = MOH + H^+Cl^- \tag{3.2}$$

As chloride ions concentrate to areas with high concentrations of metal ions this can create a localized area of corrosion called a pit. Pitting corrosion is an extremely localized form of corrosion that causes a hole or cavity in the metal as shown in Figure. 2.3. It is particularly deleterious to structural integrity because it can cause failure with only a small percentage of mass loss. As pits nucleate they create an autocatalytic process that perpetuates and exacerbates corrosion damage by depleting the pit of oxygen which inhibits the reduction reaction shown in Equation 3.3[5] [6]. The reduction reaction continues on the surface of the metal and suppresses corrosion of the base metal surface.

$$O_2 + 2H_2O + 4e^- \rightarrow 4OH^- \tag{3.3}$$

$$2Cr + H_2O \rightarrow Cr_2O_3 + 6H^+ + 6e^- \tag{3.4}$$

It is known that localized corrosion, like pits, act nucleation sites for cracks to form [7] [8] [9]. Friction stir processing (FSP) is a proposed method for repairing cracks and strengthening the base metal of the DCSS against pit formation. Using FSP techniques, beneficial elements can be added to the base metal to improve resistance to CISCC. Research shows that materials with increased resistance to pitting are more suitable for environments that encourage CISCC. This resistance can be described with the pitting resistance equivalent number (PREN) [10].

$$PREN = \%wtCr + 3.3 \times (\%wtMo + 0.5\%wtW) + 16 \times \%wtN \tag{3.5}$$

Molybdenum is added to 304L stainless steel via FSP and the newly processed material will be tested using the electro-chemical technique cyclic polarization. By using this analytical method, we can show if the proposed treatment will improve resistance to chloride induced corrosion.

3.2 Materials and Procedures

304L powder was ball milled with molybdenum powder to create a homogenized mixture with elevated amounts of molybdenum. Parameters are given in Figure. 3.1.

Table 3.1: Ball mill parameters

Powder size	Charge ratio	Charge contents	Surfactant	Mill time	Mill type
304L: 15-53 μm	13:1	304L: 9.66g	Stearic acid: 0.11g	60 Hours	Planetary
Mo: 35-45 nm		Mo: 0.74g			

After the ball milling process is completed, the powder is formed, pressed and sintered using the parameters given in Figure. 3.2. After the pellets are sintered, they are they are placed into a 0.5 inch thick plate of 304L stainless steel plate that has been prepared with holes, like the one seen in Figure. 3.2, to accept the pellets. This steel plate meets the ASTM A240/A240M-15 standard for pressure vessels and general applications and the composition of the 304L plate used is given in Table 3.3. The plate is then friction stir processed with compacts of 316L and the ball milled mixture of 304L with molybdenum. The composition of the samples being tested can be found in Table 3.4.

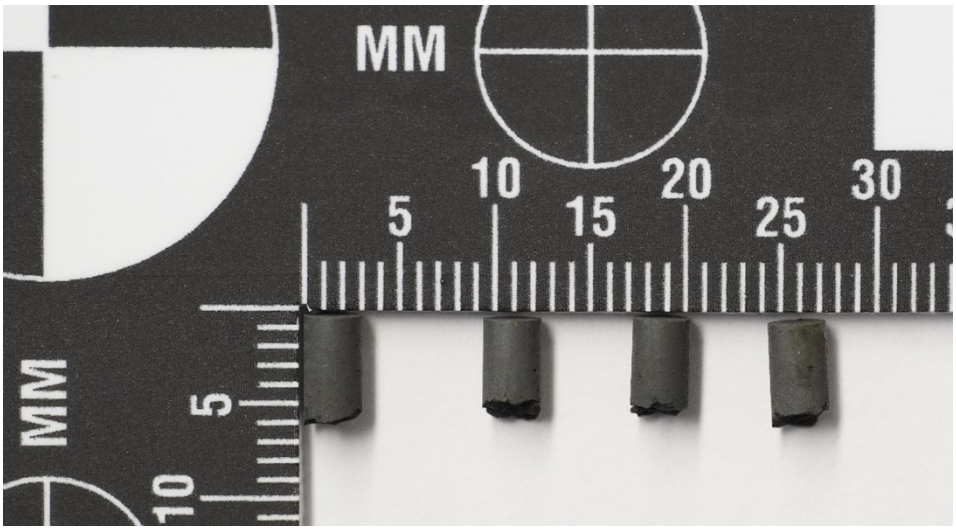

Figure 3.1: Pellets of ball milled 304L+Mo after sintering

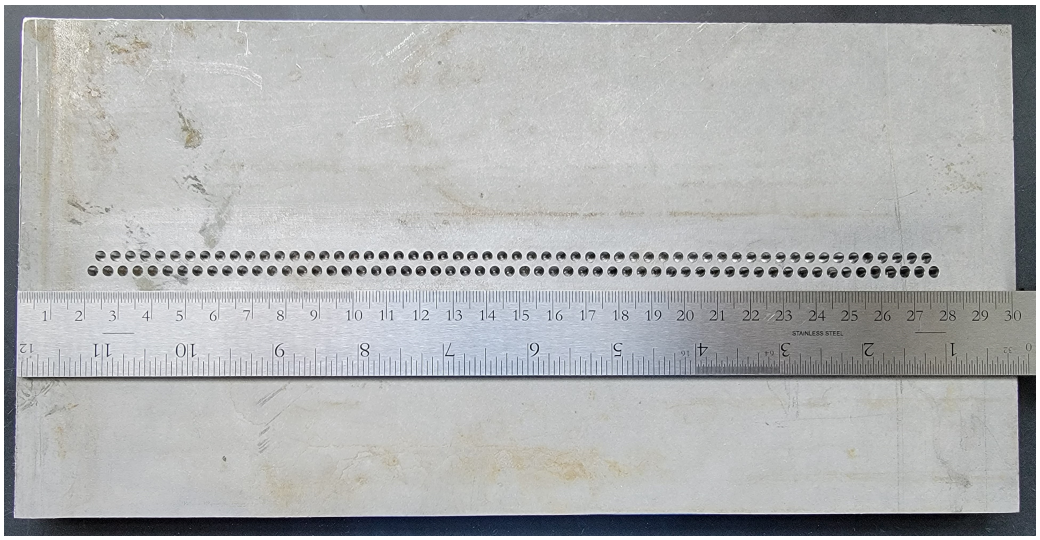

Figure 3.2: 304L plate with holes drilled to accept pellets

Table 3.2: Press and sinter parameters

	304L+Mo	316L
Pressure (mt)	0.6	0.6
Pressure hold time (min)	1	1
Sinter temperature (°C)	750	750
Sinter time (min)	90	90
Heating rate (°C/min)	12	12
Dwell time (min)	30	30
Density (g/cm^3)	6.21	4.84

Table 3.3: Composition of 304L Plate provided by steel mill

Element	C	Si	Mn	P	S	Ni	Cr	Mo	N	Cu	Fe
Percent Weight	0.025	0.34	1.33	0.026	0.001	8.05	18.19	0.27	0.070	0.36	Bal

Table 3.4: Composition of samples to be tested

Sample	Compact Composition (%wt)	%wt of Mo in bulk sample
FSP 304L+Mo	304L: 97.75% Mo: 2.25 %	0.688
FSP 304L+316L	316L: 100%	0.5
FSP 304L	N/A	N/A
304L	N/A	N/A

3.2.1 Grain Size

Microstructure analysis of the samples was done using etching techniques developed by Frederick C. Bell and Daniel E. Sonon at the U.S. steel corporation, research laboratory [11]. Generally electrolytic etching in oxalic acid is the standard for revealing grain structure in austenitic stainless steel but if the steel is annealed then the etchant preferentially attack twins and not the grain boundaries. Therefore electrolytic etching using a 60% nitric acid solution was used. To prepare samples for electrolytic, they were ground using silicon carbide grinding paper starting at 180 grit and ending in 1200 grit. Polishing was performed using 3 µm and 1µm polycrystalline diamond suspension. For electrolytic, the power supply was set to a no-load voltage of 1 V. Each sample was submersed in a 60% nitric acid solution using stainless steel tweez-

ers. The negative side of the power supply was attached to a 304L stainless steel cathode with dimensions of 7x1.5x1 cm. The positive side of the power supply was connected to the tweezers holding the samples. After submersion, the power supply was adjusted so a current density of 10 mA/cm^2 was maintained. Samples were etched for four minutes, rinsed in deionized water, then methanol. A light microscope was used to determine if the grain structure was sufficiently etched. If under etched, samples were etched again for two minutes. After etching, samples were examined using a light microscope and ASTM standard E112-96 [12] for determining average grain size was used. Several micrographs were taken using an optical light microscope of each sample to obtain a statistically sound estimate of the grain size.

$$s = [\frac{\Sigma(X_i - \overline{X})^2}{n-1}]^{1/2} \tag{3.6}$$

$$95\%CI = \frac{t * s}{\sqrt{n}} \tag{3.7}$$

$$\%RA = \frac{95\%CI}{\overline{X}} * 100 \tag{3.8}$$

The circular intercept procedure from ASTM E112-96 was used to determine the mean lineal intercept value, $\bar{l}$. Statistical analysis was performed using standard deviation (Equation 3.6), 95% confidence interval (Equation 3.7), and relative accuracy (Equation 3.8). The ASTM E112-96 standard recommends that the relative accuracy is 10% or lower to be considered acceptably precise for most purposes. The mean planar grain size ($\bar{d}$) is about 12% larger than $\bar{l}$ [13].

3.2.2 Experimental Set Up

Analysis was performed using a Gamry interface 1000 poteniostat. Using a silver/silver chloride reference electrode and a platinum wire as the counter electrode. Two electrolytes were used, 3.5%wt sodium chloride to simulate sea water and 2.5 M sulfuric acid with 0.5 M sodium chloride.

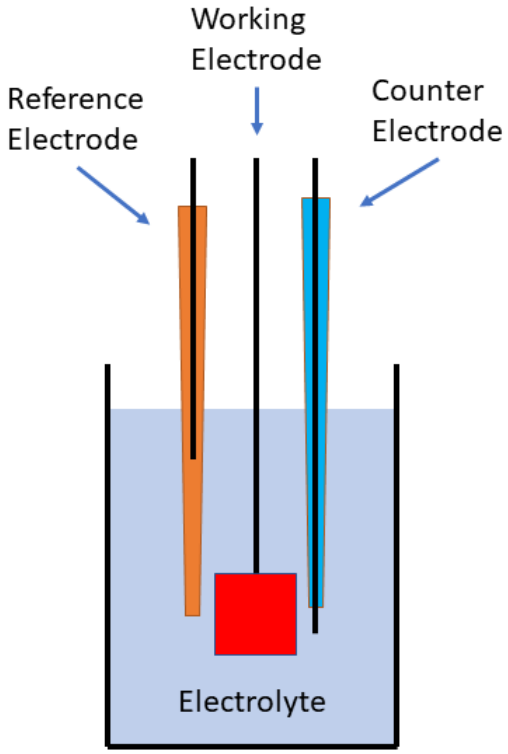

Figure 3.3: Experimental set up

Corrosion samples were cut from the bulk plate as shown in Figure 3.5. Samples were cleaned with acetone before being soldered with a wire. This wire is how the sample will be connected to the potentiostat. Each sample was 1 cm^2 and mounted in acrylic. Samples were polished to 3 micron diamond polycrystalline suspension for cyclic polarization. If any porosity could be seen with the light optical microscope, nail polish was used to create a resist to prevent any porosity from skewing the results

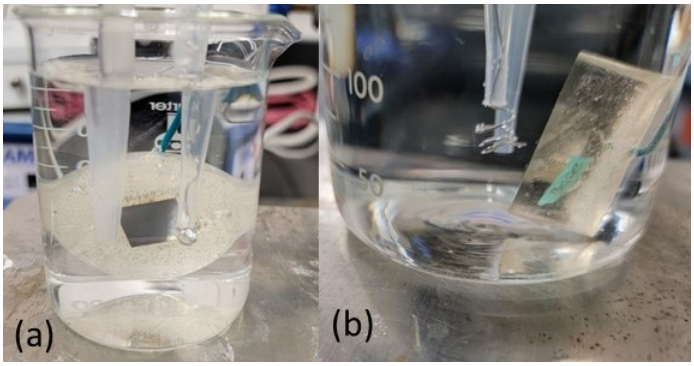

Figure 3.4: (a) front view of the experiment (b) Side view of the experiment from the cyclic polarization.

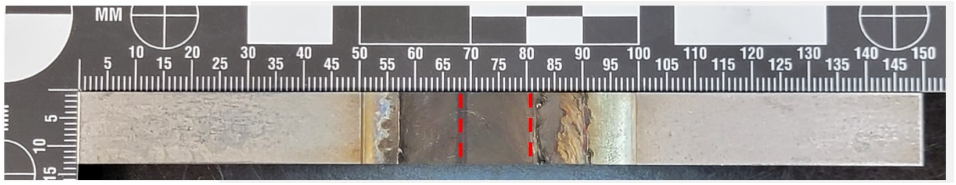

Figure 3.5: Bulk sample before sectioning into corrosion sample. Red dashed lines indicate where the corrosion sample was sectioned

Table 3.5: Cyclic polarization parameters and values for 3.5%wt sodium chloride

Parameter	Value
Initial E(V)	-0.25 vs E_{oc}
Apex E(V)	0.7 vs E_{oc}
Final E(V)	-0.25 vs E_{oc}
Foward Scan (mV/s)	0.1667
Sample Period (s)	1
Sample Area (cm^2)	1
Density (g/cm^3)	7.87
Equivalent Weight	20.12

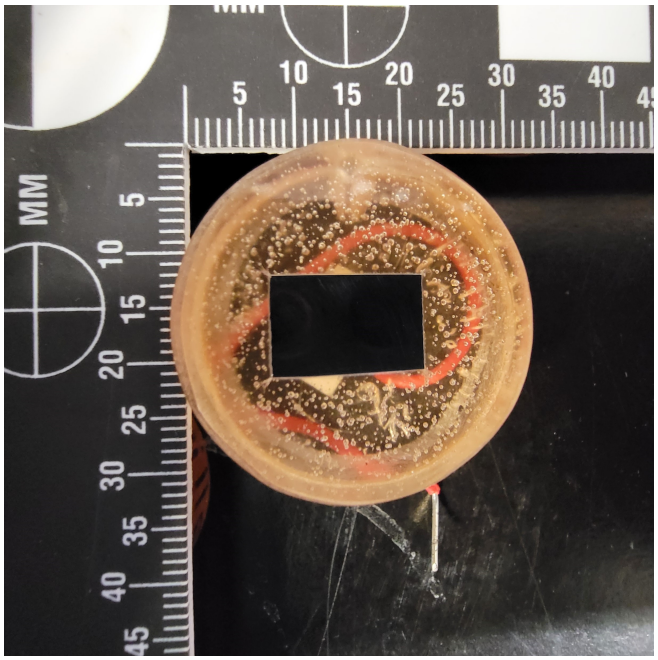

Figure 3.6: Sample mounted in acrylic and polished with 3 micron diamond polycrystalline suspension

Table 3.6: Cyclic polarization parameters and values for 2.5 M sulfuric acid with 0.5 M sodium chloride.

Parameter	Value
Initial E(V)	0 vs E_{oc}
Apex E(V)	1.6 vs E_{oc}
Final E(V)	0 vs E_{oc}
Foward Scan (mV/s)	0.1667
Sample Period (s)	1
Sample Area (cm^2)	1
Density (g/cm^3)	7.87
Equivalent Weight	20.12

3.3 Results and Discussion

A major factor for determining how well an austenitic stainless steel will do in an environment with chloride is to evaluate the pitting potential, E_p, and the pitting protection potential, E_{pp}. The pitting potential is linked to a materials resistance to CISCC [2] and characterizes the resistance of metals to pitting corrosion and, therefore can be considered as a measure of susceptibility of different metals and alloys to pitting corrosion in aggressive environments. The more noble the value of E_p, the more resistant the alloy is to pitting [8] [14]. At potentials below the pitting protection potential, pits are very unlikely to form. Pits that form between E_p and E_{pp} are metastable and are just as likely to passivate as they are to grow. When the potential increases past E_p, the pits become stable and no longer passivate. Corrosion potential, E_{corr}, provides us with a general idea of the performance of a material. The more noble it is, the better it is generally at resisting corrosion. Linear resistance helps describe the rate of corrosion. Where R_p is equal to the linear resistance of the material, K is a material unique value that defines the units of the corrosion rate, and EW is the equivalent weight of the material. From these equations we can see that the larger R_p value, the slower the corrosion rate for the given material.

$$I_{corr} = \frac{1}{R_p} \frac{\beta_a \beta_c}{2.303(\beta_a + \beta_c)} \tag{3.9}$$

$$\text{Corrosion Rate} = \frac{I_{corr} \cdot K \cdot EW}{dA} \tag{3.10}$$

It is difficult to label a material as corrosion resistant because the potential at which the material operates may be different based on where the material is used. Any

judgments based on the experimental results will be for this experiment specifically but we can draw general insight about the material based off the results.

3.3.1 Cyclic Polarization with 3.5%wt Sodium Chloride Electrolyte

The use of 3.5%wt sodium chloride electrolyte will provide a reasonably suitable environment to replicate the environment that the DCSS are in. The values obtained from the cyclic polarization tests are displayed in Table 3.7.

304L While 304L does have general corrosion resistance for this experiment it performed the worst of the four samples. From Table 3.7. we see that E_{corr}, E_p, and the passive region are the least noble. Figure 3.7 reveals very little frenetic oscillations in the current density during the cyclic polarization test which is to be expected because the base metal comes directly from the foundry and should be free of porosity or inclusions that might cause the passive layer to be weak

FSP 304L FSP 304L had the best E_p of the four samples and a large passive region. The cyclic polarization graph reveals oscillations in the current in the passive region, as the potential approaches a maximum, and as the potential drops off after the maximum potential. This behavior is indicative of a weak passive layer from porosity or inclusions. This might be caused by improper friction stir rotational or translational speeds.

FSP 304L+Mo FSP 304L+Mo had the worst E_p of the friction stir processed samples, but it's I_{corr} and linear resistance were the best of the four. This is indicative of slow corrosion rates as defined be Equation 3.9 and 3.10. Figure 3.7 reveals small

amounts of oscillation in the current density but overall smoothness during the cyclic polarization test.

FSP 304L+316L With only a 3.7 mV difference in E_p when compared with the FSP 304L sample, and the second best I_{coor}, the FSP 304L+316L sample performed well in the cyclic polarization test using the 3.5%wt sodium chloride. Figure 3.7 shows many oscillations in the current density throughout most of the cyclic polarization test. This provides additional evidence of surface defects which detract from corrosion resistance

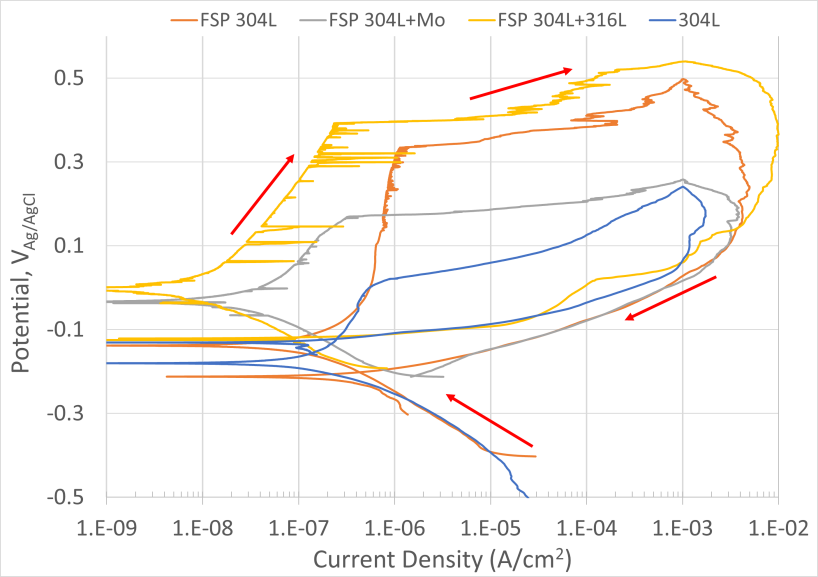

Figure 3.7: Superimposed graph of all samples using cyclic polarization and 3.5%wt sodium chloride solution

Table 3.7: Averaged values derived from cyclic polarization on prepared samples

Parameters	304L	FSP 304L	FSP 304L + 316L	FSP 304L + Mo
E_{corr}(V)	-0.1533 ± .0268	-0.154 ± 0.0205	-0.0681 ± 0.0459	-0.03243 ± 0.00117
E_p(V)	0.0421 ± .0409	0.3342 ± 0.0365	0.3305 ± 0.0254	0.2872 ± 0.1209
E_{pp}(V)	-0.1021 ± .1616	-0.1819 ±0.0443	-0.1972 ± 0.00541	-0.4776 ± 0.0977
Bottom of Passive Region (V)	-0.0988 ± 0.0222	-0.01668 ± 0.02990	-0.0156 ± 0.0207	0.0181 ± 0.0302
Top of Passive Region(V)	0.0419 ± 0.0417	0.332 ± 0.3182	0.3051 ± 0.0598	0.2872 ± 0.1209
β_a(V/Decade)	0.1025 ± 0.0272	0.2681 ± 0.2105	0.2223 ± 0.1442	0.0695 ± 0.00242
β_c(V/Decade)	0.0901 ± 0.0302	0.2758 ± 0.2455	0.09397 ± 0.03431	0.0501 ± 0.00637
I_{corr}(A)	$1.132 \times 10^{-7} \pm 0.4621 \times 10^{7}$	$1.8 \times 10^{-7} \pm 1.41 \times 10^{-7}$	$7.183 \times 10^{-8} \pm 2.516 \times 10^{-8}$	$1.15 \times 10^{-8} \pm 0.078 \times 10^{-8}$
Linear Resistance (Ω)	$89.8 \times 10^{3} \pm 30.2 \times 10^{3}$	$242 \times 10^{3} \pm 139 \times 10^{3}$	$218 \times 10^{3} \pm 234 \times 10^{3}$	$1100 \times 10^{3} \pm 187 \times 10^{3}$

3.3.1.1 Microstructure after Cyclic Polarization

After cyclic polarization with the 3.5%wt sodium chloride electrolyte solution, micrographs were taken of the surface of each sample to ascertain any visual corrosion damage. It was expected to see damage in the form of pits but the size and morphology were unclear before observing the samples. Samples were cleaned in an ultra-sonic cleaner in deionized water to remove as much corrosion products that might be obscuring the surface and the pits. A light optical microscope at the lowest magnification was used to inspect the surface of each sample and identify any areas of corrosion damage. The entire sample surface area was examined using a 5X objective, when pits were identified the 10X and 50X objective were used to reveal the details of the pits. The 304L and FSP 304L samples, Figure 3.8 and Figure 3.9. respectively, did not have much visual sign of corrosion damage. The small dark spots are too small to affirm as pits using the light optical microscope but because of the test performed it is logical to theorize that these are pits. Their small size does not fully reveal the extent of the damage, this could be the small opening to a much larger void (see Figure 2.3A).

Upon examining the FSP 304L+Mo and FSP 304L+316L large pits were discovered, see Figure 3.10, 3.11, and 3.12. These pits are substantially larger than the other pits observed in the 304L and FSP 304L samples. One of these types of pits was found on the FSP 304L+Mo sample and two were found on the FSP 304L+316L sample. The remaining surface of the FSP 304L+Mo and FSP 304L+316L samples was almost completely devoid of the small dark spots that were found on the other samples. Fontana and Green[5] suggest that pits act as sinks for corrosion and "protect" the rest of the surface from corrosion damage. Which is likely the reason why these two samples have less pit density of small pits.

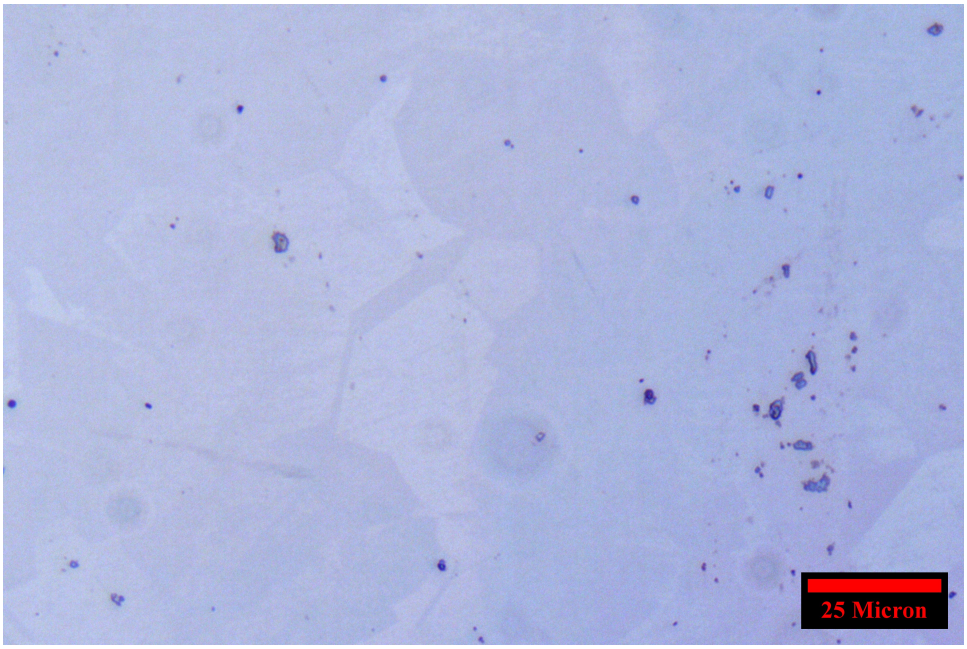

Figure 3.8: Optical light micrograph of 304L after cyclic polarization with 3.5%wt sodium chloride electrolyte using a light optical microscope

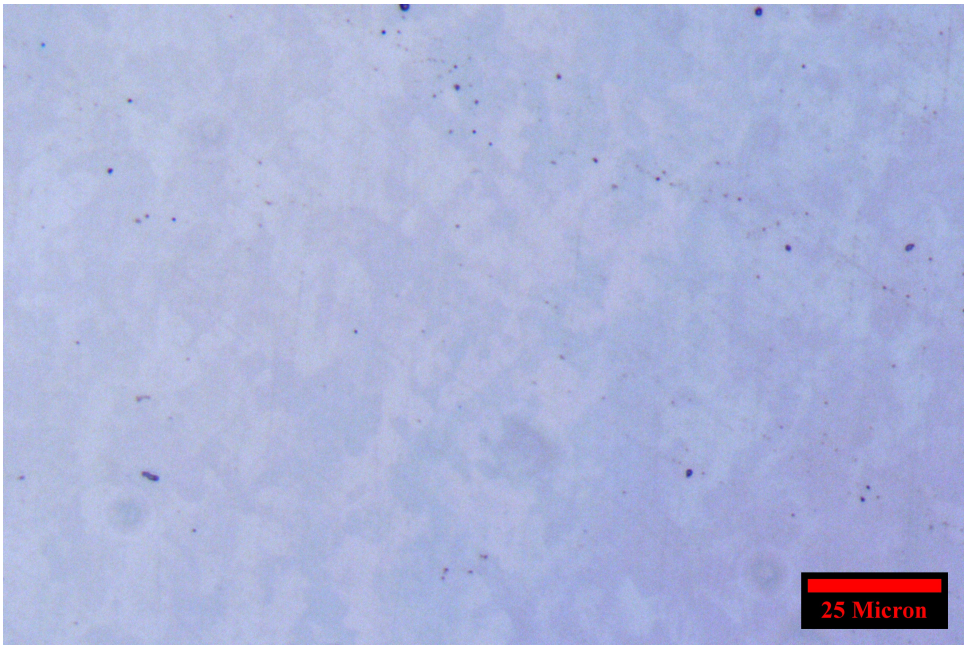

Figure 3.9: Optical light micrograph of FSP 304L after cyclic polarization with 3.5%wt sodium chloride electrolyte using a light optical microscope

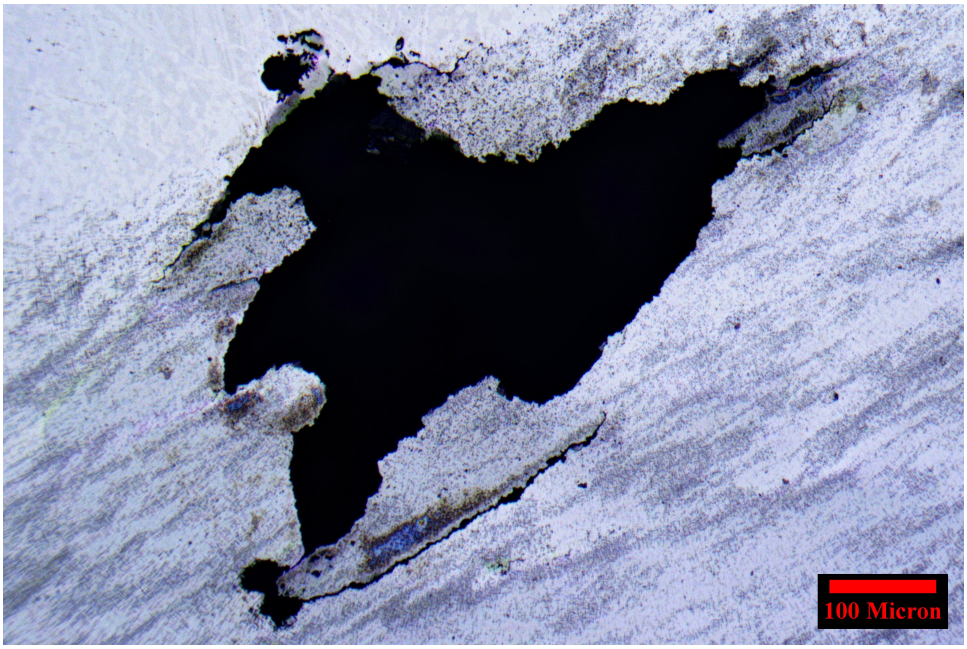

Figure 3.10: Light optical micrograph of FSP 304L+Mo after cyclic polarization using 3.5%wt sodium chloride solution

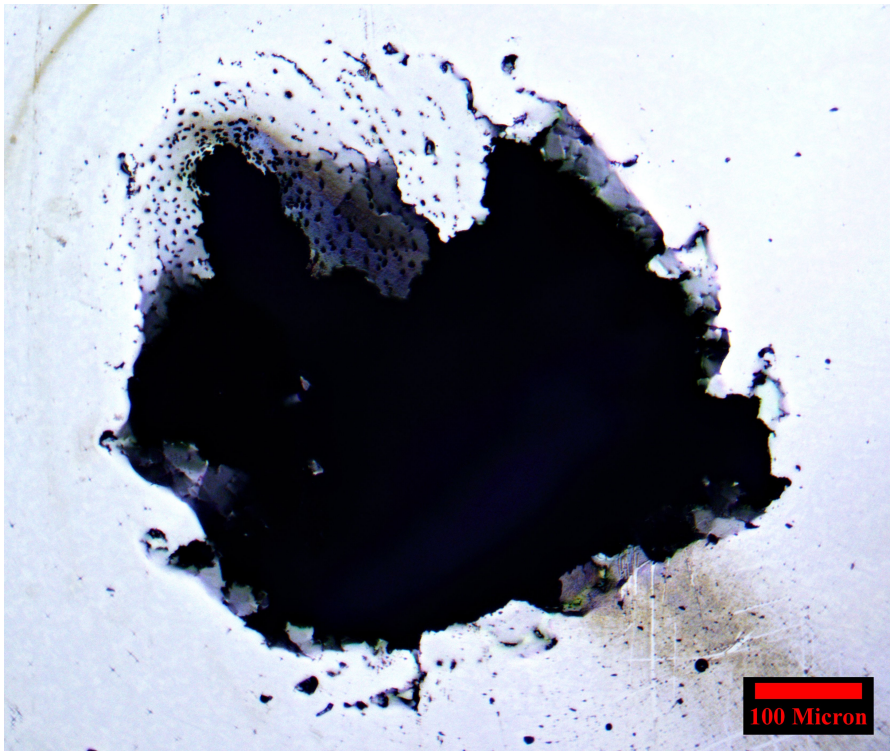

Figure 3.11: Light optical micrograph of FSP 304L+316L after cyclic polarization using 3.5%wt sodium chloride solution

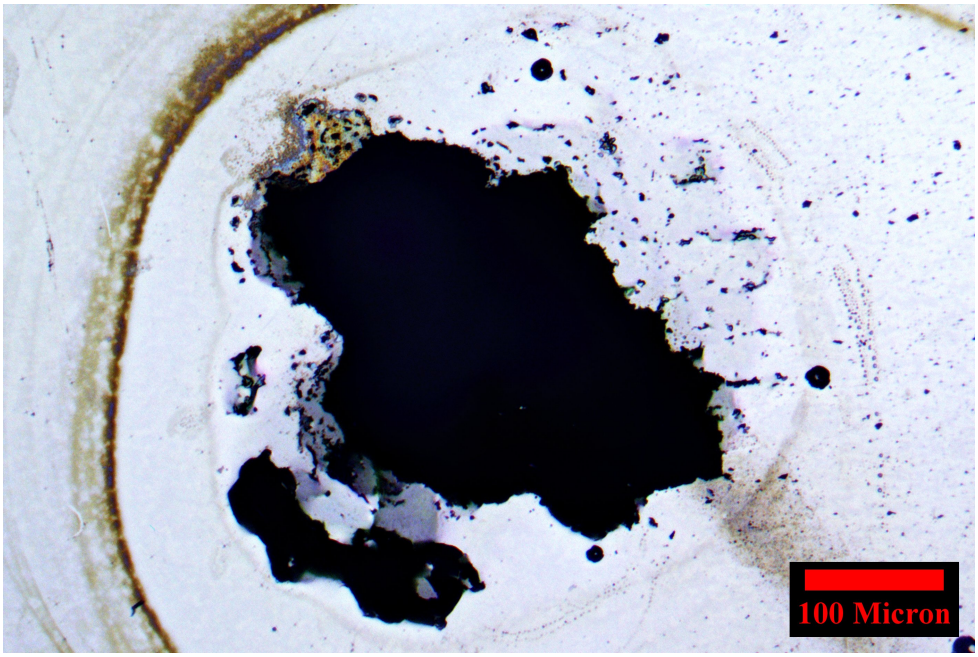

Figure 3.12: Light optical micrograph of FSP 304L+316L after cyclic polarization using 3.5%wt sodium chloride solution

3.3.2 Cyclic Polarization with 2.5 M Sulfuric Acid and 0.5 M sodium chloride

Cyclic polarization techniques using 2.5 M sulfuric acid and 0.5 M sodium chloride were applied to the four samples to explore what corrosion resistance if any was gained by friction stir processing or friction stir alloying with molybdenum. All four test performed very similarly, results can be seen in Table 3.8, with the best E_p, 1.030 V, coming from FSP 304L, yet only 10 mV separate it from the worst result of 1.020 V from 304L+316L.

Table 3.8: Values derived from cyclic polarization on prepared samples using 2.5 M sulfuric acid and 0.5 M sodium chloride

Parameters	304L	FSP 304L	FSP 304L+316L	FSP 304L+Mo
E_{corr}(V)	-0.3679	-0.3805	-0.3356	-0.3632
E_p(V)	1.021	1.030	1.020	1.029
E_{pp}(V)	1.021	1.030	1.020	1.029
I_{Crit}(A)	0.036	0.030	0.015	0.018
Lower Bound of Passive Region (V)	0.04224	0.0623	0.048	0.0413
Upper bound of Passive Region(V)	1.021	1.030	1.020	1.029

In the passive region of the FSP 304L+Mo sample, there is oscillation in the current which may suggest some porosity or inclusions weakening the passive layer. The FSP 304L sample also has some oscillation, but it is much smoother than FSP 304L+Mo. This may indicate that there is still porosity or inclusions but not to the same degree as the FSP 304L+Mo sample. When comparing results from Table 3.7 and Table 3.8 there is a large disparity between many of the values. E_{corr} in the sulfuric acid and sodium chloride solution was significantly less noble when compared with the 3.5%wt sodium chloride solution. The E_{corr} of the FSP 304L sample having a difference of 214.6 mV between the two electrolytes, yet when comparing E_p, the sulfuric acid and sodium chloride solution resulted in a value 695.8 mV more noble than that of the 3.5%wt sodium chloride solution. This result may be because of

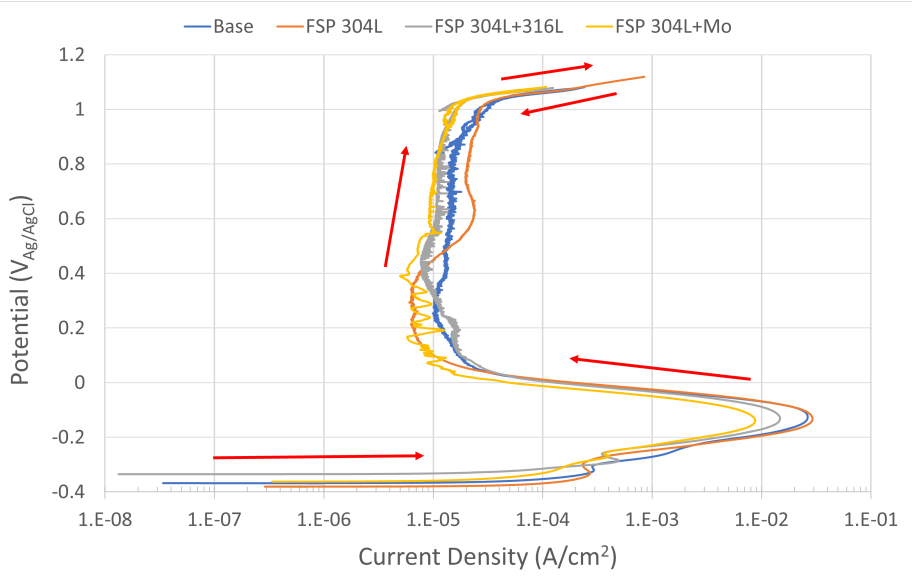

Figure 3.13: Superimposed graph of cyclic polarization tests using 2.5 M sulfuric acid and 0.5 M sodium chloride solution

the ability sulfate has in water, causing a higher ordering of water molecules. Sometimes called water structure makers or kosmotropes [15][16], some anions like sulfate (SO_4^{-2}) produces a high electric fields at short distances, binding the water molecules strongly and slowing down the migration of chloride anions in the aqueous solution. The kosmotrope dominated solution restricts pitting nucleation by slowing down the migration of chloride, or other halides anions, to the bare metal. Kosmotropes are more likely to adsorb on the surface of the passive layer, causing a pseudo-passive layer that resists pit nucleation [17]. This kosmotropic behavior suggests the reason for the noble E_p while the E_{corr} is so low when using the the sulfuric acid and sodium chloride electrolyte.

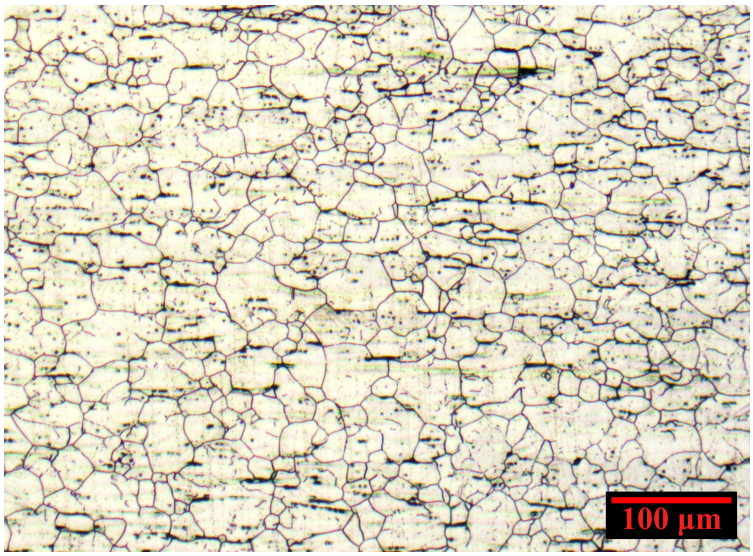

Figure 3.14: Light optical micrograph taken of etched 304L.

3.3.3 Grain Size

The application of ASTM E112-96 revealed that the friction stir processed samples had a reduced grain size when compared with the 304L, see Figure 3.9. This is congruent with the results from other research [18], [19], [20].

Table 3.9: Microstructure details of 304L samples before FSP, after FSP, and FSP with the addition of 316L and molybdenum.

	304L	FSP 304L	FSP 304L+316L	FSP 304L+Mo
$\bar{l}$ (μm)	19.60	3.93	3.08	5.20
$\bar{d}$ (μm)	22.35	4.40	3.45	5.82
s (μm)	$\pm$12.94	$\pm$2.43	$\pm$2.02	$\pm$3.87
95% CI	1.85	0.33	0.29	0.46
% RA	8.29	7.52	8.38	8.83

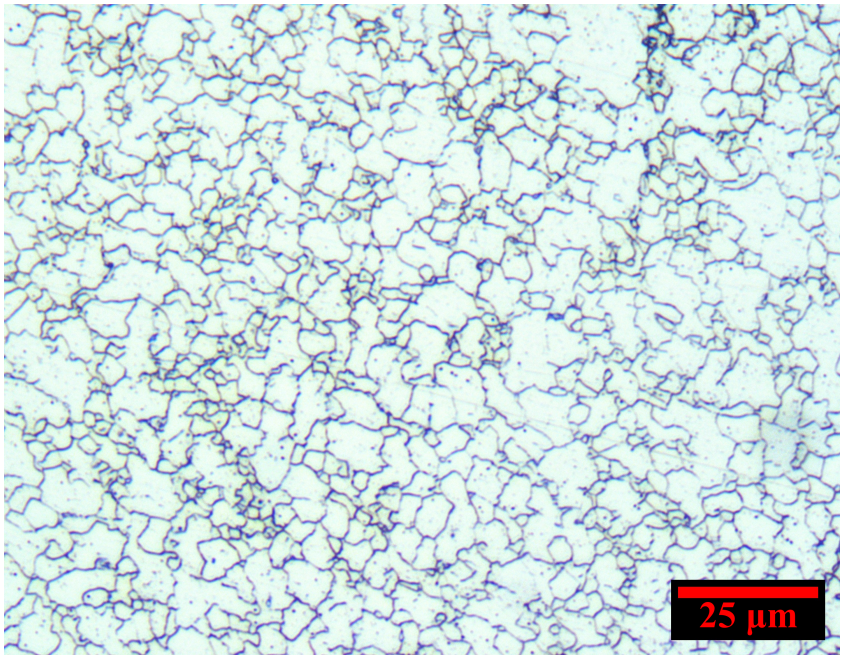

Figure 3.15: Light optical micrograph taken of etched FSP 304L.

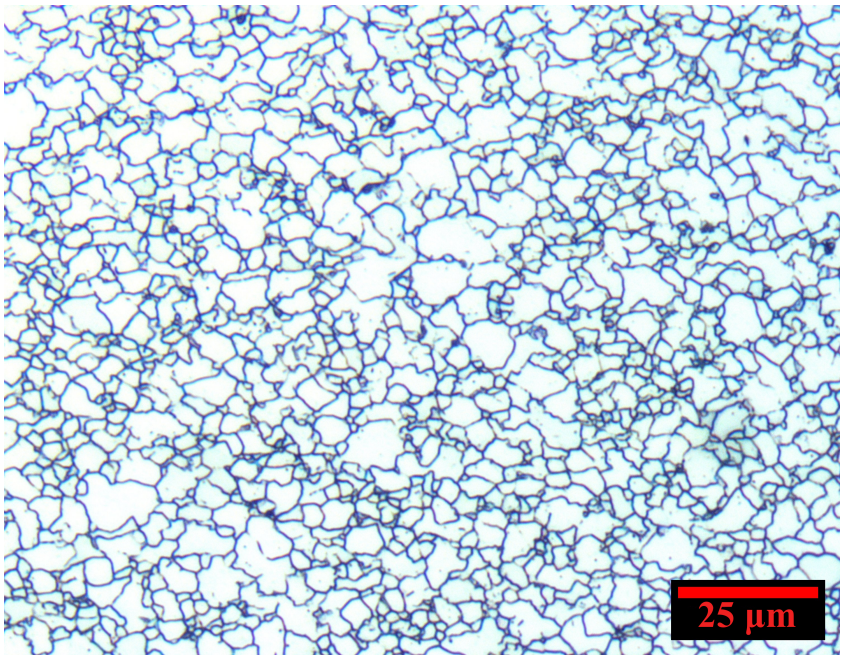

Figure 3.16: Light optical micrograph taken of etched FSP 304L+316L.

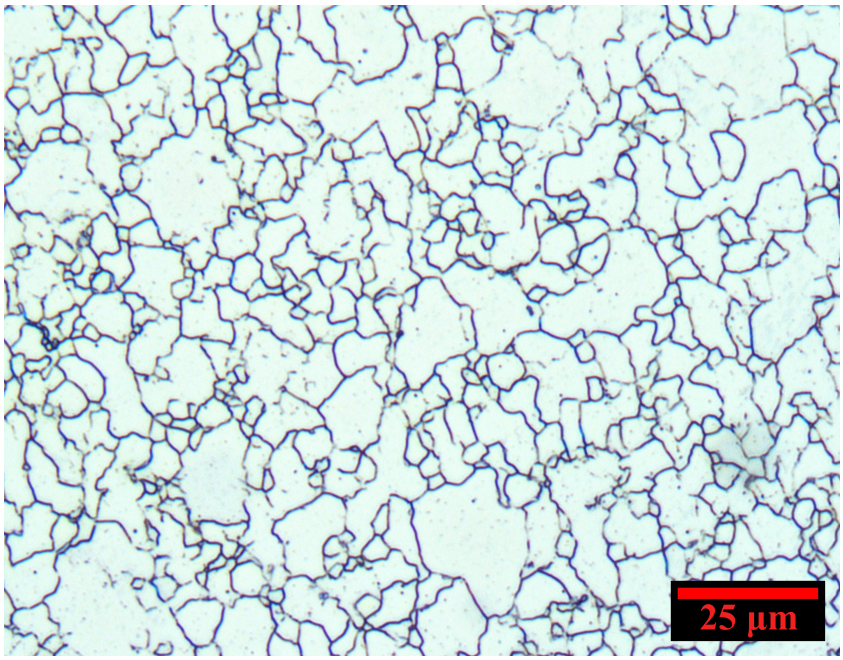

Figure 3.17: Light optical micrograph taken of etched FSP 304L+Mo

3.3.4 Surface Defects

While polishing the samples, surface artifacts were observed using the optical light microscope. The first artifacts observed were comet tails, as seen in Figure 3.18 and 3.19. The comet tails started to appear during 800 grit portion of the grinding process. Comet tails occur adjacent to inclusions or pores [21] or when an inclusion is pulled out of the sample [22]. Porosity and inclusions are possible with friction stir processing [23] [24]. The second surface artifact observed was what appeared as small dark spots on the surface of the sample, as can be seen in Figure 3.20. The concentration of surface artifacts varied between samples from only visible with a scanning electron microscope, like Figure. 3.22, to visible to the naked eye like in Figure 3.21. Scanning electron microscopy and energy dispersive spectroscopy revealed in Figure 3.22 that these dark spots are evidence of porosity and powder that did not become homogenized within the base metal [25].

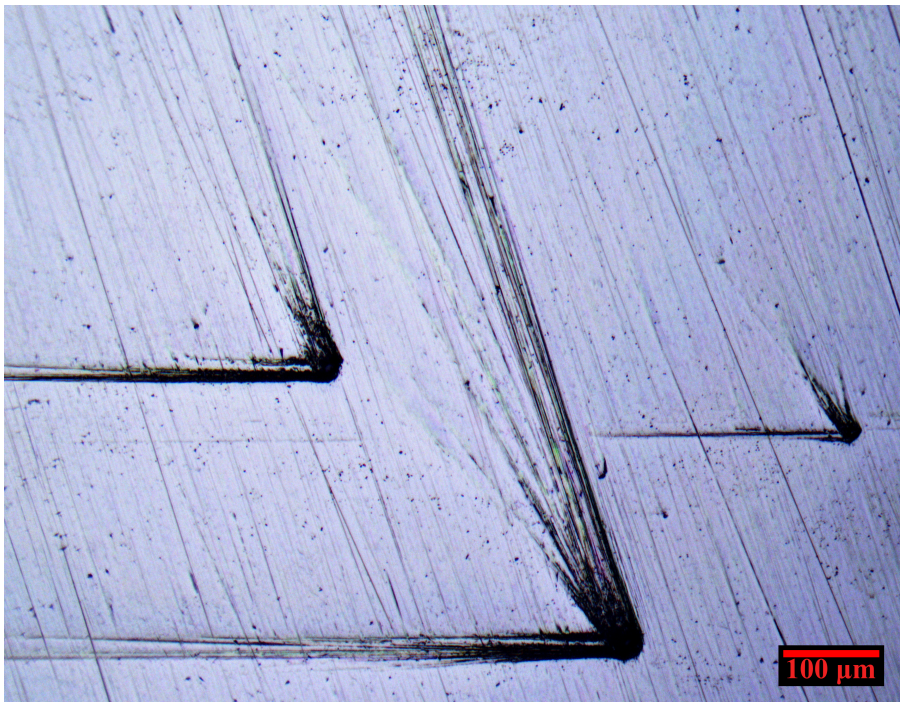

Figure 3.18: Comet tail observed after 800 grit grinding paper using light microscope at 10X

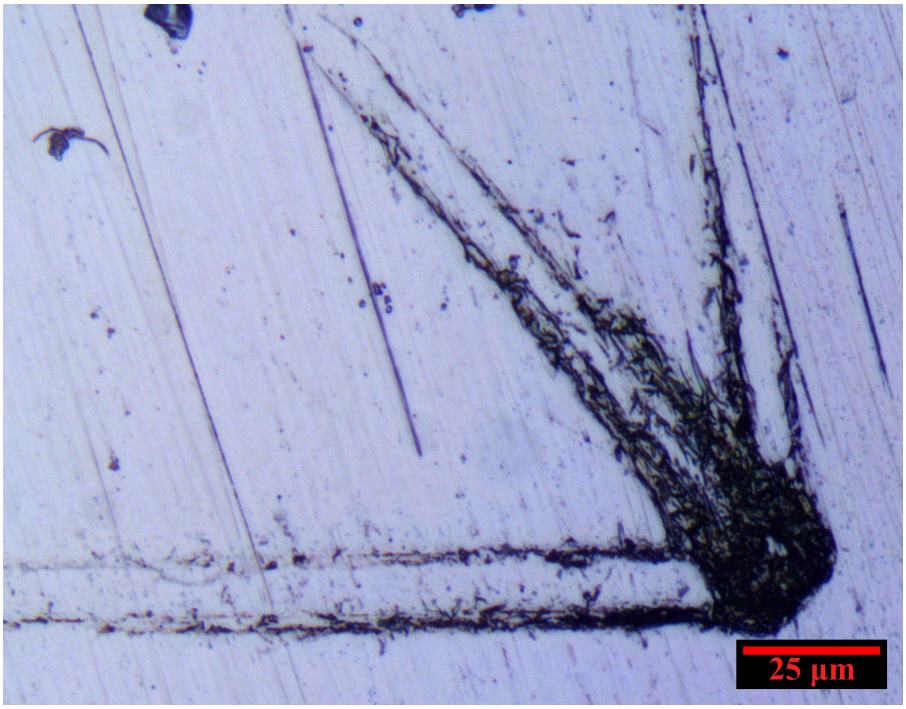

Figure 3.19: Comet tail observed after 800 grit grinding paper using light microscope at 50X

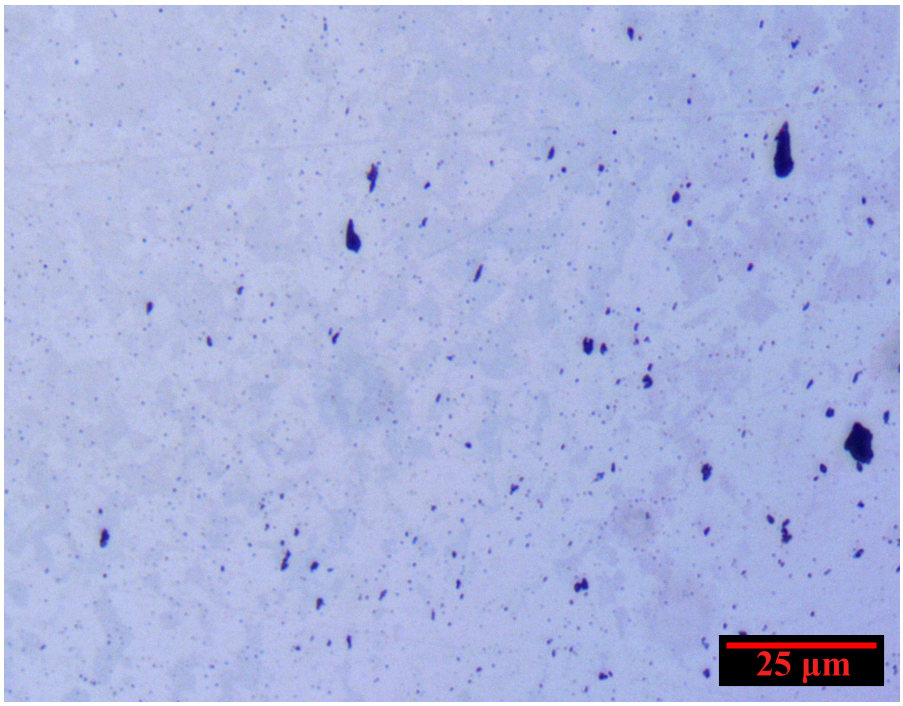

Figure 3.20: Surface artifacts observed in FSP 304L+316L after 1 μm diamond suspension

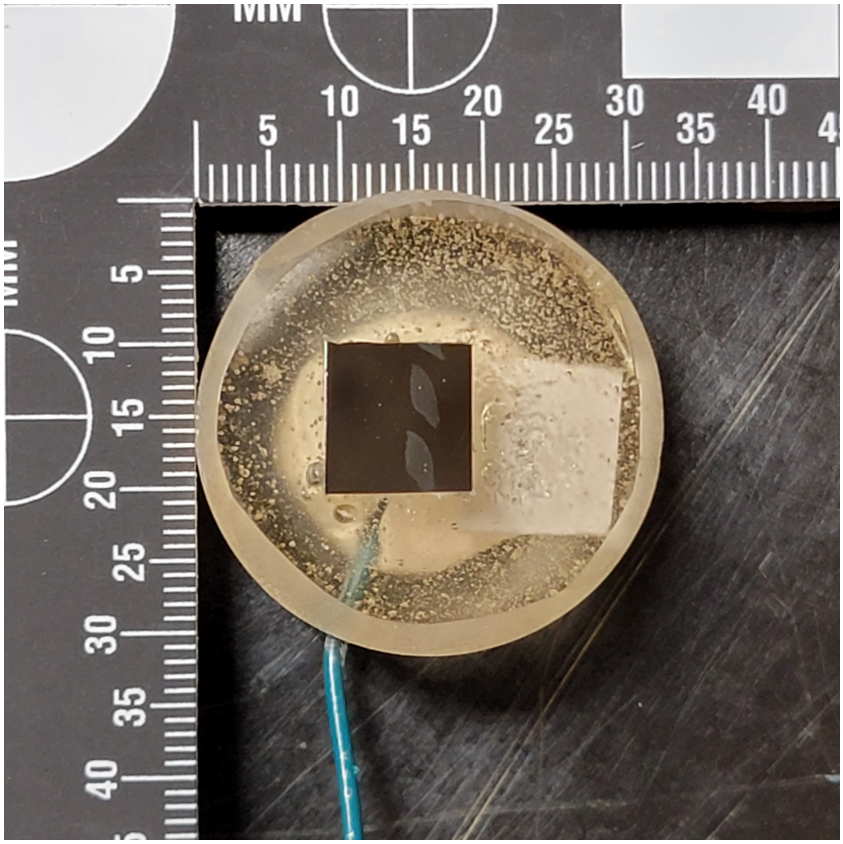

Figure 3.21: Photograph taken of FSP 304L+Mo sample with surface inclusions

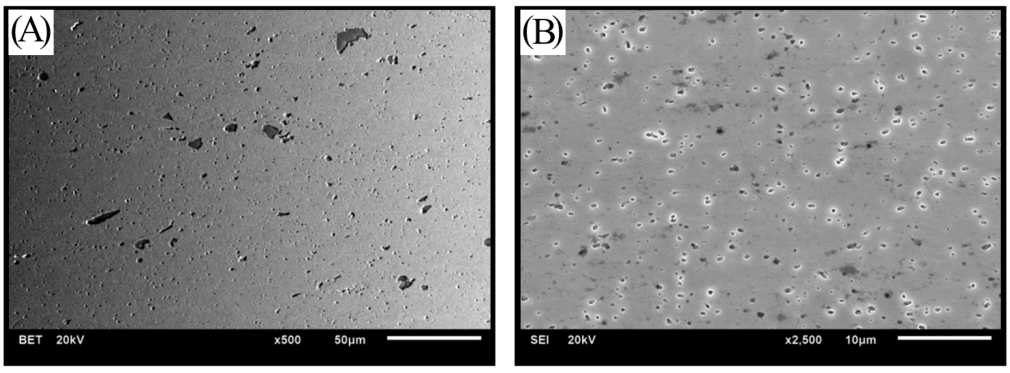

Figure 3.22: Scanning electron image of: (A)Backscatter electron image of the surface of the FSP 304L+316L sample and (B)Secondary electron image of the surface of the 304L+Mo sample.

3.4 Conclusion

Prior research suggests that the addition of molybdenum should improve pitting resistance but the results do not agree. The results obtained in this study suggests that the addition of the molybdenum through FSP was not beneficial to pitting potential of the samples but was beneficial in decreasing the I_{corr} and in the case of the FSP 304L+Mo increasing the linear polarization resistance significantly. These improvements are important because it slows down the corrosion kinetics. Cyclic polarization did reveal that the FSP 304L sample did show the most improvement in E_p when compared with the other samples. While the exact reason is beyond the scope of this thesis, research suggests that a reduction of grain size in Fe-Cr alloys can improve corrosion resistance because the increase in grain boundaries provides faster diffusion of Cr into the passive layer but the research community is not unanimous on this subject. Another possible reason for the improvement of corrosion resistance is that friction stir welding introduces low angle grain boundaries in the material which have been shown to improve corrosion resistance . In future work, the parameters of the friction stir process should be examined to determine if there is an ideal technique for mixing additives into Fe-Cr alloys. An examination of the limits of molybdenum that can be added via friction stir processing would also be of great importance to the research community.

Bibliography

[1] Tae M Ahn, Greg Oberson, and Sara DePaula. "Chloride-Induced Stress Corrosion Cracking of Austenitic Stainless Steel Used for Dry Storage of Spent Nuclear Fuel". In: *ECS Transactions* 50.31 (May 1, 2013), pp. 211–226. ISSN: 1938-5862, 1938-6737. DOI: 10.1149/05031.0211ecst. URL: https://iopscience.iop.org/article/10.1149/05031.0211ecst (visited on 09/28/2022).

[2] M. Mayuzumi, J. Tani, and T. Arai. "Chloride induced stress corrosion cracking of candidate canister materials for dry storage of spent fuel". In: *Nuclear Engineering and Design*. Concrete Cask Storage of Spent Fuel -Challenge of Economic Storage Technology 238.5 (May 1, 2008), pp. 1227–1232. ISSN: 0029-5493. DOI: 10.1016/j.nucengdes.2007.03.038. URL: https://www.sciencedirect.com/science/article/pii/S0029549307002518 (visited on 11/09/2022).

[3] L. Caseres and T.S. Mintz. "NUREG/CR-7030, "Atmospheric Stress Corrosion Cracking Susceptibility of Welded and Unwelded 304, 304L, and 316L Austenitic Stainless Steels Commonly Used for Dry Cask Storage Containers Exposed to Marine Environments."" In: (Oct. 2010), p. 90.

[4] P. R. Rhodes. "Mechanism of Chloride Stress Corrosion Cracking of Austenitic Stainless Steels". In: *Corrosion* 25.11 (Nov. 1, 1969), pp. 462–472. ISSN: 1938-159X, 0010-9312. DOI: 10.5006/0010-9312-25.11.462. URL: https://meridian.allenpress.com/corrosion/article/25/11/462/158324/Mechanism-of-Chloride-Stress-Corrosion-Cracking-of (visited on 04/12/2023).

[5] Mars G. Fontana. *Corrosion Engineering*. 3rd edition. New York: McGraw-Hill Book Company, Nov. 1, 1985. 556 pp. ISBN: 978-0-07-021463-7.

[6] Robert Kelly. "Passivity and Localized Corrosion". In: Robert Kelly et al. *Electrochemical Techniques in Corrosion Science and Engineering*. Series Title: Corrosion Technology. CRC Press, Sept. 13, 2002. ISBN: 978-0-203-90913-3. DOI: 10.1201/9780203909133.ch3. (Visited on 05/02/2023).

[7] K. Sugimoto and Y. Sawada. "The role of molybdenum additions to austenitic stainless steels in the inhibition of pitting in acid chloride solutions". In: *Corrosion Science* 17.5 (Jan. 1977), pp. 425–445. ISSN: 0010938X. DOI: 10.1016/0010-938X(77)90032-4.

[8] B. T. Lu et al. "Pitting and stress corrosion cracking behavior in welded austenitic stainless steel". In: *Electrochimica Acta* 50.6 (Jan. 30, 2005). ISSN: 0013-4686. DOI: 10.1016/j.electacta.2004.08.036. (Visited on 11/09/2022).

[9] R. J. Brigham and E. W. Tozer. "Effect of Alloying Additions on the Pitting Resistance of 18% Cr Austenitic Stainless Steel". In: *CORROSION* 30.5 (May 1974), pp. 161–166. ISSN: 0010-9312, 1938-159X. DOI: 10.5006/0010-9312-30.5.161. URL: http://corrosionjournal.org/doi/10.5006/0010-9312-30.5.161 (visited on 03/10/2023).

[10] Scott D Cramer and Bernard S. Covino. *ASM Handbook Volume 13B, Corrosion: Materials - ASM International*. Nov. 2005.

[11] Frederick C. Bell and Daniel E. Sonon. "Improved metallographic etching techniques for stainless steel and for stainless steel to carbon steel weldments". In: *Metallography* 9.2 (Apr. 1, 1976), pp. 91–107. ISSN: 0026-0800. DOI: 10.1016/0026-0800(76)90008-2. URL: https://www.sciencedirect.com/science/article/pii/0026080076900082 (visited on 03/11/2023).

[12] *Standard Test Methods for Determining Average Grain Size*. Version E112-96. 1996. DOI: 10.1520/E0112-96R04E01. (Visited on 05/09/2023).

[13] George F. Vander Voort. *Metallography, Principles and Practice*. Google-Books-ID: GRQC8zYqtBIC. ASM International, Jan. 1, 1999. 770 pp. ISBN: 978-1-61503-236-5.

[14] R Parrott and H Pitts. *Chloride stress corrosion cracking in austenitic stainless steel*. Research RR902. Health and Safety Executive, Nov. 2011, p. 52.

[15] Beibei Kang et al. "Hofmeister Series: Insights of Ion Specificity from Amphiphilic Assembly and Interface Property". In: *ACS Omega* 5.12 (Mar. 31, 2020). Publisher: American Chemical Society, pp. 6229–6239. DOI: 10.1021/acsomega.0c00237. URL: https://doi.org/10.1021/acsomega.0c00237 (visited on 05/26/2023).

[16] M. A. Hegazy et al. "An investigation of three novel nonionic surfactants as corrosion inhibitor for carbon steel in 0.5M H2SO4". In: *Corrosion Science* 54 (Jan. 1, 2012), pp. 219–230. ISSN: 0010-938X. DOI: 10.1016/j.corsci.2011.09.019. URL: https://www.sciencedirect.com/science/article/pii/S0010938X11004963 (visited on 05/26/2023).

[17] J. L. Trompette. "Implications of the kosmotrope/chaotrope nature of the anions on the breakdown of passivity of iron by halides". In: *Corrosion Science* 82 (May 1, 2014), pp. 108–114. ISSN: 0010-938X. DOI: 10.1016/j.corsci.2014.01.005. URL: https://www.sciencedirect.com/science/article/pii/S0010938X14000092 (visited on 05/26/2023).

[18] R. S. Mishra and Z. Y. Ma. "Friction stir welding and processing". In: *Materials Science and Engineering: R: Reports* 50.1 (Aug. 31, 2005), pp. 1–78. ISSN: 0927-796X. DOI: 10.1016/j.mser.2005.07.001.

[19] M. W. Mahoney et al. "Properties of friction-stir-welded 7075 T651 aluminum". In: *Metallurgical and Materials Transactions A* 29.7 (July 1, 1998), pp. 1955–1964. ISSN: 1543-1940. DOI: 10.1007/s11661-998-0021-5. URL: https://doi.org/10.1007/s11661-998-0021-5 (visited on 06/17/2023).

[20] Hidetoshi Fujii et al. "Friction stir welding of carbon steels". In: *Materials Science and Engineering: A* 429.1 (Aug. 15, 2006), pp. 50–57. ISSN: 0921-5093. DOI: 10.1016/j.msea.2006.04.118. URL: https://www.sciencedirect.com/science/article/pii/S0921509306005417 (visited on 06/17/2023).

[21] *Metallographic grinding and polishing insight — Struers.com*. URL: https://www.struers.com/en/Knowledge/ (visited on 05/10/2023).

[22] *Grinding and Polishing Guide - Buehler - Metallography Equipment & Supplies for Sample Preparation*. Section: Technical Article. Nov. 15, 2021. URL: https://www.buehler.com/blog/grinding-and-polishing-guide/ (visited on 05/10/2023).

[23] Yousef Imani, M. K. Besharati Givi, and Michel Guillot. "Improving Friction Stir Welding between Copper and 304L Stainless Steel". In: *Advanced Materials Research* 409 (2012). Publisher: Trans Tech Publications Ltd, pp. 263–268. ISSN: 1662-8985. DOI: 10.4028/www.scientific.net/AMR.409.263. URL: https://www.scientific.net/AMR.409.263 (visited on 05/10/2023).

[24] Shubham Verma and Joy Misra. “A Critical Review of Friction Stir Welding Process”. In: Jan. 1, 2015, pp. 249–266. ISBN: 978-3-902734-05-1. DOI: 10.2507/daaam.scibook.2015.22.

[25] Norah Alsairy. “Microstructural Modification and Mechanical Properties Evaluation of an Austenitic Stainless Steel Subjected to Friction Stir Based Repair”. PhD thesis. Idaho Falls, ID, USA: University of Idaho, 2023.

CHAPTER 4

U-bend analysis of Friction Stir Alloyed Austenitic Stainless Steel

Abstract

300 series stainless steels are particularly susceptible to chloride induced stress corrosion cracking (CISCC) in chloride environments. Examples of CISCC have been reported a variety of enviroments exposed to chloride salts. Localized pitting or crevice corrosion probably precedes CISCC, and therefore improving the pitting resistance of a material should improve resistance to CISCC. Friction stir processing is a proposed technique to repair and strengthen material that has developed chloride induced stress cracks by adding molybdenum to the base material. FSP samples were made by adding 316L and molybdenum powder to 304L stainless steel and then U-bend tested. The FSP 304L+316L and FSP 304L+Mo were more noble in the open circuit potential analysis and did not fail in the U-bend test yet the surface crack density was higher in the FSP samples. The FSP 304L+316L and FSP 304L+Mo were removed from the 2.5 M sulfuric acid + 0.5 M sodium chloride solution intact after 2472 hours with no failure. By contrast, the 304L U-bend sample had a low surface crack density yet failed at 267.5 hours. The potentiostatic analysis revealed that the FSP 304L+Mo sample had improved passivation kinetics.

4.1 Introduction

The Nuclear Regulatory Commission has identified chloride-induced stress corrosion cracking (CISCC) of austenitic stainless steel dry cask storage systems (DCSS) as an area of great concern. Dry storage systems are used for long-term storage (up to 100 years) of spent nuclear fuels. These DCSS are made of 300 series austenitic stainless steel that has general corrosion resistance but are particularly susceptible to chloride induced corrosion. Examples of CISCC have been reported on the surfaces of Type 304, 304L, and 316L stainless steel components in chemical reactor vessels, urea plant vessels, rock climbing equipment, and at nuclear power plants [1]. Friction stir processing (FSP) is a proposed method for repairing CISCC and strengthening the base metal of the DCSS. Using FSP techniques, beneficial elements can be added to the base metal to improve resistance to CISCC.

CISCC is difficult to detect while in progress, even when pervasive and can lead to rapid catastrophic failure of pressurized equipment. it is difficult to alleviate the environmental conditions that lead to CISCC. The level of chlorides required to produce CISCC is very low. The atmospheric contaminants responsible for CISCC generally come from NaCl or $MgCl_2$. Chloride contamination may come from concrete, like $MgCl_2$, or exposure to marine or industrial locations[2]. Because casks are generally located near bodies of water, because the reactor requires a water source for cooling, and casks are made with concrete it is extremely difficult to eliminate chloride contamination. In operation there can be evaporative concentration or a concentration in the surface film on a heat-rejecting surface. Tensile stress is one parameter that might be controlled. However the residual stresses associated with fabrication, welding, or thermocycling, rather than design stresses, are often responsible for SCC, and even stress-relieving heat treatments do not completely eliminate these residual stresses [3]

Research shows that materials with increased resistance to pitting are more suitable for environments that encourage CISCC. This resistance can be described with the pitting resistance equivalent number (PREN) [2].

$$PREN = \%wtCr + 3.3 \times (\%wtMo + 0.5\%wtW) + 16 \times \%wtN \tag{4.1}$$

This project will add molybdenum to 304L stainless steel via FSP and then test the newly processed material using U-bend techniques. By using these analytical methods, we can show if the proposed treatment will improve resistance to chloride induced corrosion.

4.2 Materials and Procedures

304L powder was ball milled with molybdenum powder to create a homogenized mixture with elevated amounts of molybdenum. Parameters are given in Figure 4.1.

Table 4.1: Ball mill parameters

Powder size	Charge ratio	Charge contents	Surfactant	Mill time	Mill type
304L: 15-53 μm	13:1	304L: 9.66g	Stearic acid: 0.11g	60 Hours	Planetary
Mo: 35-45 nm		Mo: 0.74g			

After the ball milling process is completed, the powder is formed, pressed and sintered using the parameters given in Figure 4.2. After the pellets are sintered, they are they are placed into a 0.5 inch thick plate of 304L stainless steel plate that has been prepared with holes, like the one seen in Figure 4.2, to accept the pellets. This steel plate meets the ASTM A240/A240M-15 standard for pressure vessels and general applications and the composition of the 304L plate used is given in Table 3.3. The plate is then friction stir processed with compacts of 316L and the ball milled

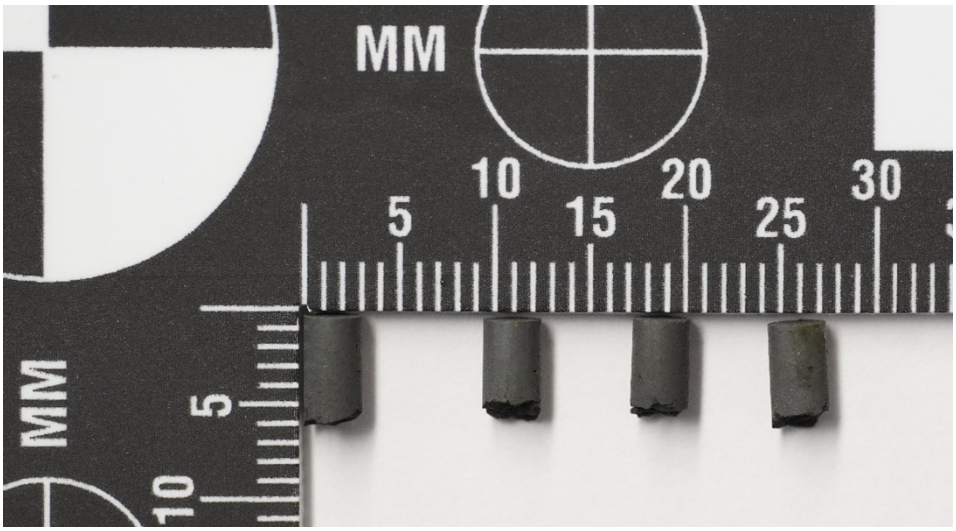

Figure 4.1: Pellets of ball milled 304L+Mo after sintering

mixture of 304L with molybdenum. The composition of the samples being tested can be found in Table 3.4.

Table 4.2: Press and sinter parameters

	304L+Mo	316L
Pressure (mt)	0.6	0.6
Pressure hold time (min)	1	1
Sinter temperature (°C)	750	750
Sinter time (min)	90	90
Ramp up (°C/min)	12	12
Dwell time (min)	30	30
Density (g/cm^3)	6.21	0

Table 4.3: Composition of Sandia 304L plate

Element	C	Si	Mn	P	S	Ni	Cr	Mo	N	Cu	Fe
Percent Weight	0.025	0.34	1.33	0.026	0.001	8.05	18.19	0.27	0.070	0.36	Bal

Table 4.4: Composition of samples to be tested

Sample	Compact Composition (%wt)	%wt of Mo in bulk sample	Dimensions (mm)
FSP 304L+Mo	304L: 97.75% Mo: 2.25 %	0.688	114 x 15.5 x 1
FSP 304L+316L	316L: 100%	0.5	114 x 15.5 x 1
304L	N/A	N/A	114 x 15.5 x 1

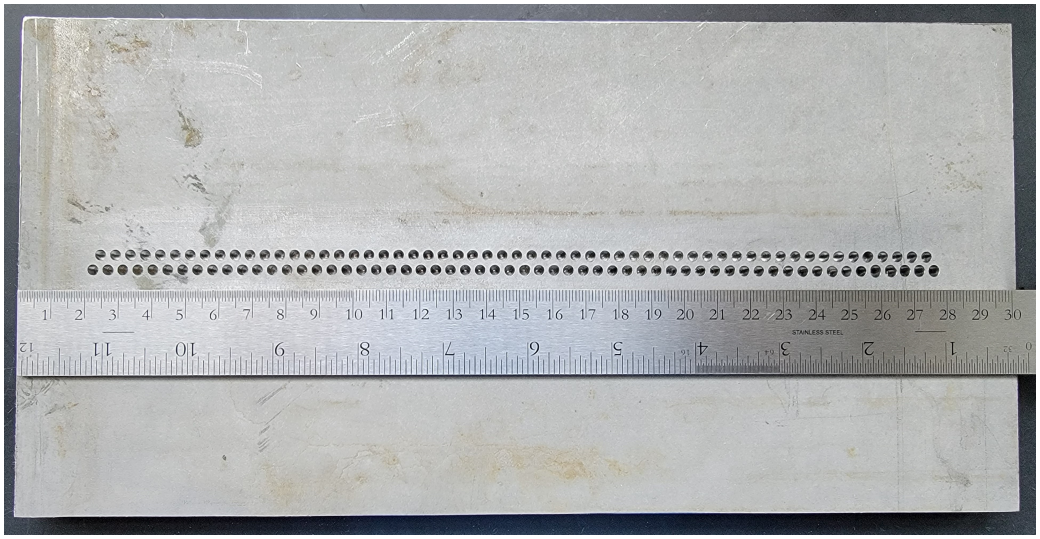

Figure 4.2: 304L stainless steel plate with holes drilled so that corrosion resistant elements can be added via pellets

4.2.1 Grain Size

Microstructure analysis of the samples was done using etching techniques developed by Frederick C. Bell and Daniel E. Sonon at the U.S. steel corporation, research laboratory [4]. Generally electrolytic etching in oxalic acid is the standard for revealing grain structure in austenitic stainless steel but if the steel is annealed then the etchant preferentially attack twins and not the grain boundaries. Therefore electrolytic etching using a 60% nitric acid solution was used. To prepare samples for electrolytic, they were ground using silicon carbide grinding paper starting at 180 grit and ending in 1200 grit. Polishing was performed using 3 µm and 1µm polycrystalline diamond suspension. For electrolytic, the power supply was set to a no-load voltage of 1 V. Each sample was submersed in a 60% nitric acid solution using stainless steel tweezers. The negative side of the power supply was attached to a 304L stainless steel cathode with dimensions of 7x1.5x1 cm. The positive side of the power supply was connected to the tweezers holding the samples. After submersion, the power supply was ad-

justed so a current density of 10 mA/cm2 was maintained. Samples were etched for four minutes, rinsed in deionized water, then methanol. A light microscope was used to determine if the grain structure was sufficiently etched. If under etched, samples were etched again for two minutes. After etching, samples were examined using a light microscope and ASTM standard E 112-96 [5] for determining average grain size was used. Several micrographs were taken using an optical light microscope of each sample to obtain a statistically sound estimate of the grain size. The circular intercept procedure from ASTM E112-96 was used to determine the mean lineal intercept value, $\bar{l}$. Statistical analysis was performed using standard deviation (Equation 4.2), 95% confidence interval (Equation 4.3), and relative accuracy (Equation 4.4). The ASTM E112-96 standard recommends that the relative accuracy is 10% or lower to be considered acceptably precise for most purposes. The mean planar grain size ($\bar{d}$) is about 12% larger than $\bar{l}$ [6].

$$s = [\frac{\Sigma(X_i - \overline{X})^2}{n-1}]^{1/2} \tag{4.2}$$

$$95\%CI = \frac{t * s}{\sqrt{n}} \tag{4.3}$$

$$\%RA = \frac{95\%CI}{\overline{X}} * 100 \tag{4.4}$$

4.2.2 Expiremental

U-bend samples are prepared from the FSP plate where the base metal composition is given in Table 4.3 and the FSP U-bend samples composition is given in Table 4.4. U-bend samples are prepared by machining a strip from the FSP plate as can be seen in Figure 4.3 and cut to dimension found in Figure 4.4. The samples are then ground planar using 120 grit silicon carbide grinding paper. The polishing process begins at 220 grit and ends at 1200 grit. Polished samples are then first stage bent, see Figure 4.6, using a U-bend jig as can be seen in Figure. 4.5. U-bend samples are then bolted with the legs parallel, like in Figure 4.6. The bolt pins the U-bend creating stress along the curve. The U-bend samples are submerged in 225mL of 2.5 M H2SO4 + .5 M NaCl solution in a bottle with a screw on cap as seen in Figure 4.7(B). On regular intervals, the samples are removed from the acid and rinsed in deionized water and then placed into an ultra sonic cleaner to remove any corrosion products or detritus that would obscure micrographs. Micrographs were taken of the surface to highlight any microstructure changes like cracks.

U-bend samples will be subjected to two different potentials while submerged in 2.5 M sulfuric acid and 0.5 M sodium chloride. The first will be open circuit potential and samples will be evaluated for time to first crack, first crack length, time to total failure, and surface crack density. Using these metrics we will be able to evaluate how well the material resisted CISCC at open circuit potential. The second potential will be at a static 0.2 V while submerged in 2.5 M sulfuric acid and 0.5 M sodium chloride. This will reveal information about the kinetics of passivation given by the equation:

$$I(t) = I_o t^k \tag{4.5}$$

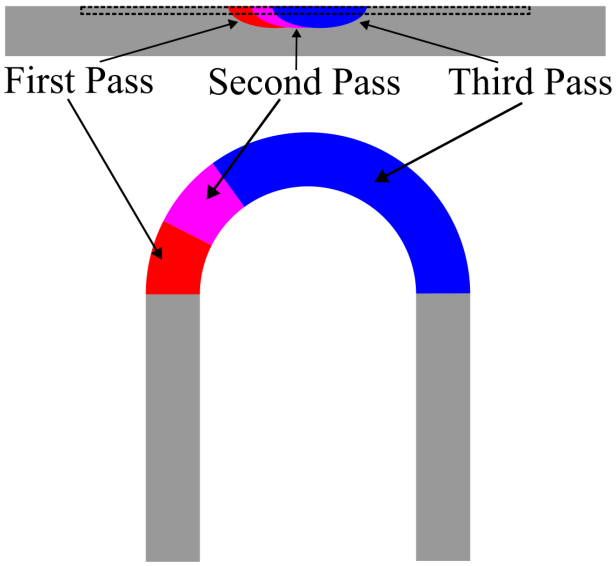

Figure 4.3: Cross sectional view of where the U-bend samples are machined from and approximate locations of stir zones before and after bending

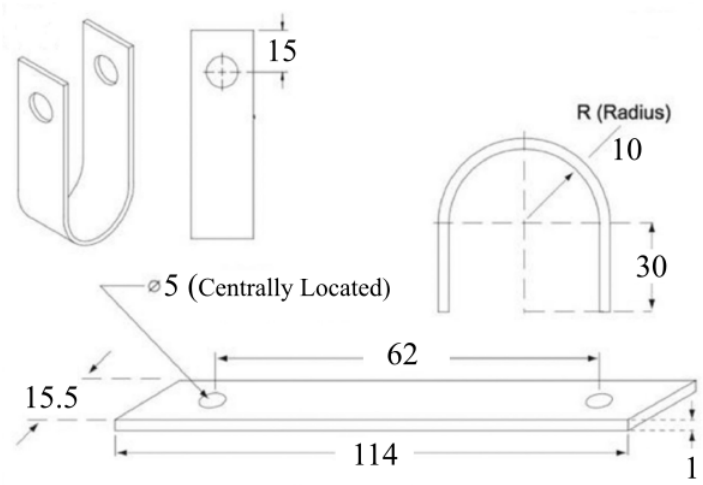

Figure 4.4: U-bend are cut to shape and bent with these dimensions

Where k is the passivation kinetics constant and describes how fast a material develops a passive layer. The more negative the value for k, the fast the pasivation layer will form. The value for potential was chosen because it was near the bottom of the

Figure 4.5: Jig used to repeatably bend samples to the correct size

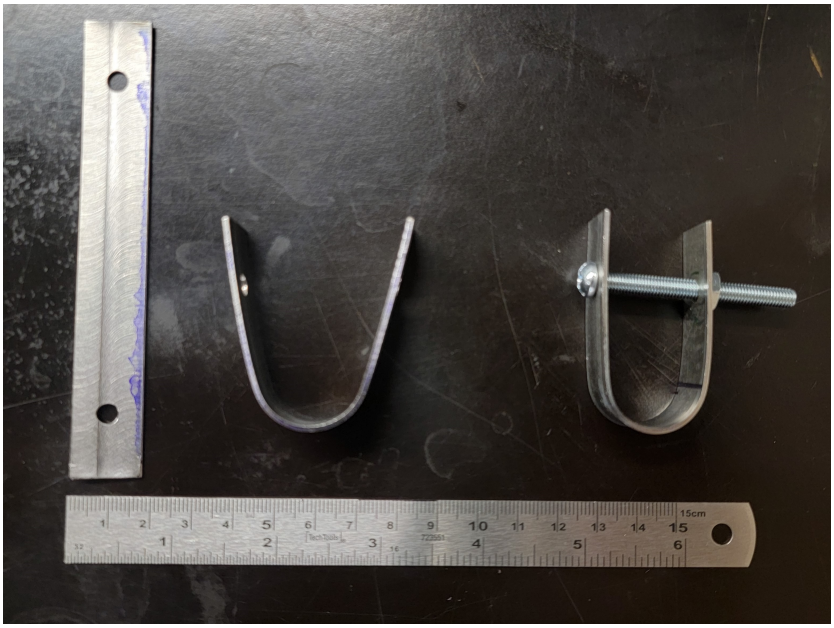

Figure 4.6: Left: U-bend samples before bending. Middle: U-bend samples after first stage bend. Right: U-bend samples completely bent and bolted to retain shape.

passivation region when cyclic polarization was performed, see Figure 3.13. This region will have meta stable pit nucleation where stress corrosion cracking might happen

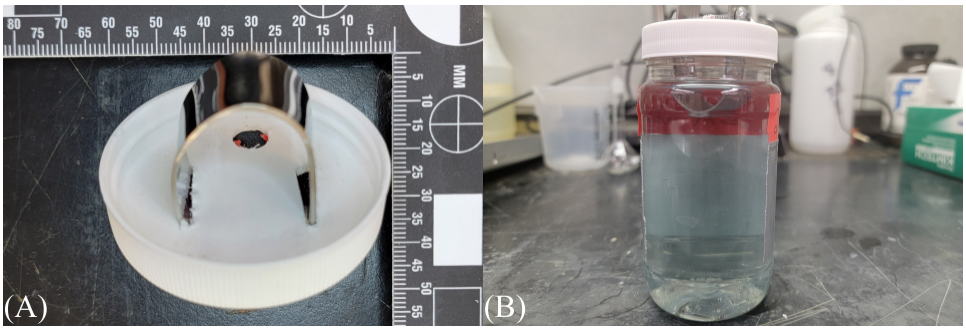

Figure 4.7: (A): After polishing and final stage bending of the samples, they are bolted so the legs of the sample are parallel. (B): A cap is used to hold the sample in the sulfuric acid in the bottle

4.3 Results and Discussion

4.3.1 Open Circuit Potential

U-bend test are a useful for comparing major differences in the resistance of CISCC. Using this technique, we can compare the three samples and their ability to withstand cracking in a corrosive environment. During the prolonged exposure to 2.5 M sulfuric acid and 0.5 M sodium chloride solution, the open circuit was measured using a $Ag/AgCl$ reference electrode to compare the corrosion potential of all three samples. The Figure 4.8 reveals that the 304L sample has the least noble corrosion potential when compared with the other samples. the FSP 304L+Mo and FSP 304L+3016L samples had very similar corrosion potentials through the entirety of the test. The Figure 4.8 shows some strange spikes in the potential at 2.5 hours for the FSP 304L+316L sample that settles after after a couple of hours. At 25 hours the FSP 304L+Mo and FSP 304L+316L spike again but settle. These spikes coincide with when the samples are removed from the acid to take micrographs and the open circuit potential was measured immediately after samples were re-submerged in the acid.

4.3.1.1 Microstructure

The more resistant a material is to CISCC the longer it will take to form surface cracks and the longer until total failure. Research suggests that the addition of molybdenum will improve CISCC resistance by increasing the PREN and improving the stacking fault energy[9], but Table 4.5 illustrates that 304L is the last to crack of the samples. This is an unexpected result considering 304L has the least amount of molybdenum compared with the other samples. Using micrographs, Tables 4.6-4.8 show that 304L

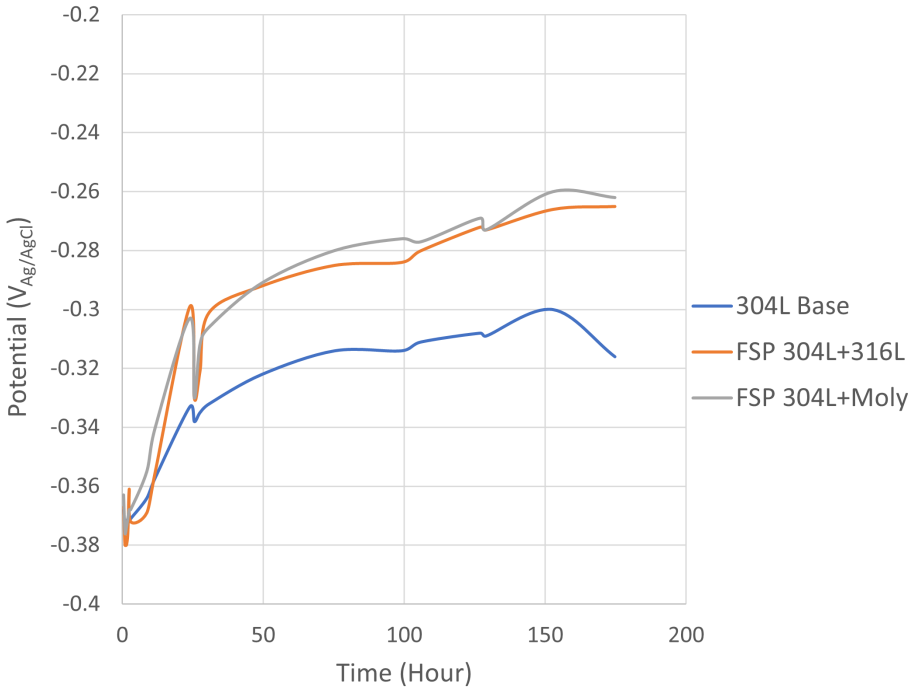

Figure 4.8: Plot of open circuit potential over the duration of the test

has lower SCD when compared to FSP 304L+Mo and FSP 304L+316L. At 174.75 hours, FSP 304L+Mo has 2.4 times as much SCD. FSP 304L+316L has 3 times as much SCD when compared to 304L. It should be noted that the SCD of all samples will be higher than what this report states because of the limitations of the optical microscope. Figure 4.8 reveals that 304L is less noble than FSP 304L+Mo and FSP 304L+316L. At 175.75 hours of solution exposure, 304L had a corrosion potential of -0.316 V while FSP 304L+Mo and FSP 304L+316L had -0.262 V and -0.265 V respectively. This result seems incongruous when compared to the other results because the more noble the corrosion potential, the more resistance to corrosion a material is yet the data from Tables 4.5-4.8 suggest that 304L has superior CISCC resistance.

Table 4.5: Details of first crack observed, time to total failure and first crack length.

Sample	Time to First Crack(hours)	Time to Total Failure (hours)	First Crack Length (μm)
304L	47.75	267.5	115
FSP 304L+Mo	30	-	78
FSP 304L+316L	30	-	65

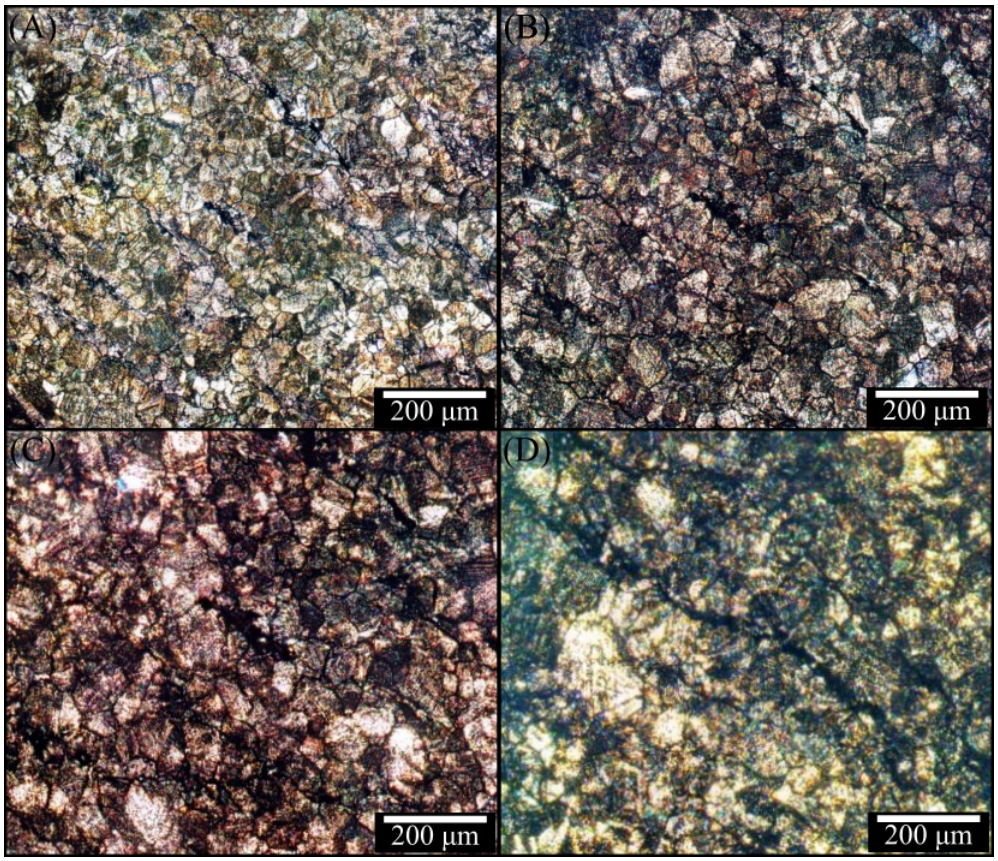

Figure 4.9: Micrograph of 304L sample after (A): 102.75 hours (B): 127 hours (C): 152.75 hours (D): 174 hours

Table 4.6: Evolution of SCD over time of 304L sample

Sample	Time (hour)	Surface Crack Density ($\mu m/\mu m^2$)
304L	78.75	0.0046
	102.75	0.0209
	127	0.0208
	152.75	0.0264
	174	0.0152

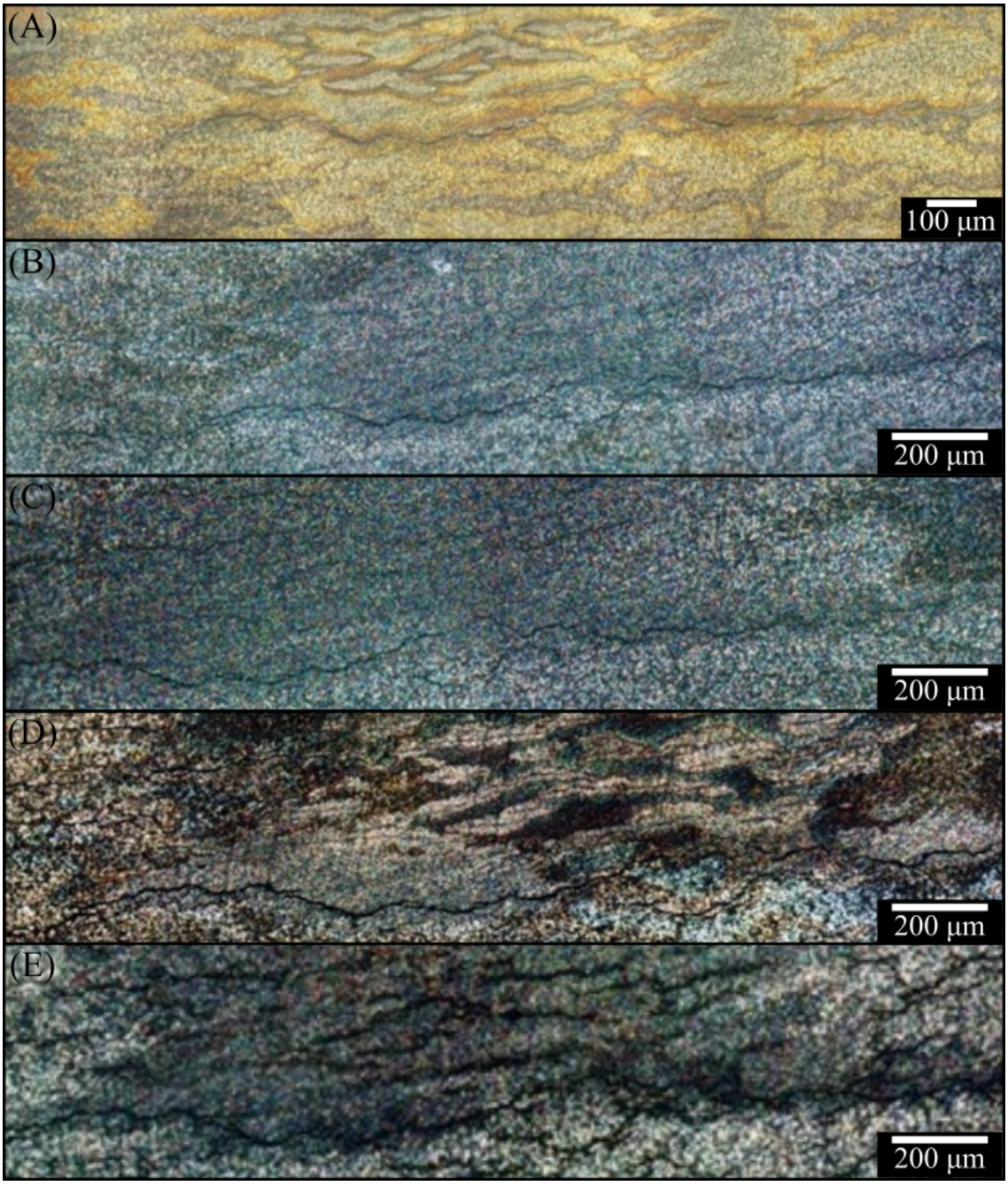

Figure 4.10: Micrograph of FSP 304L+Mo sample after (A):78.75 hours (B): 102.75 hours (C): 127 hours (D): 152.75 hours (E): 174 hours

Table 4.7: Evolution of SCD over time of FSP 304L+Mo

Sample	Time (hour)	Surface Crack Density ($\mu m/\mu m^2$)
FSP 304L+Mo	78.75	0.0190
	102.75	0.0284
	127	0.0329
	152.75	0.0387
	174	0.0369

Table 4.8: Evolution of SCD over time of FSP 304L+316L

Sample	Time (hour)	Surface Crack Density ($\mu m/\mu m^2$)
FSP 304L+316L	78.75	0.0323
	102.75	0.0409
	127	0.0451
	152.75	0.0511
	174	0.0465

Figure 4.11: Micrograph of FSP 304L+316L sample after (A): 102.75 hours (B): 127 hours (C): 152.75 hours (D): 174 hours

4.3.2 Poteniostatic Analysis

Potentiostatic testing highlights details of the passive layer of the U-bend samples like the passivation kinetics, k, found in the following equation.

$$I = I_o t^k \tag{4.6}$$

The more negative the value for k, the faster the passive layer grows. By observing Figure 4.12 we see that for the first 100 seconds the current is decreasing the entire time and the passivation constant is -0.516. This signifies that the passive layer is growing and becoming thicker. If we compare the passivation kinetics of the 304L sample at day 1, Figure 4.12, with the FSP 304L+316L sample at day 1, Figure 4.22, we see that the while both show passive layer growth with time, the FSP 304L+316L sample is passivating slower than the 304L sample. After the initial 100 seconds the behavior of current changes based on the integrity of the passive layer. If we observe Figure 4.15, we can see that after 100 seconds, the current begins to oscillate slightly. These oscillations are a sign that the passive layer is beginning to fail. The current is still decreasing until just before 1000 seconds, but begins to increase and the oscillations become more frenetic as the time approaches 10,000 seconds. These spikes in the current are indicative of pit nucleation and passive layer failure. When observing the passivation kinetics over all 5 days, we see that 304L has mostly negative values for the passivation constant where as the FSP 304L+316L samples have smaller passivation constants oscillating around zero. The FSP 304L+Mo samples tended to have the most negative passivation constant.

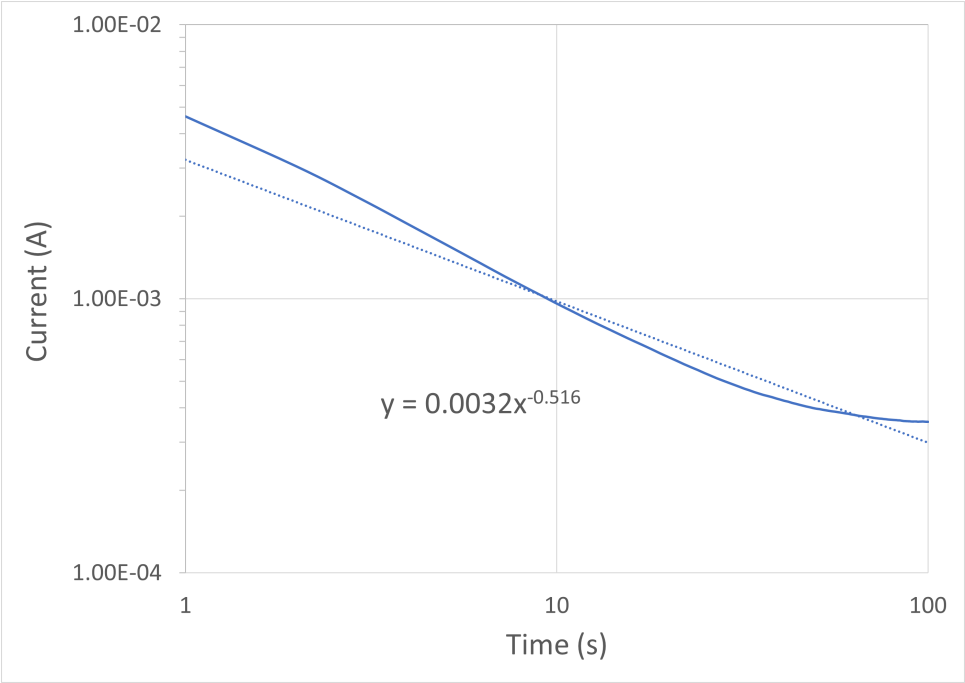

Figure 4.12: First 100 seconds of day one of potentiostatic test of 304L U-bend sample.

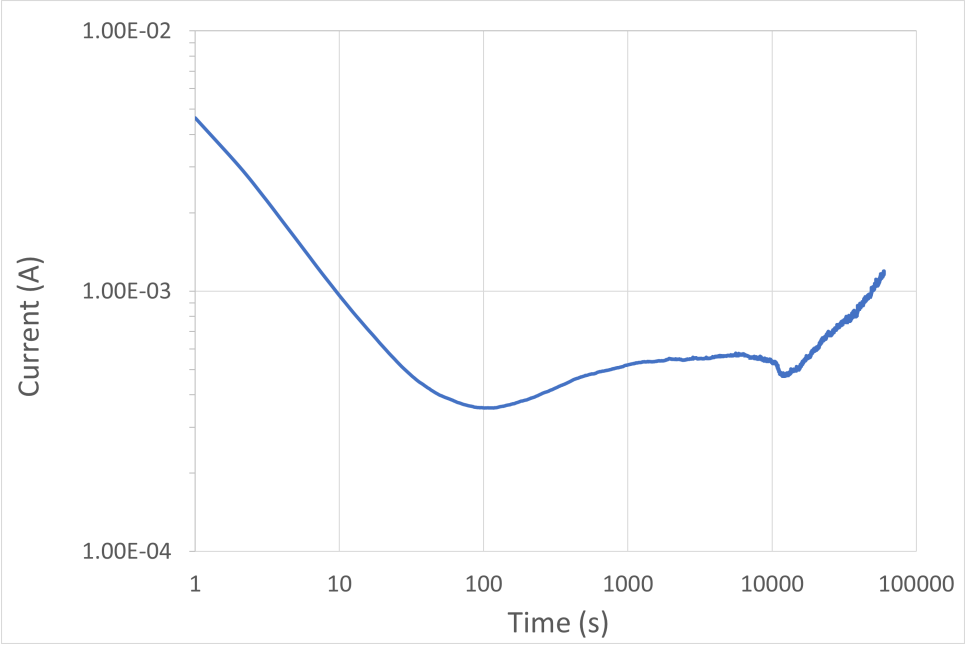

Figure 4.13: Day one of potentiostatic test of 304L U-bend sample.

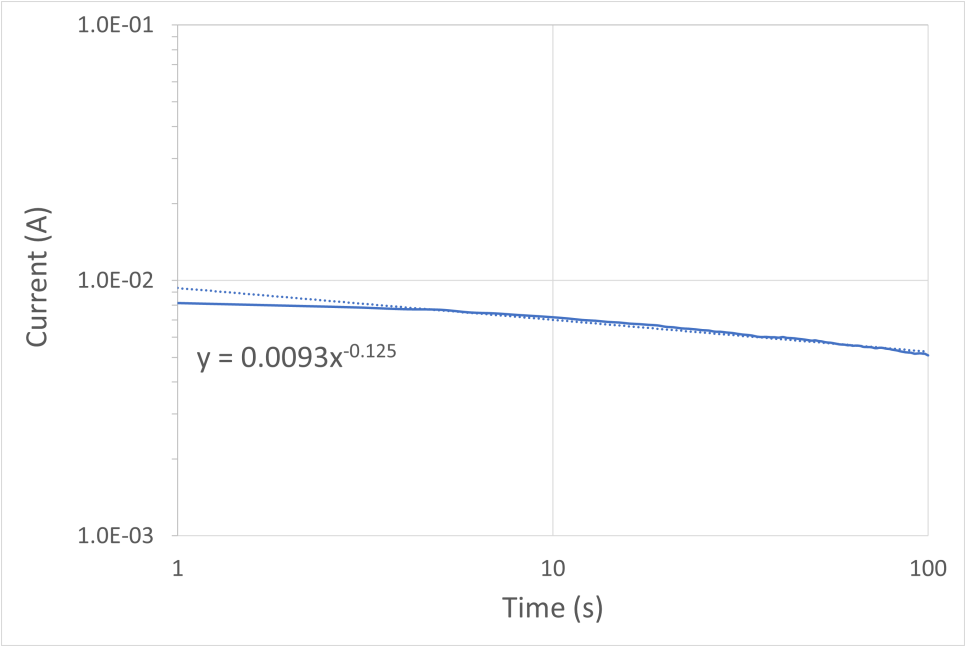

Figure 4.14: First 100 seconds of day two of potentiostatic test of 304L U-bend sample.

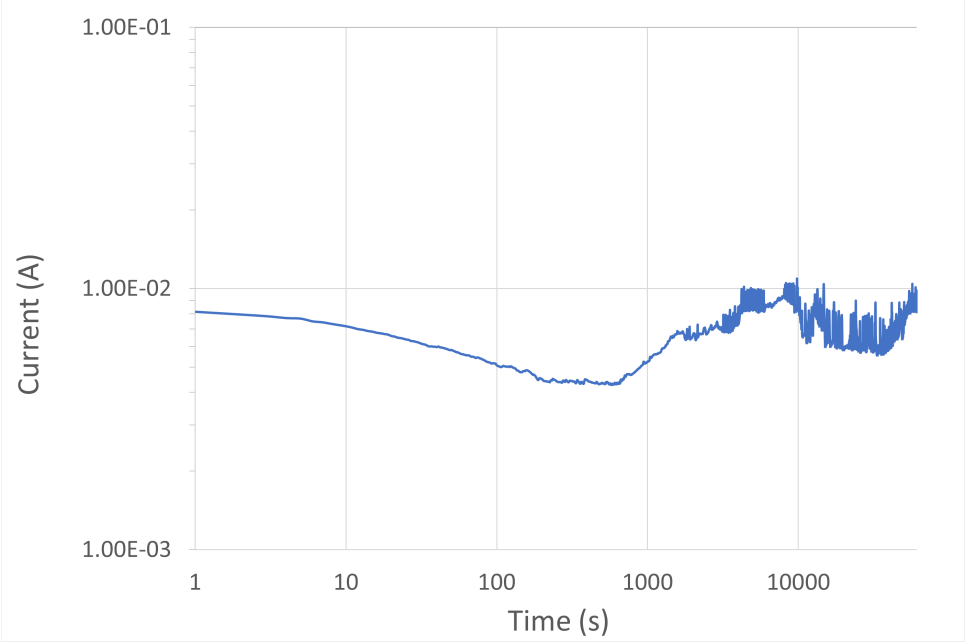

Figure 4.15: Day two of potentiostatic test of 304L U-bend sample.

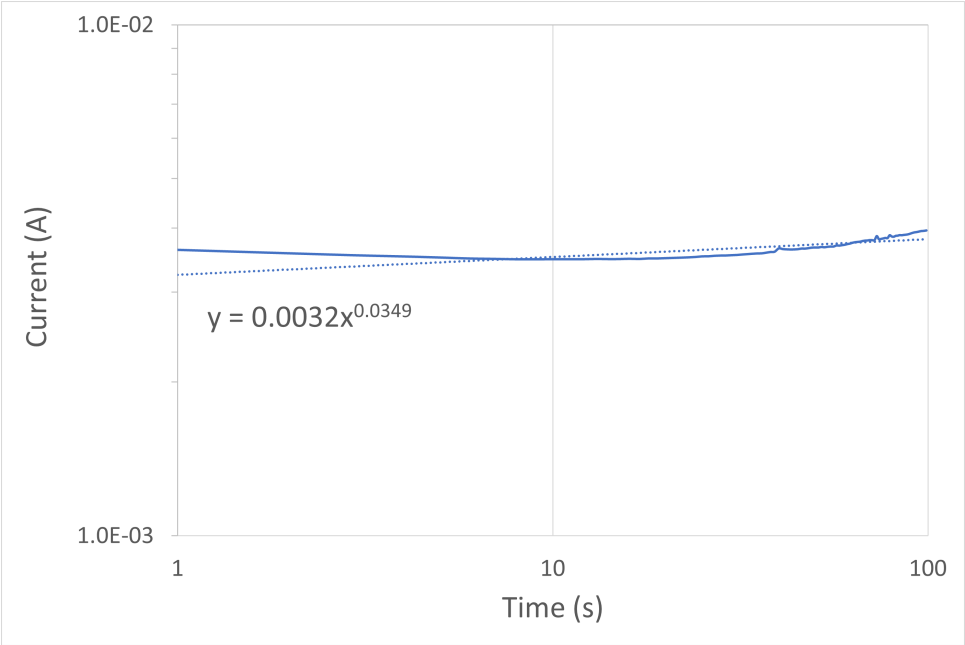

Figure 4.16: First 100 seconds of day three of potentiostatic test of 304L U-bend sample.

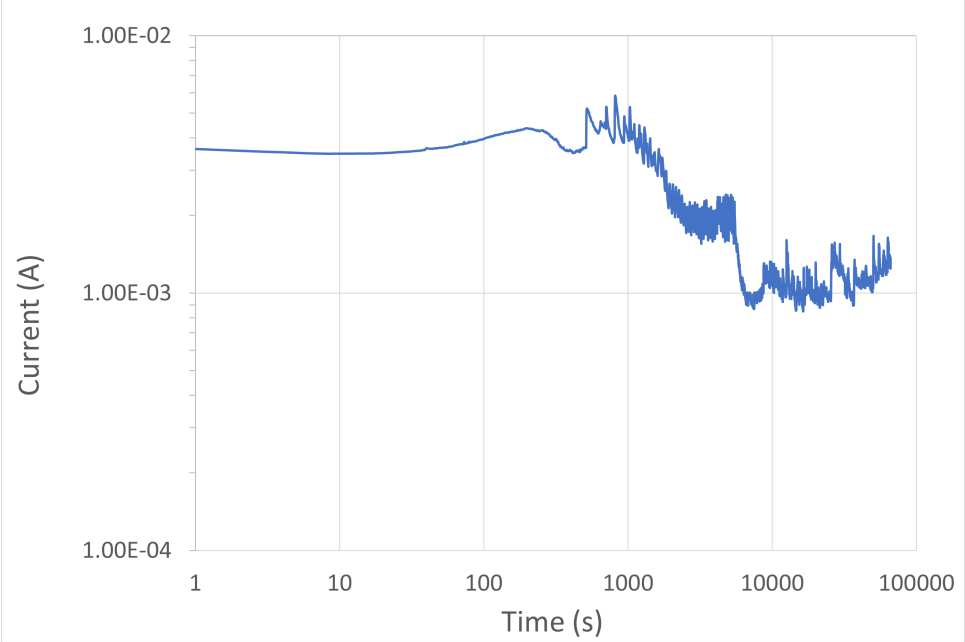

Figure 4.17: Day three of potentiostatic test of 304L U-bend sample.

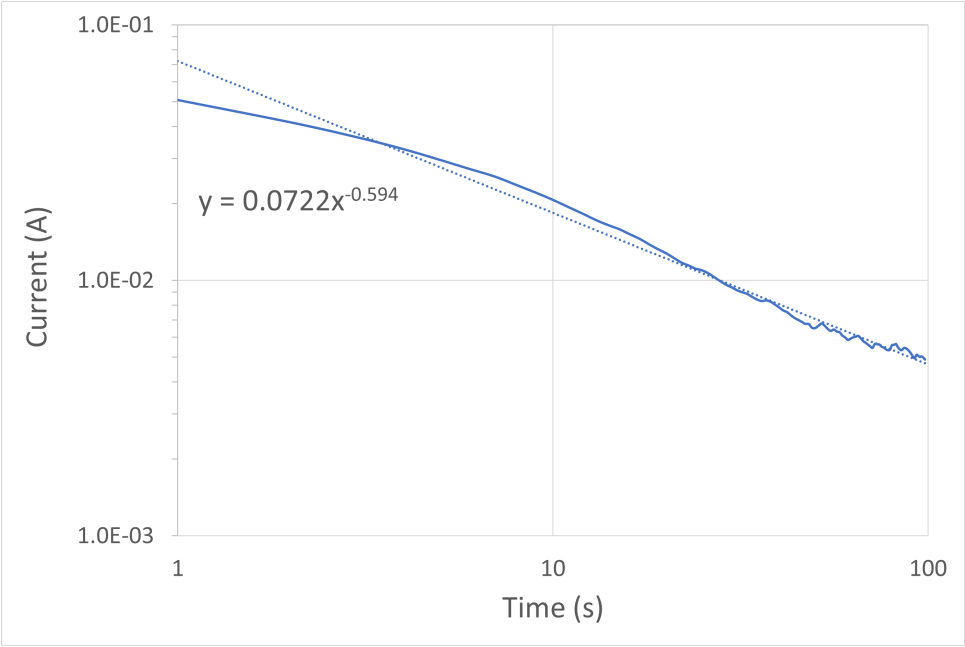

Figure 4.18: First 100 seconds of day four of potentiostatic test of 304L U-bend sample.

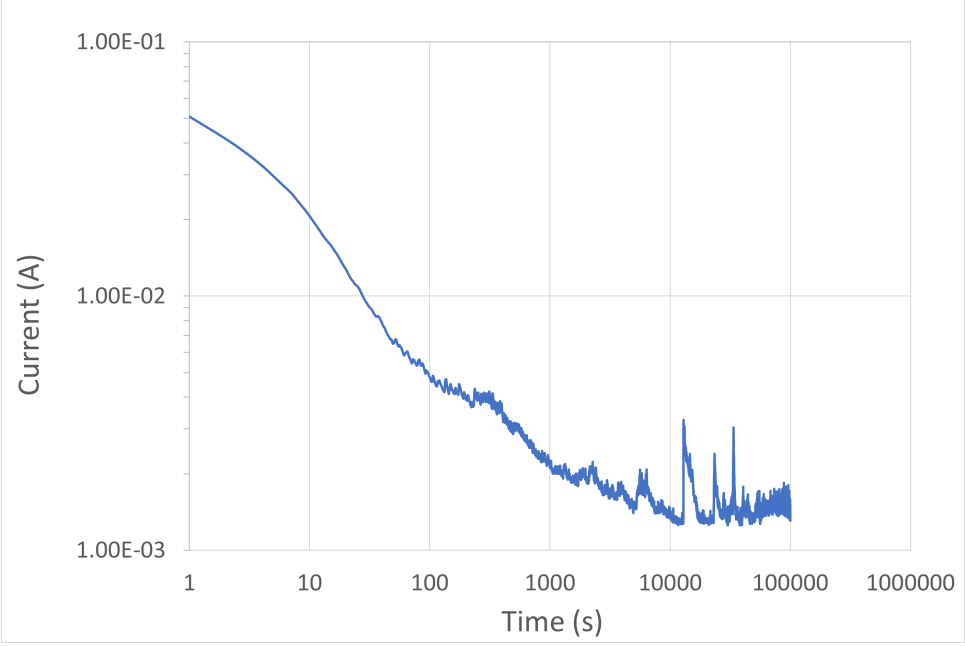

Figure 4.19: Day four of potentiostatic test of 304L sample.

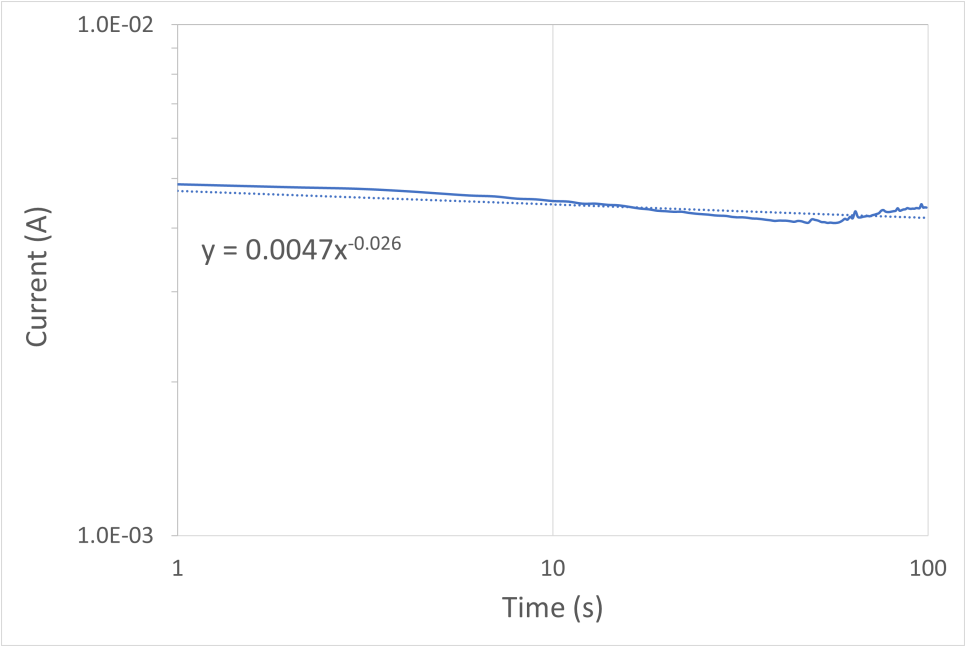

Figure 4.20: First 100 seconds of day five of potentiostatic test of 304L U-bend sample.

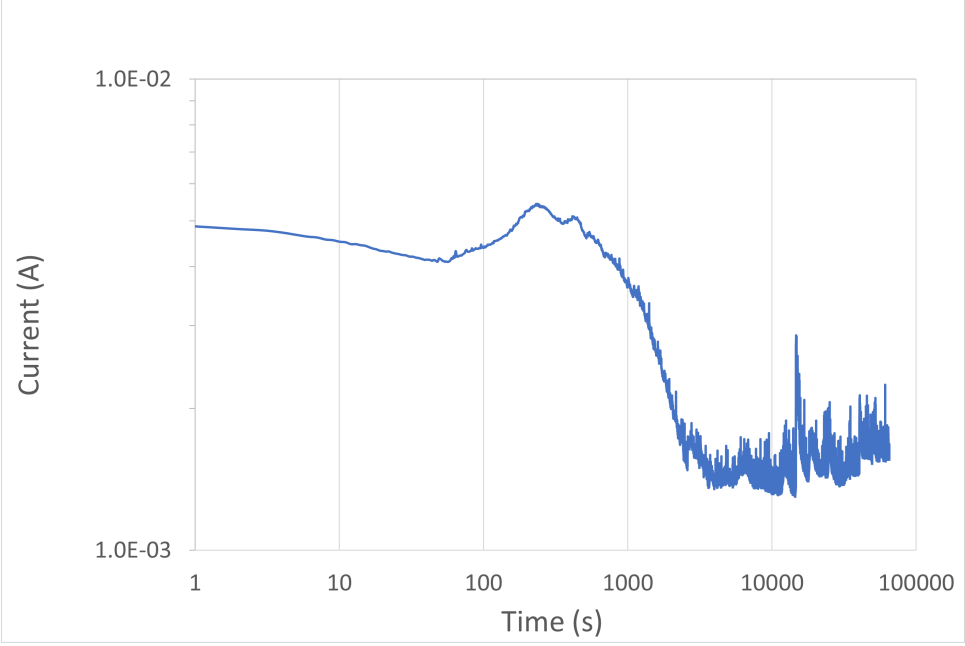

Figure 4.21: Day five of potentiostatic test of 304L U-bend sample.

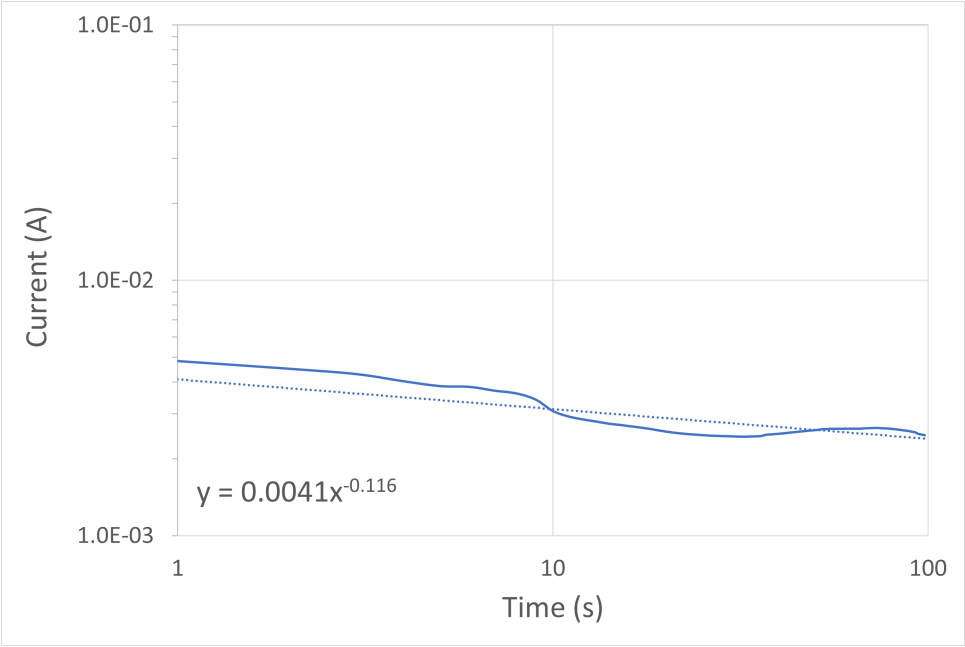

Figure 4.22: First 100 seconds of day one of potentiostatic test of FSP 304L+316L U-bend sample.

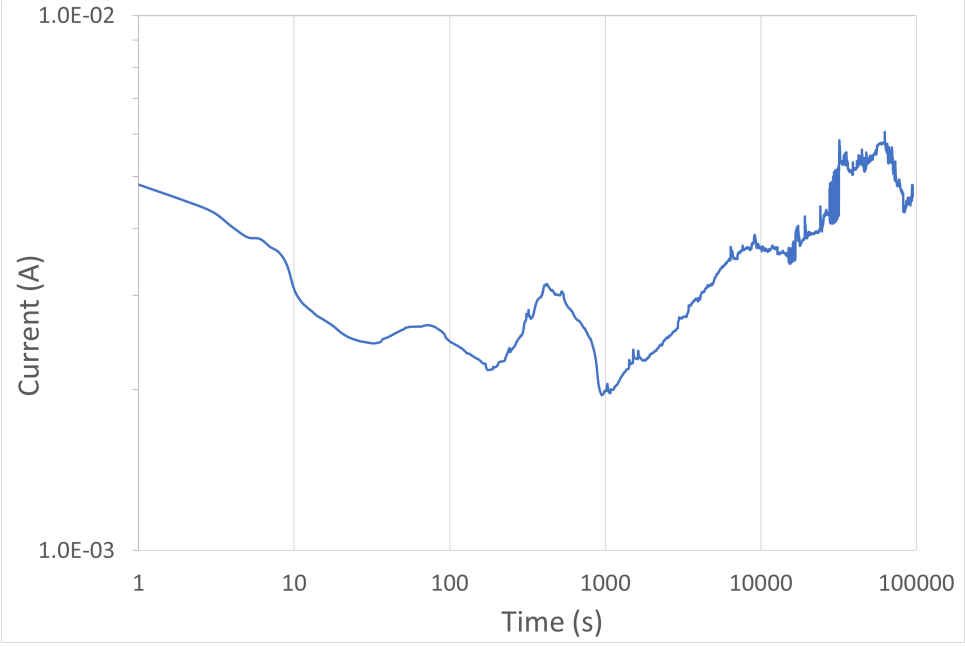

Figure 4.23: Day one of potentiostatic test of FSP 304L+316L U-bend sample.

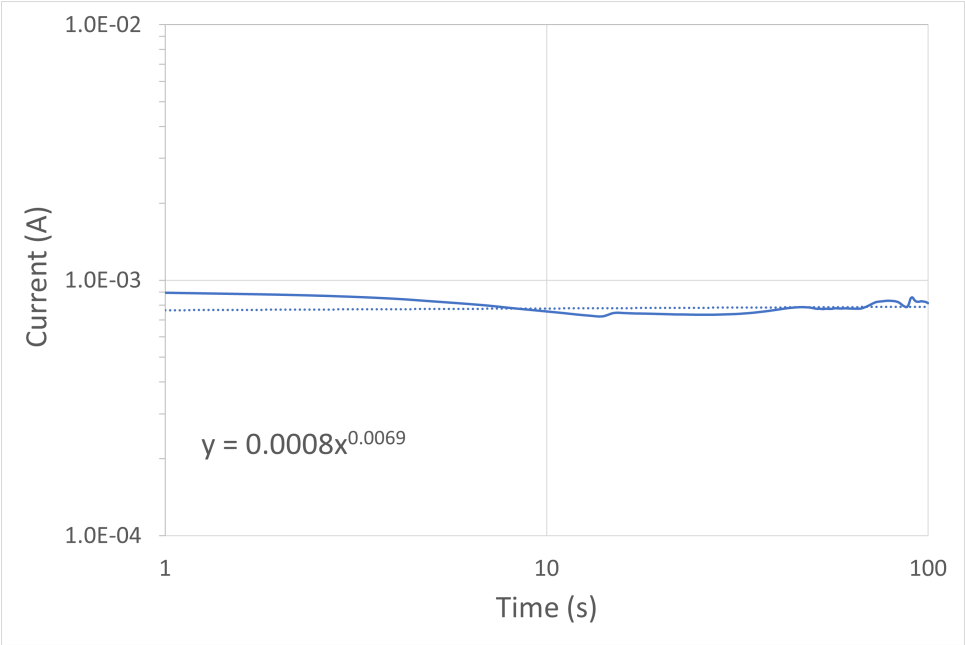

Figure 4.24: First 100 seconds of day two of potentiostatic test of FSP 304L+316L U-bend sample.

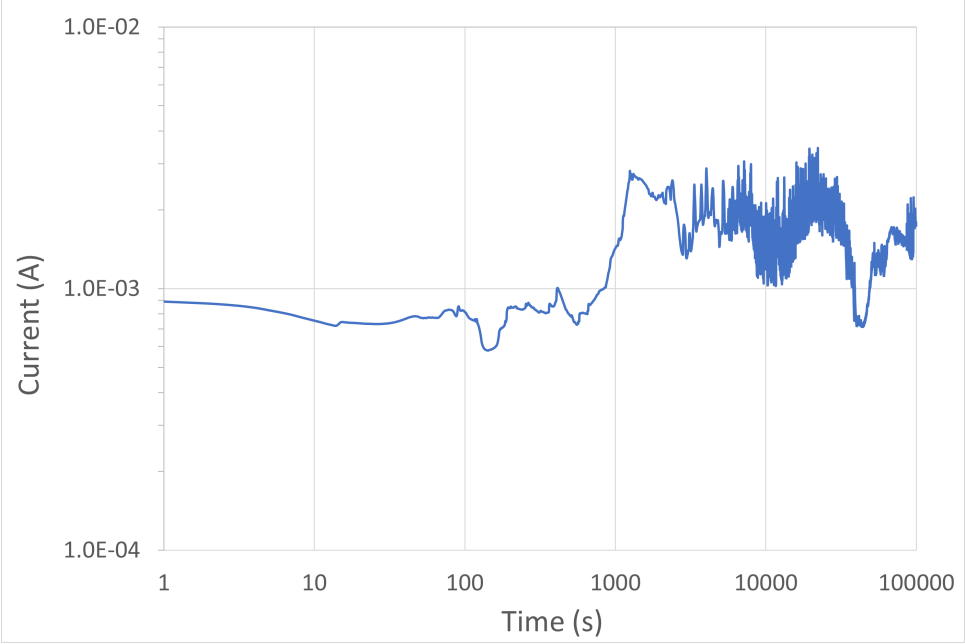

Figure 4.25: Day two of potentiostatic test of FSP 304L+316L U-bend sample.

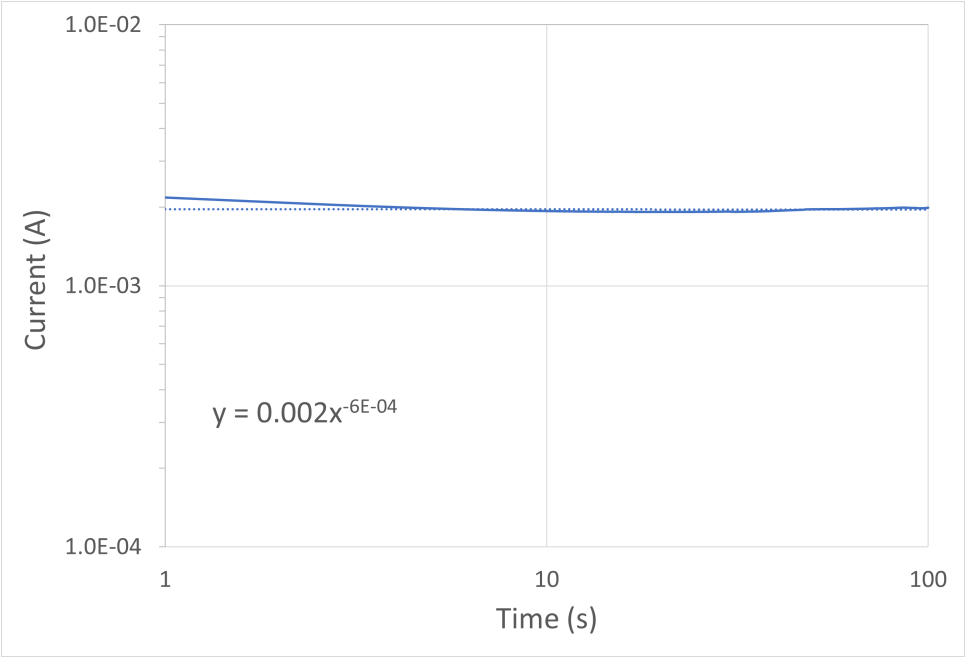

Figure 4.26: First 100 seconds of day three of potentiostatic test of FSP 304L+316L U-bend sample.

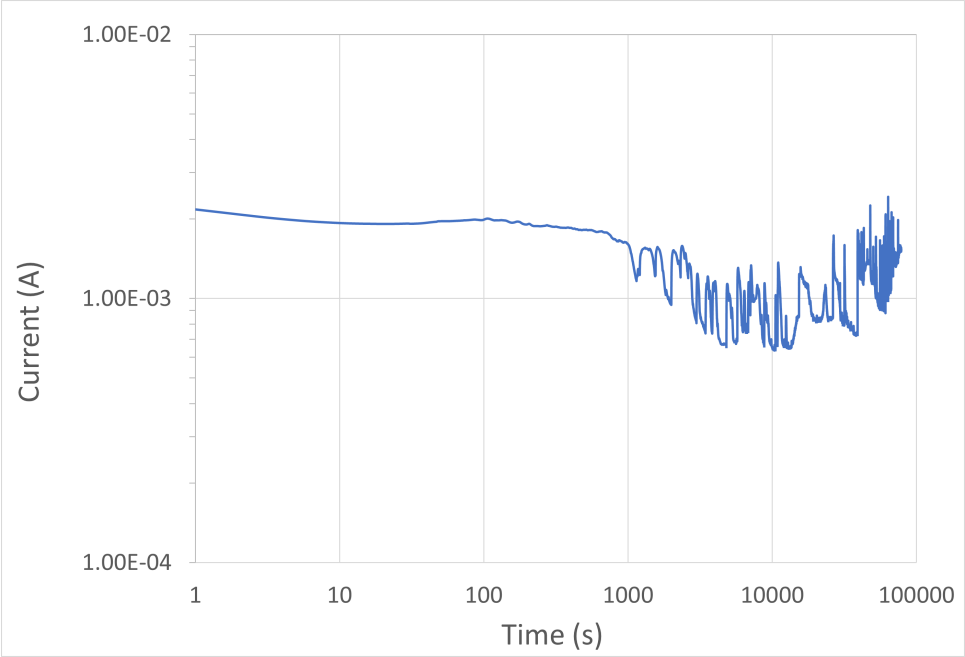

Figure 4.27: Day three of potentiostatic test of FSP 304L+316L U-bend sample.

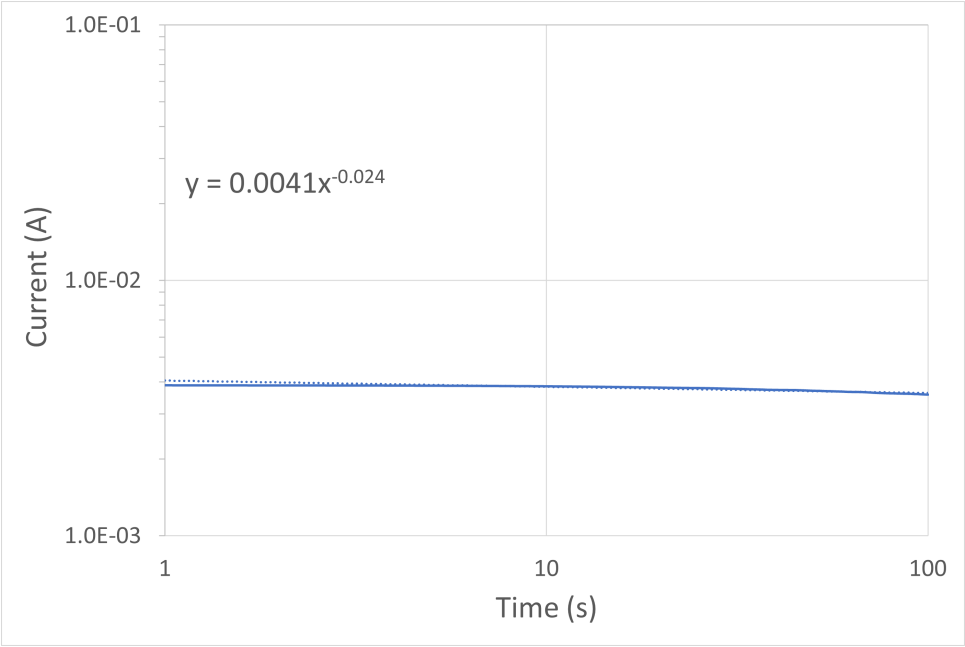

Figure 4.28: First 100 seconds of day four of potentiostatic test of FSP 304L+316L U-bend sample.

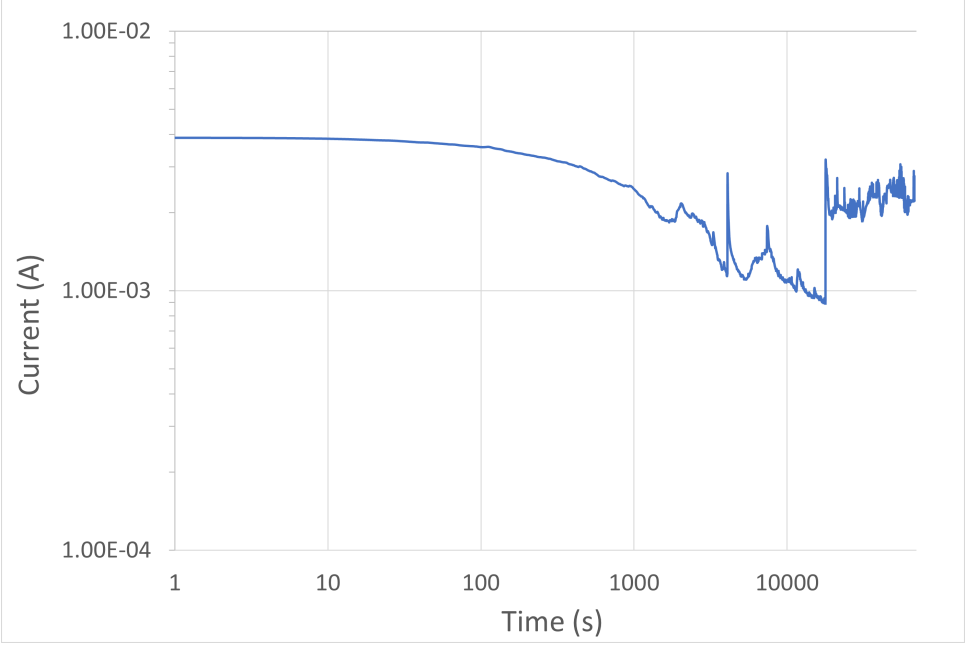

Figure 4.29: Day four of potentiostatic test of FSP 304L+316L U-bend sample.

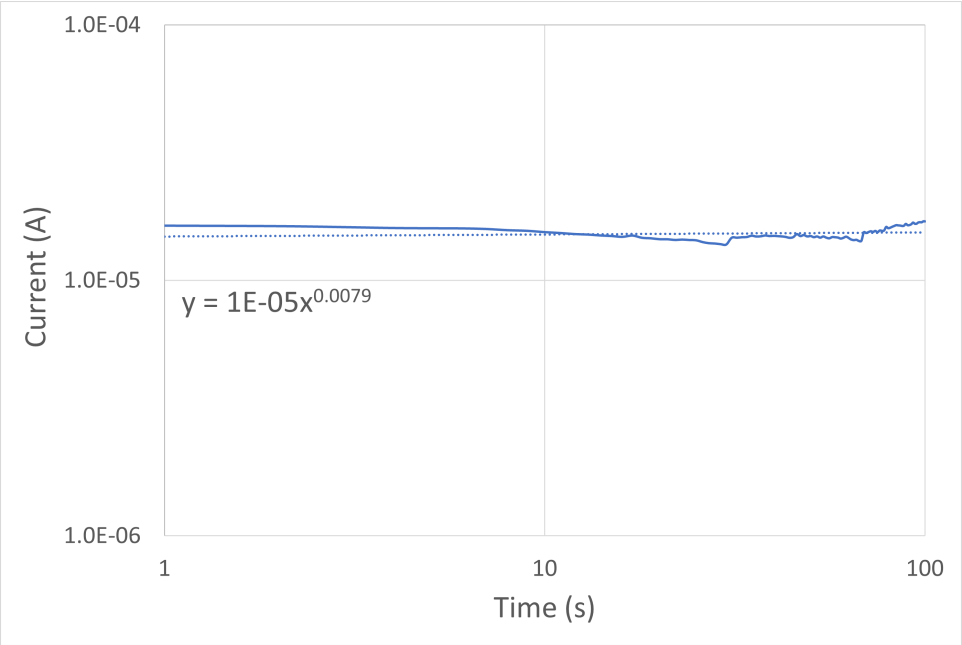

Figure 4.30: First 100 seconds of day five of potentiostatic test of FSP 304L+316L U-bend sample.

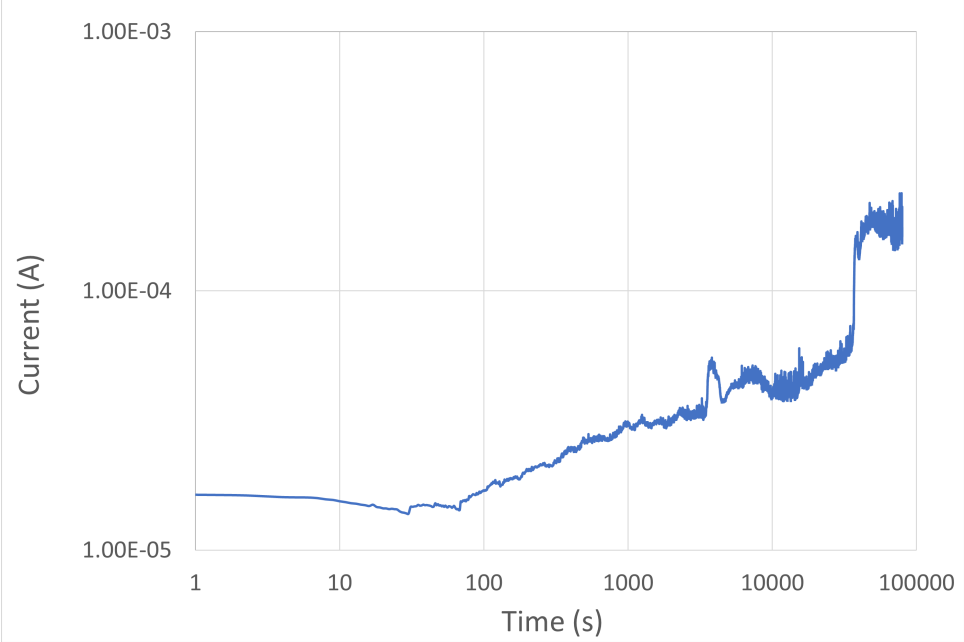

Figure 4.31: Day five of potentiostatic test of FSP 304L+316L U-bend sample.

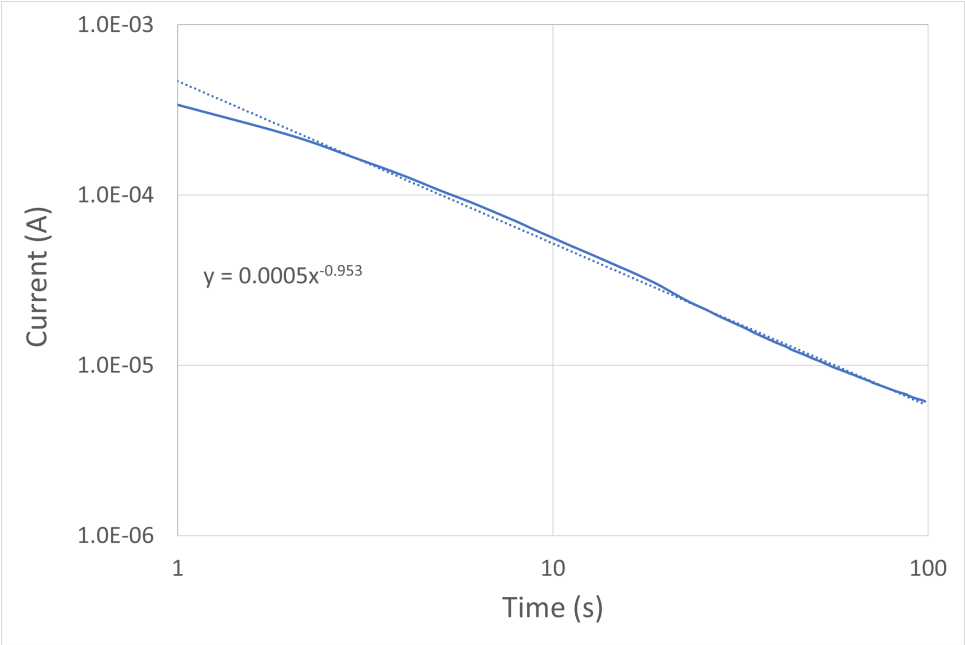

Figure 4.32: First 100 seconds of day one of potentiostatic test of FSP 304L+Mo U-bend sample.

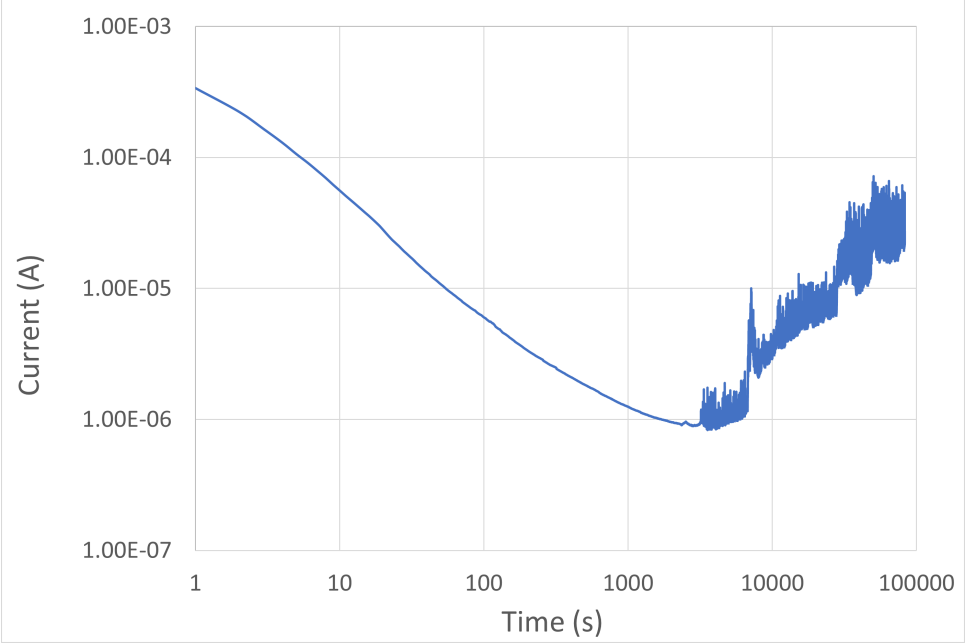

Figure 4.33: Day one of potentiostatic test of FSP 304L+Mo U-bend sample.

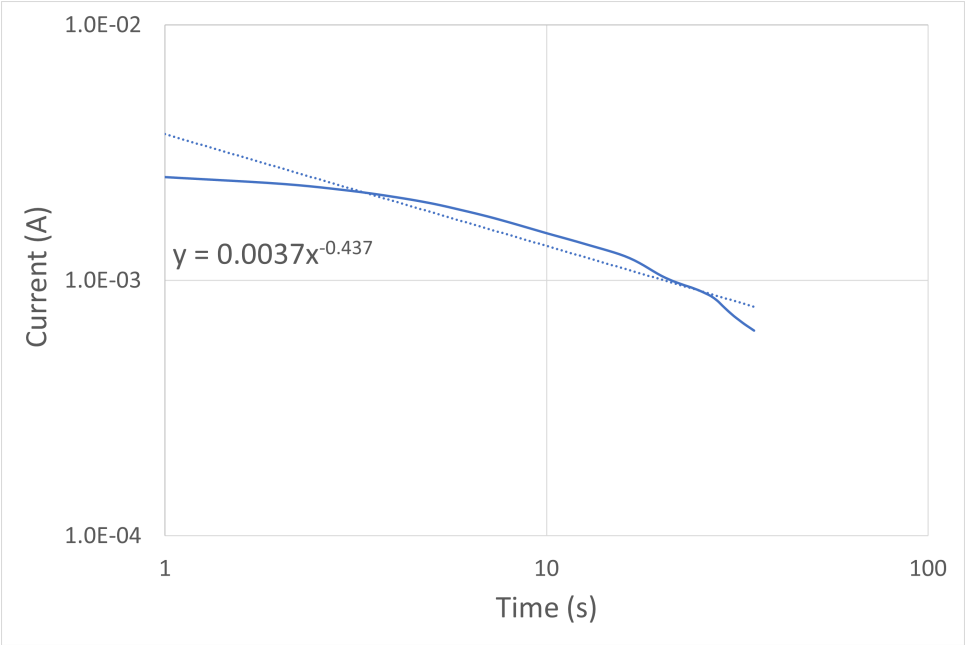

Figure 4.34: First 100 seconds of day two of potentiostatic test of FSP 304L+Mo U-bend sample.

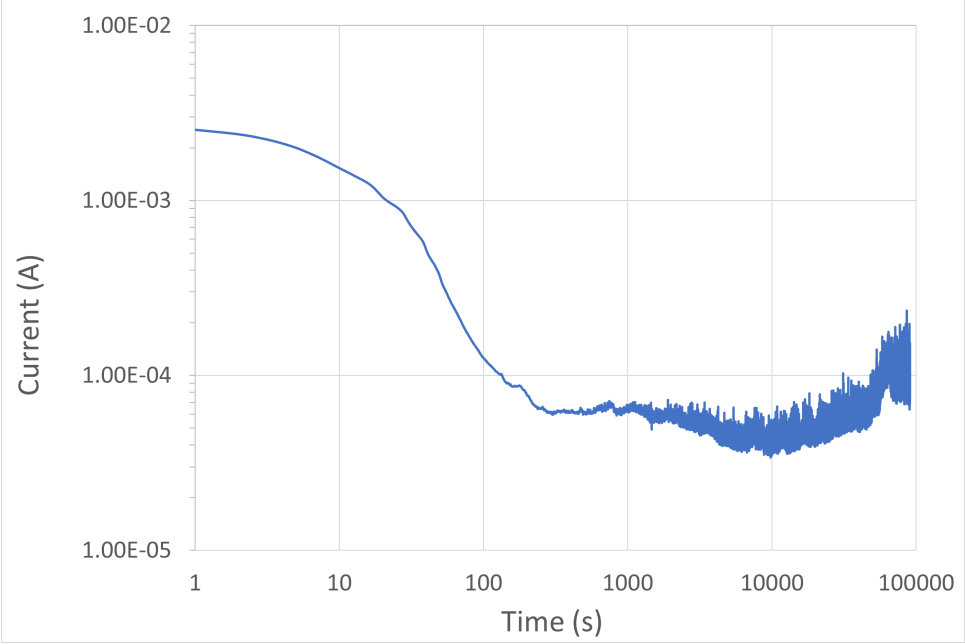

Figure 4.35: Day two of potentiostatic test of FSP 304L+Mo U-bend sample.

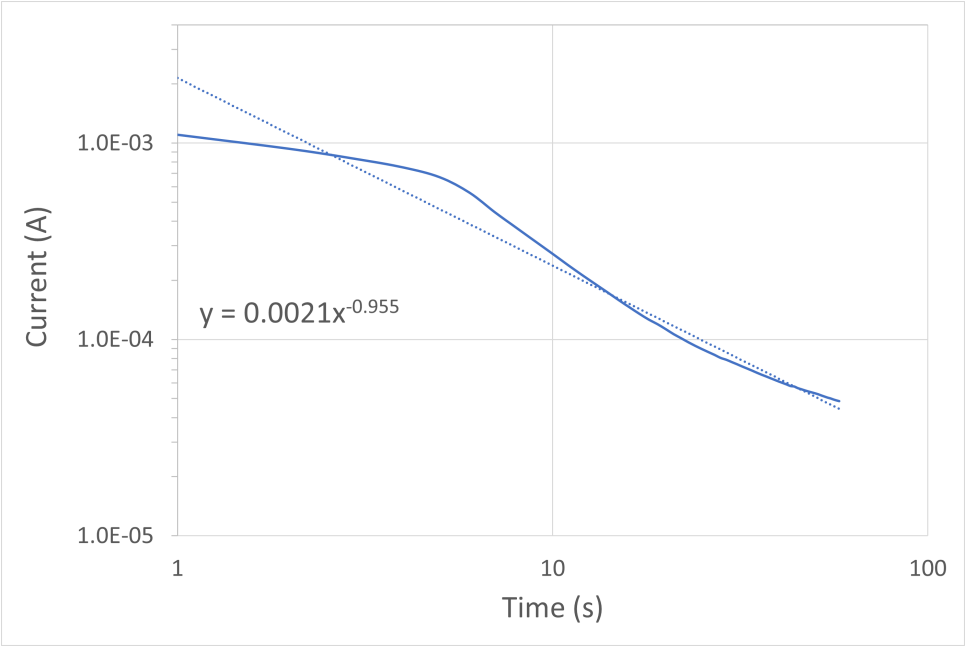

Figure 4.36: First 100 seconds of day three of potentiostatic test of FSP 304L+Mo U-bend sample.

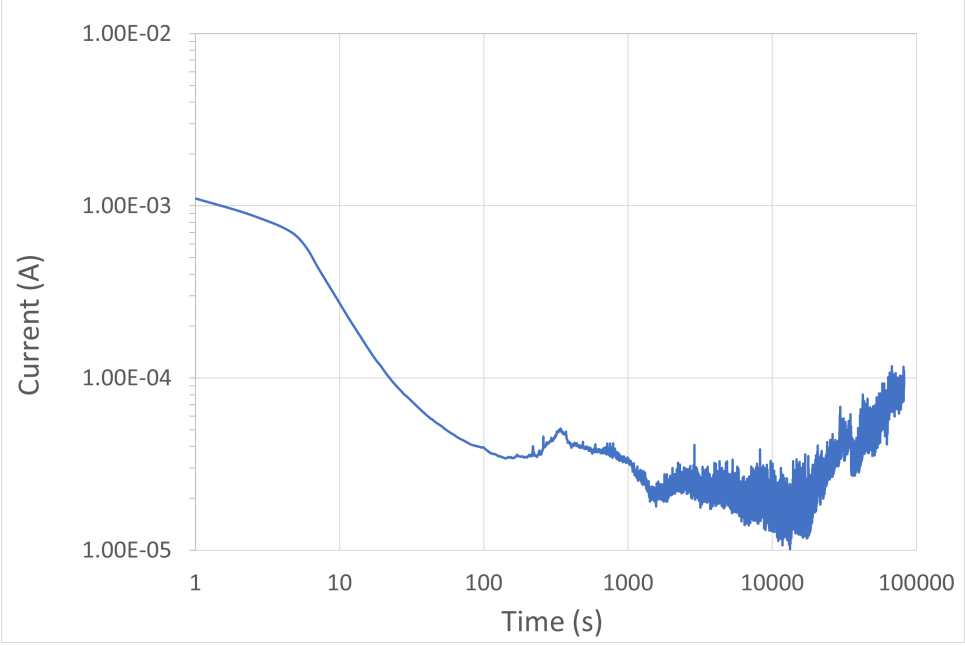

Figure 4.37: Day three of potentiostatic test of FSP 304L+Mo U-bend sample.

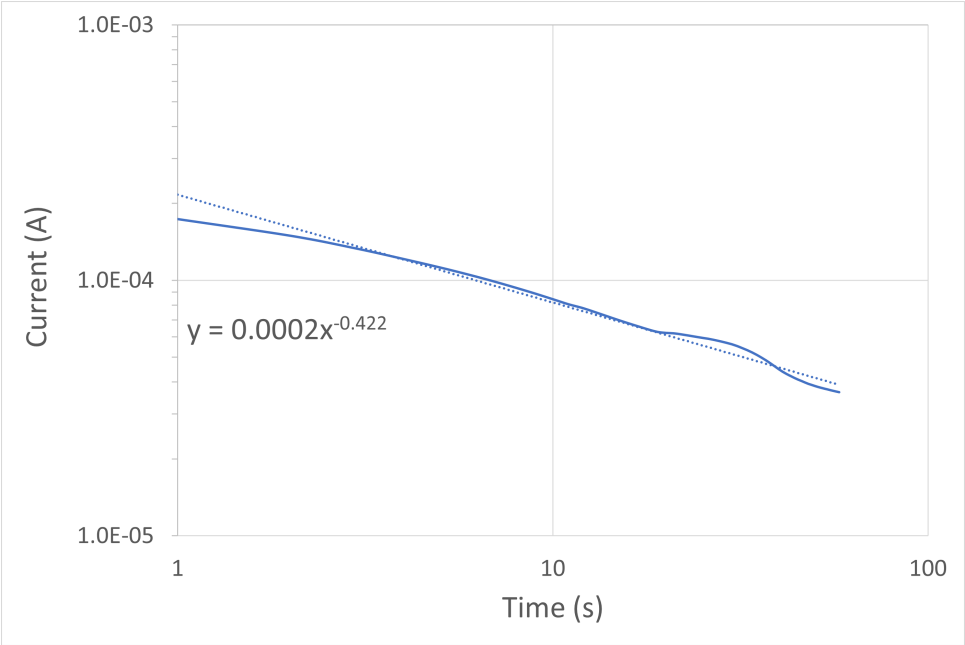

Figure 4.38: First 100 seconds of day four of potentiostatic test of FSP 304L+Mo U-bend sample.

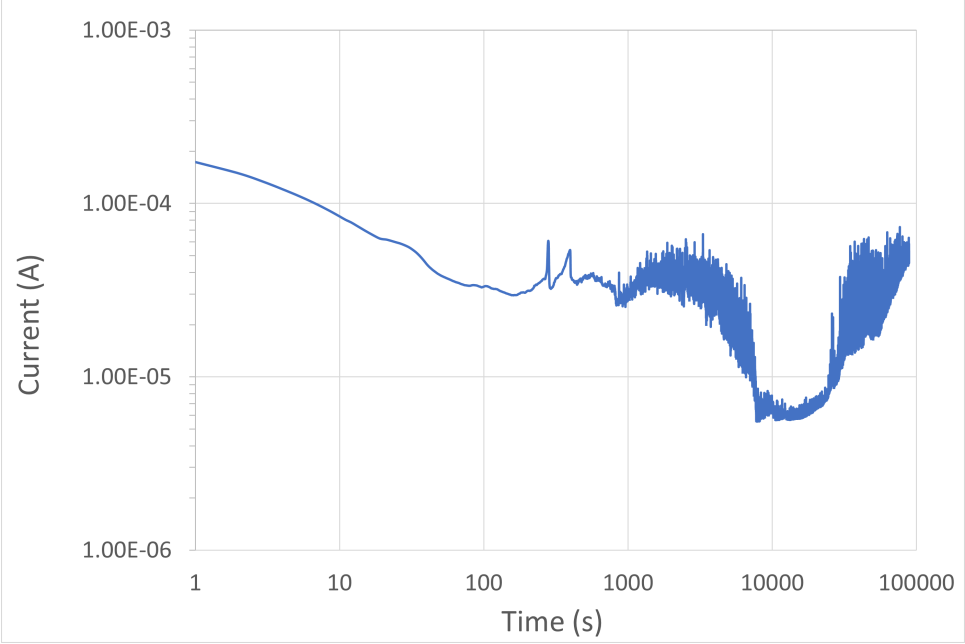

Figure 4.39: Day four of potentiostatic test of FSP 304L+Mo U-bend sample.

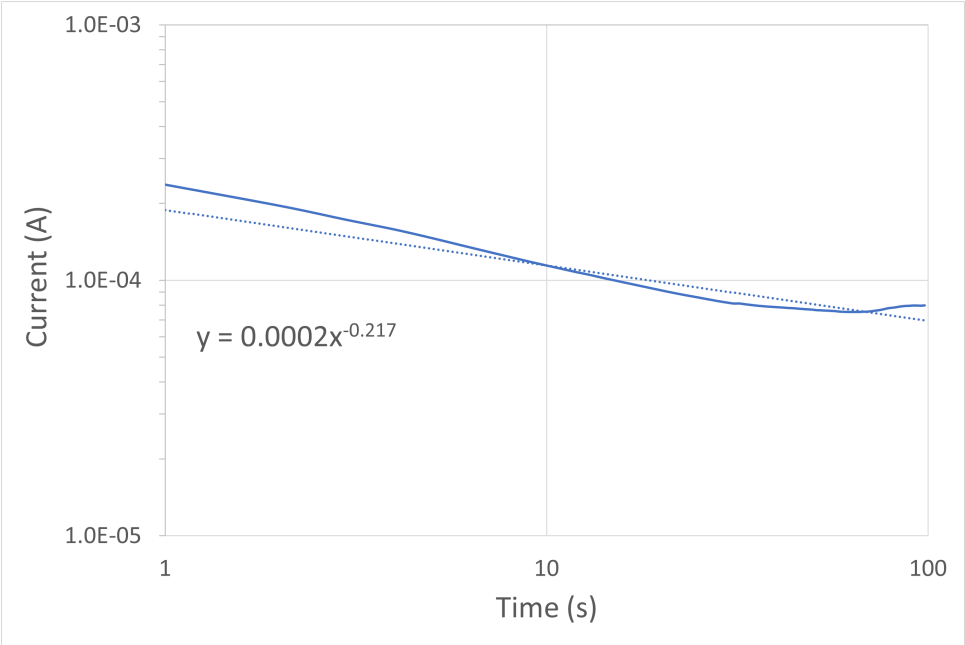

Figure 4.40: First 100 seconds of day five of potentiostatic test of FSP 304L+Mo U-bend sample.

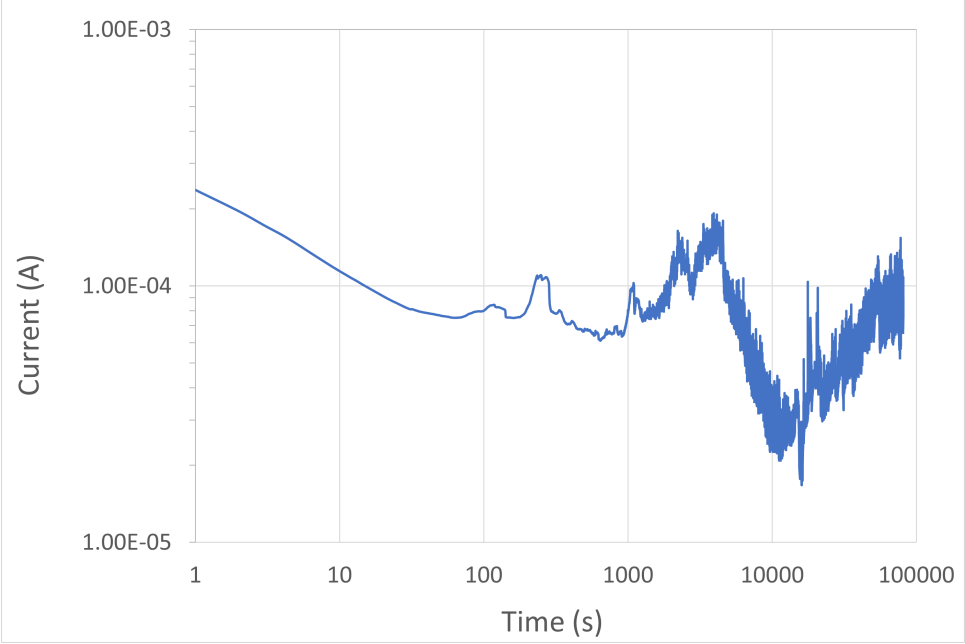

Figure 4.41: Day five of potentiostatic test of FSP 304L+Mo U-bend sample.

Table 4.9: Values for Equation 4.6 taken from potentiostatic analysis.

Sample		Day 1	Day 2	Day 3	Day 4	Day 5
304L	I_o (A)	0.0032	0.0093	0.0032	0.0722	0.0047
	k	-0.516	-0.125	0.0349	-0.594	-0.026
FSP 304L+316L	I_o (A)	0.0041	0.0008	0.002	0.0041	0.00001
	k	-0.116	0.0069	-0.0006	-0.024	0.0079
FSP 304L +Mo	I_o (A)	0.0005	0.0037	0.0021	0.0002	0.0002
	k	-0.953	-0.437	-0.955	-0.422	-0.217

4.3.2.1 Microstructure

Micrographs of the U-bend samples reveal that the 2.5 M H_2SO_4 + 0.5 NaCl solution attacks the surface intergranularly. The most notable changes occur with the 304L samples with large voids visible like in Figure 4.42. During the potentiostatic test, over the course of several minutes, small dust like particulates could be seen falling from the surface of the U-bend sample. These small particulates were not investigated using a scanning electron microscope, but in conjunction with the light optical micrographs, it is believed that these voids are left from grains being intergranularly attacked by the solution. The 304L U-bend sample was the most effected by the potentiostatic test, with large voids visible over the surface. The FSP 304L+316L U-bend samples were less effected, with less of a change to the surface texture. The FSP 304L+Mo U-bend samples were the least effected visually, with almost no change from day 1, Figure 4.43(A), and day 5, Figure 4.43(E). Using the light optical microscope, the surface of the FSP 304L+316L and FSP 304L+Mo samples did not reveal if the samples were intergranular or intragranular attacked. Therefore the samples were analysed with a JEOL JSM-6610LV scanning electron microscope to reveal the surface topology. Upon inspection, it can be seen in Figure 4.45 that the corrosion attack was intergranular. Figure 4.46 reveals an unexpected topography. The surface is dimpled like that of a golf ball with no visible grain boundaries or visable cracking. It appears as though the

sample under went general corrosion because the whole surface has been attacked. Figure 4.47 reveals a smooth surface with occasional pitting but no intergranular attack.

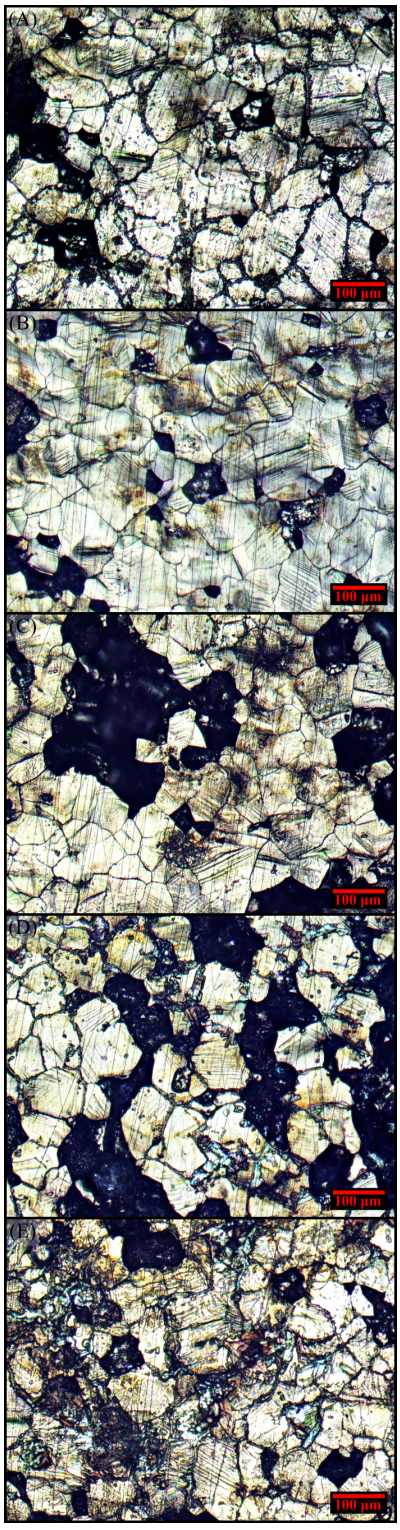

Figure 4.42: Micrograph of 304L U-bend with 0.2 V in 2.5 M H_2SO_4 + 0.5 NaCl. (A): day 1, (B): day 2, (C): day 3, (D): day 4, (E): day 5

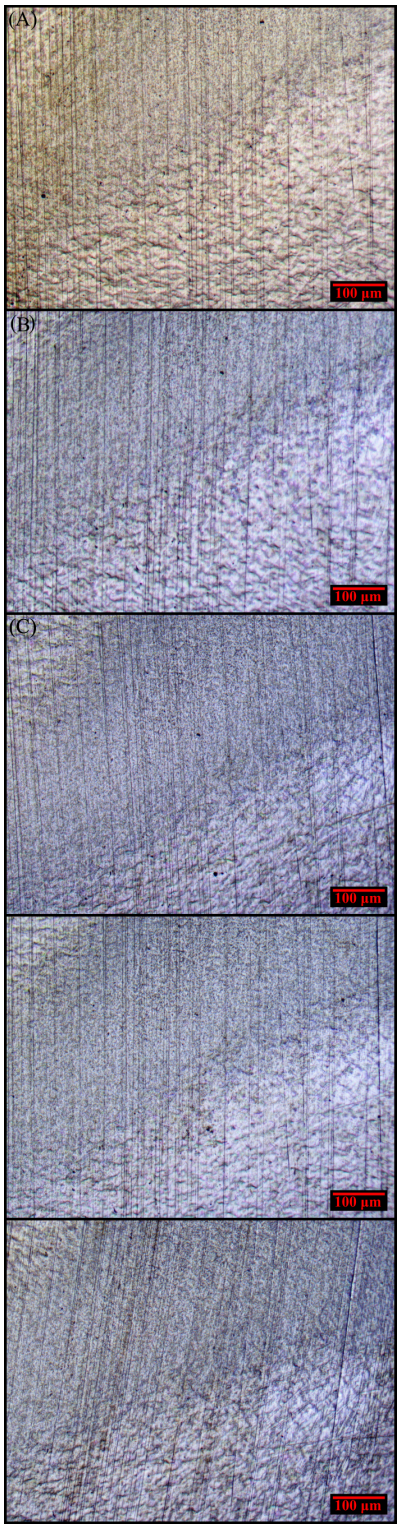

Figure 4.43: Micrograph of FSP 304L+Mo U-bend 0.2 V with in 2.5 M H_2SO_4 + 0.5 NaCl. (A): day 1, (B): day 2, (C): day 3, (D): day 4, (E): day 5

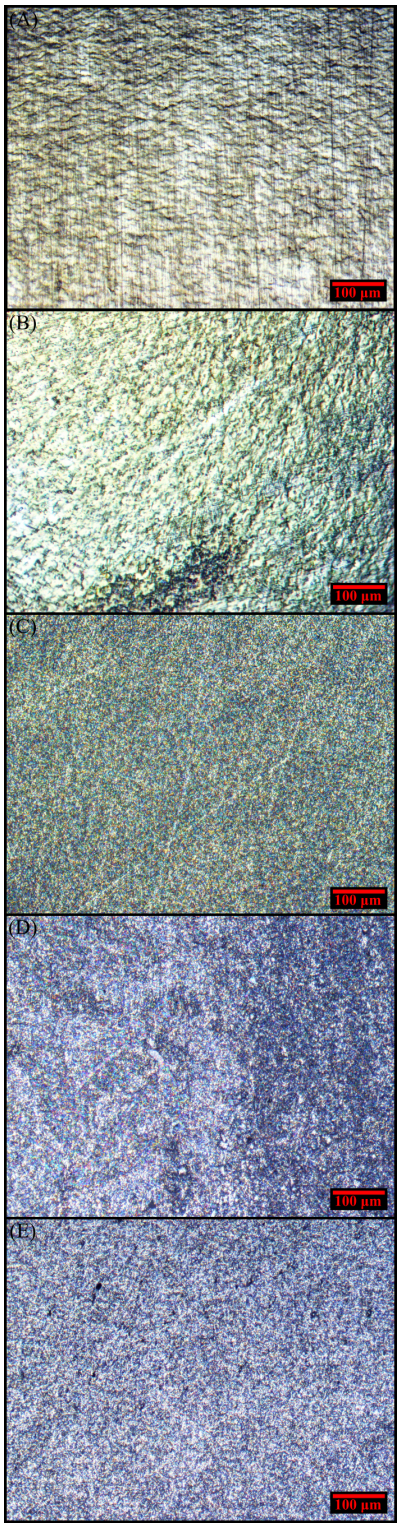

Figure 4.44: Micrograph of FSP 304L+316L U-bend with 0.2 V in 2.5 M H_2SO_4 + 0.5 NaCl. (A): day 1, (B): day 2, (C): day 3, (D): day 4, (E): day 5

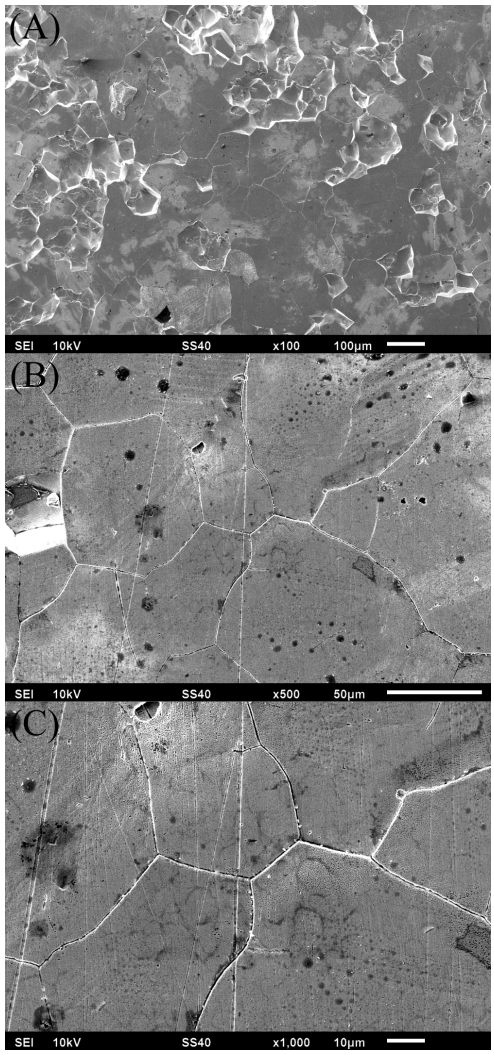

Figure 4.45: Scanning electron image of 304L U-bend sample.

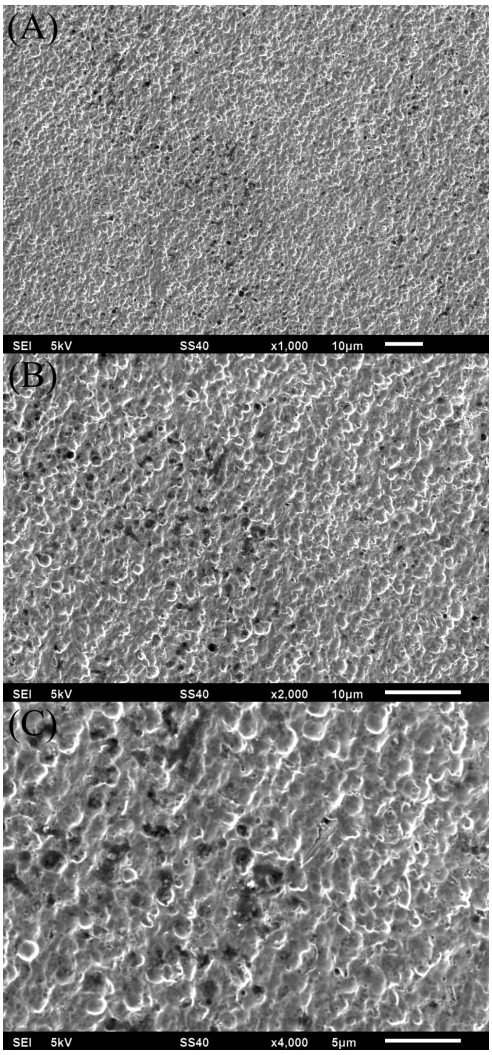

Figure 4.46: Scanning electron image of FSP 304L+316L U-bend sample.

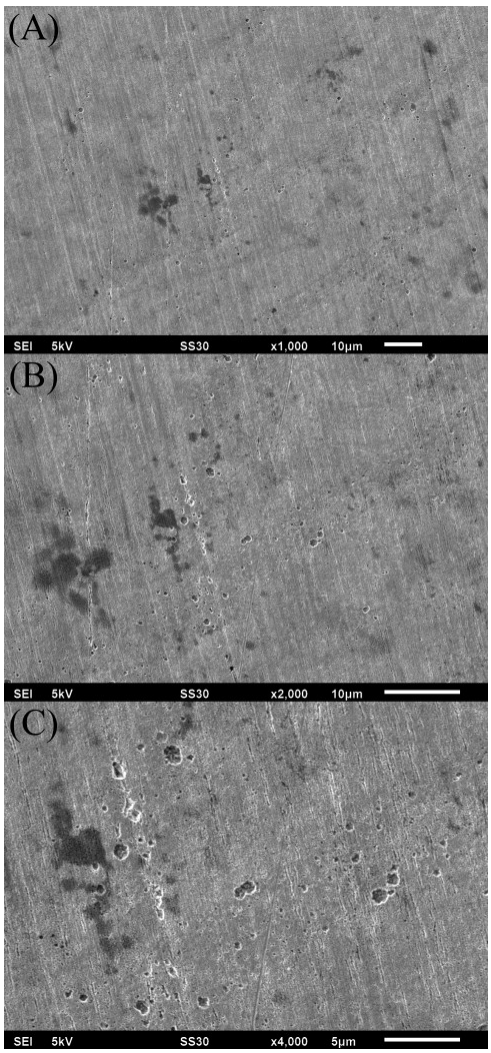

Figure 4.47: Scanning electron image of FSP 304L+Mo U-bend sample.

4.3.3 Grain Size

The application of ASTM E112-96 revealed that the friction stir processed samples had a reduced grain size when compared with the 304L, see Figure 4.10. This is congruent with the results from other research [7], [8], [9].

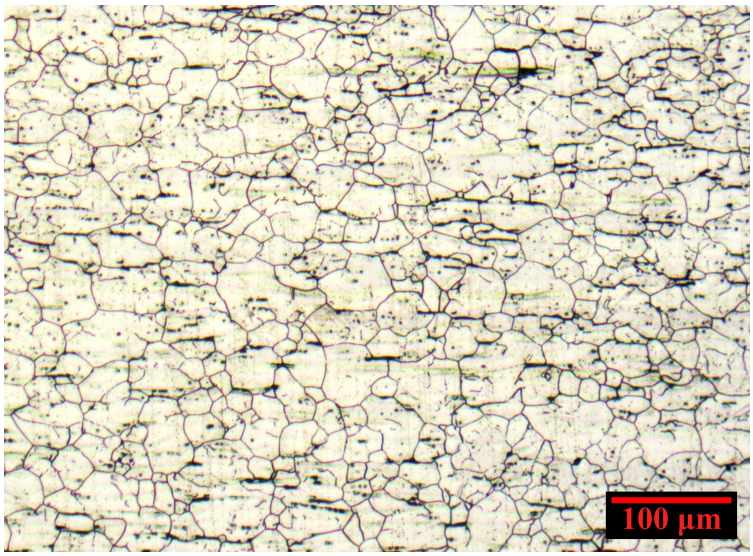

Figure 4.48: Light optical micrograph taken of etched 304L.

Table 4.10: Microstructure details of 304L samples before FSP, after FSP, and FSP with the addition of 316L and molybdenum.

	304L	FSP 304L+316L	FSP 304L+Mo
$\bar{l}$ (μm)	19.60	3.08	5.20
$\bar{d}$ (μm)	22.35	3.45	5.82
s (μm)	$\pm$12.94	$\pm$2.02	$\pm$3.87
95% CI	1.85	0.29	0.46
% RA	8.29	8.38	8.83

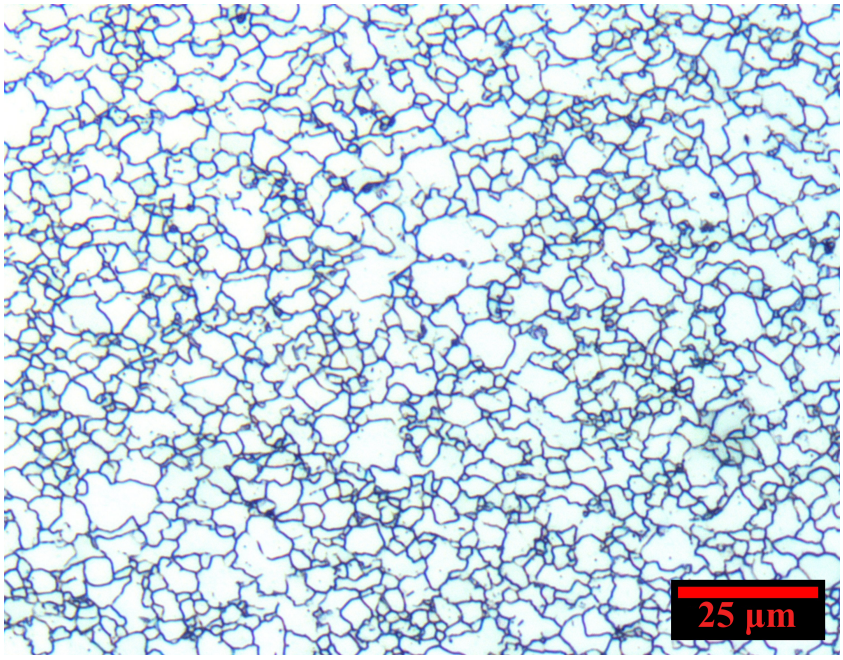

Figure 4.49: Light optical micrograph taken of etched FSP 304L+316L.

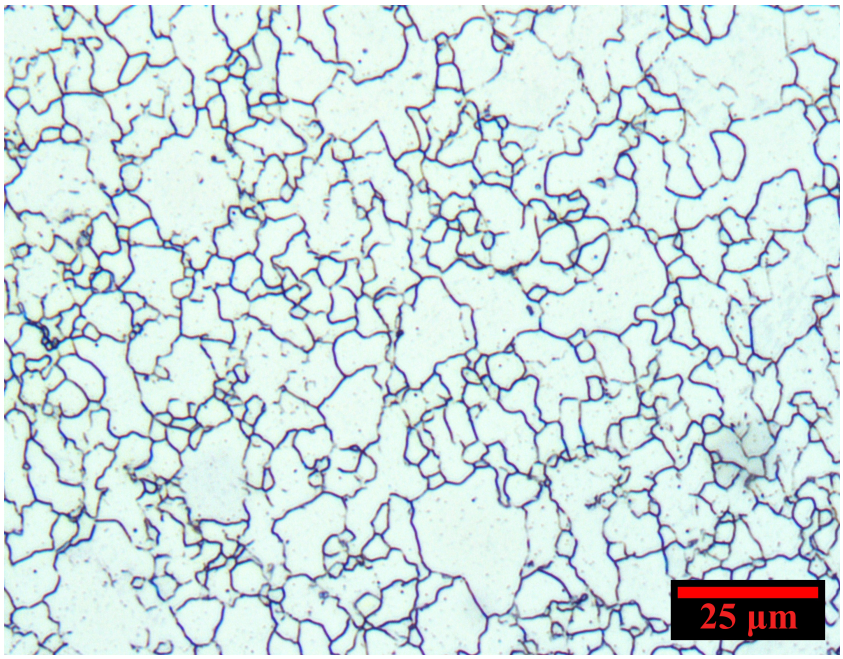

Figure 4.50: Light optical micrograph taken of etched FSP 304L+Mo.

4.3.4 Surface Defects

While polishing the samples, surface artifacts were observed using the optical light microscope. The first artifacts observed were comet tails, as seen in Figure 4.51 and 4.52. The comet tails started to appear during 800 grit portion of the grinding process. Comet tails occur adjacent to inclusions or pores [10] or when an inclusion is pulled out of the sample [11]. Porosity and inclusions are possible with friction stir processing [12] [13] but this is outside the scope of this thesis. The second surface artifact observed was what appeared as small dark spots on the surface of the sample, as can be seen in Figure 4.53. The concentration of surface artifacts varied between samples from only visible with a scanning electron microscope, like Figure 3.22, to visible to the naked eye like in Figure 4.54. Scanning electron microscope and energy dispersive spectroscopy revealed in Figure 4.55 that these dark spots to be evidence of porosity and powder that did not become homogenized with the base metal [14].

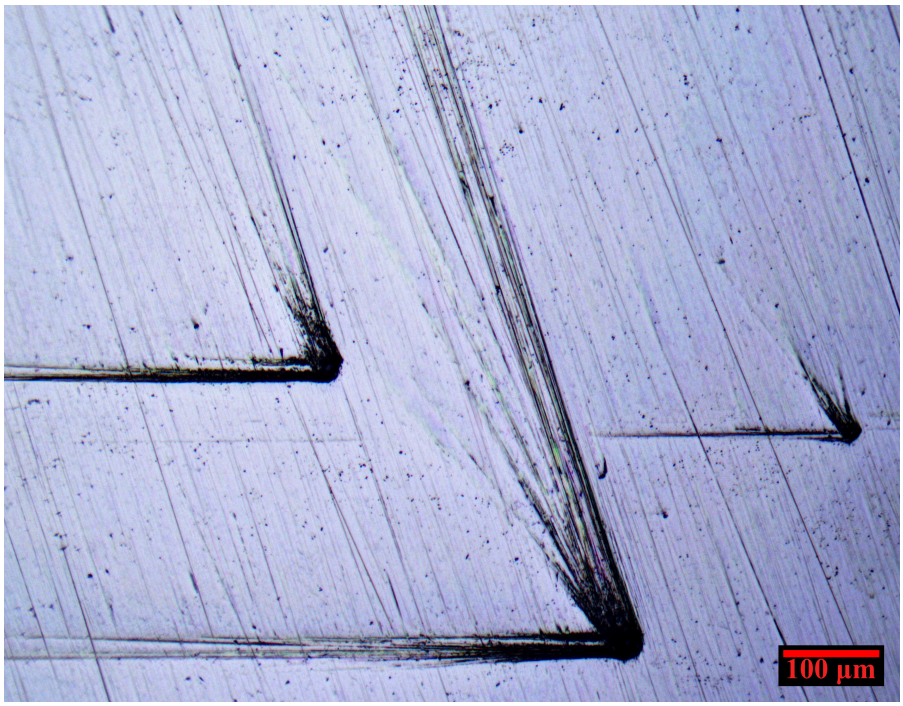

Figure 4.51: Comet tail observed after 800 grit grinding paper using light microscope at 10X

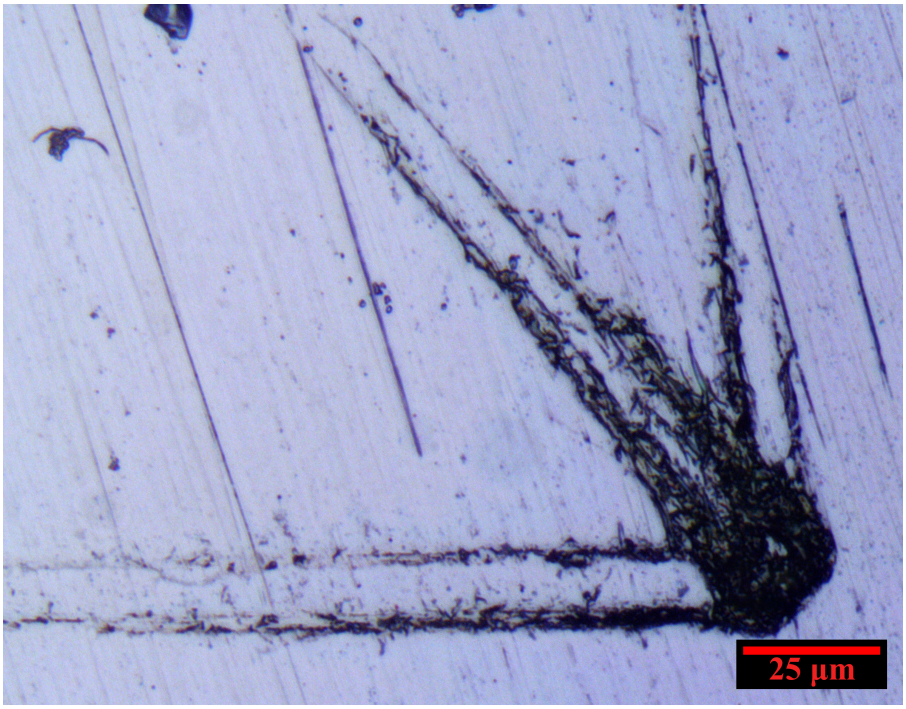

Figure 4.52: Comet tail observed after 800 grit grinding paper using light microscope at 50X

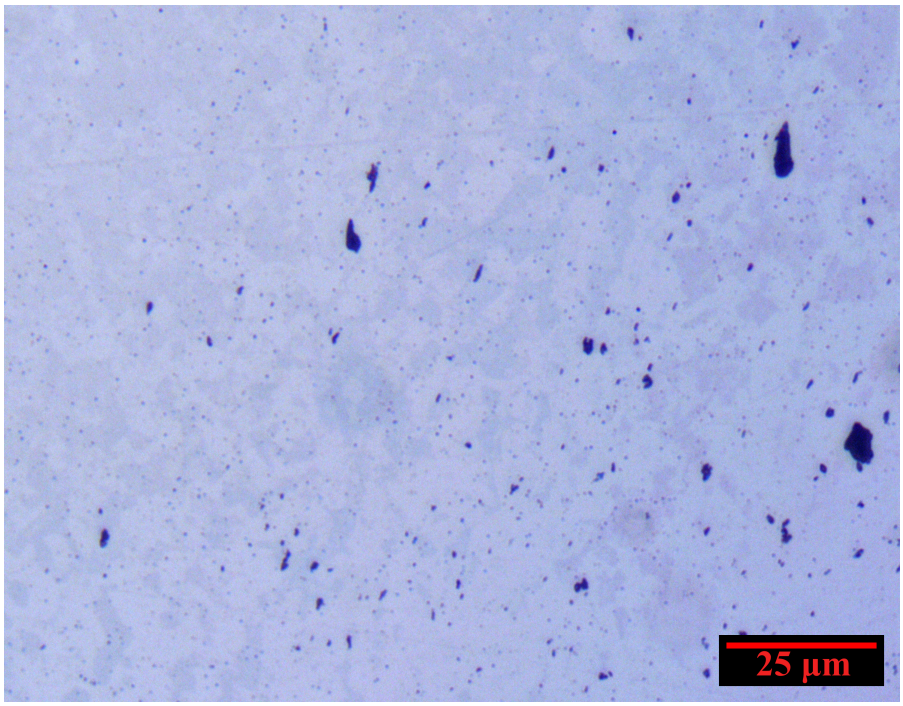

Figure 4.53: Surface artifacts observed in FSP 304L+316L after 1 μm diamond suspension

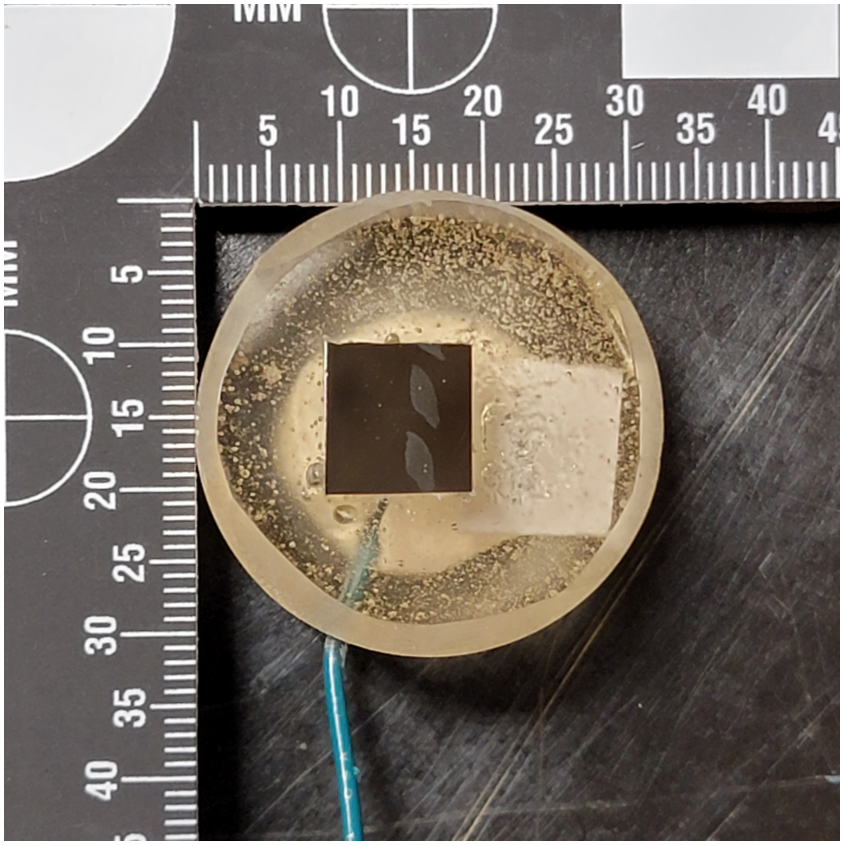

Figure 4.54: Photograph taken of FSP 304L+Mo sample with surface inclusions

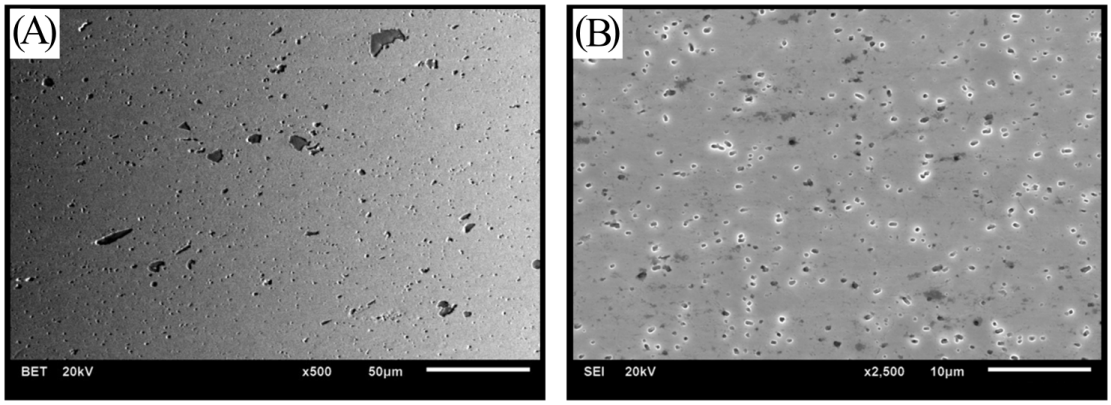

Figure 4.55: Scanning electron image of: (A)The surface of the FSP 304L+316L sample and (B)the surface of the 304L+Mo sample.

4.4 Conclusion

The FSP 304L+316L and FSP 304L+Mo were more noble in the open circuit potential analysis and did not fail in the U-bend test yet the surface crack density was higher in the FSP samples. while crack formation is generally not ideal in a material, this may have relieved stress in the U-bend sample enough to mitigate total failure. The FSP 304L+316L and FSP 304L+Mo were removed from the 2.5 M sulfuric acid + 0.5 M sodium chloride solution intact after 2472 hours. By contrast, the 304L U-bend sample had a low surface crack density with a larger grain size which may have encouraged the catastrophic failure at 267.5 hours. The potentiostatic analysis reveals that the FSP 304L+Mo sample performed best because the average value for I_o is the lowest at 0.00134 A, the average k value is most negative at -0.597, and visual inspection using the SEM reveals the smoothest topography. The FSP 304L+316L sample performed the worst in the potentiostatic test but based on SEM analysis did not suffer as aggressive of corrosion attack as the 304L sample. The 304L sample was the second best in the potentiostatic test but light optical microscope and SEM analysis revealed the samples sustained aggressive intergranular attack from the 2.5 M sulfuric acid and 0.5 M sodium chloride solution. It is unclear why the FSP 304L+316L sample had the worst k value for the potentiostatic test. Based on scanning electron microscopy, the presence of surface defects in the FSP 304L+316L may have attributed to the slower passivation kinetics. Intergranular attack was dominant in the 304L sample with the light optical microscope but a mix of the two types is reasonable to be present in a Fe-Cr alloys. FSP 304L+Mo had an improved passivation constant compared with the other samples.

Bibliography

[1] Tae M Ahn, Greg Oberson, and Sara DePaula. "Chloride-Induced Stress Corrosion Cracking of Austenitic Stainless Steel Used for Dry Storage of Spent Nuclear Fuel". In: *ECS Transactions* 50.31 (May 1, 2013), pp. 211–226. ISSN: 1938-5862, 1938-6737. DOI: 10.1149/05031.0211ecst. URL: https://iopscience.iop.org/article/10.1149/05031.0211ecst (visited on 09/28/2022).

[2] Scott D Cramer and Bernard S. Covino. *ASM Handbook Volume 13B, Corrosion: Materials - ASM International*. Nov. 2005.

[3] A. Abbasi Aghuy et al. "Effect of grain size on pitting corrosion of 304L austenitic stainless steel". In: *Corrosion Science* 94 (May 1, 2015), pp. 368–376. ISSN: 0010-938X. DOI: 10.1016/j.corsci.2015.02.024. URL: https://www.sciencedirect.com/science/article/pii/S0010938X15000992 (visited on 11/07/2022).

[4] Frederick C. Bell and Daniel E. Sonon. "Improved metallographic etching techniques for stainless steel and for stainless steel to carbon steel weldments". In: *Metallography* 9.2 (Apr. 1, 1976), pp. 91–107. ISSN: 0026-0800. DOI: 10.1016/0026-0800(76)90008-2. URL: https://www.sciencedirect.com/science/article/pii/0026080076900082 (visited on 03/11/2023).

[5] *Standard Test Methods for Determining Average Grain Size*. Version E112-96. 1996. DOI: 10.1520/E0112-96R04E01. (Visited on 05/09/2023).

[6] George F. Vander Voort. *Metallography, Principles and Practice*. Google-Books-ID: GRQC8zYqtBIC. ASM International, Jan. 1, 1999. 770 pp. ISBN: 978-1-61503-236-5.

[7] R. S. Mishra and Z. Y. Ma. "Friction stir welding and processing". In: *Materials Science and Engineering: R: Reports* 50.1 (Aug. 31, 2005), pp. 1–78. ISSN: 0927-796X. DOI: 10.1016/j.mser.2005.07.001.

[8] M. W. Mahoney et al. "Properties of friction-stir-welded 7075 T651 aluminum". In: *Metallurgical and Materials Transactions A* 29.7 (July 1, 1998), pp. 1955–1964. ISSN: 1543-1940. DOI: 10.1007/s11661-998-0021-5. URL: https://doi.org/10.1007/s11661-998-0021-5 (visited on 06/17/2023).

[9] Hidetoshi Fujii et al. "Friction stir welding of carbon steels". In: *Materials Science and Engineering: A* 429.1 (Aug. 15, 2006), pp. 50–57. ISSN: 0921-5093. DOI: 10.1016/j.msea.2006.04.118. URL: https://www.sciencedirect.com/science/article/pii/S0921509306005417 (visited on 06/17/2023).

[10] *Metallographic grinding and polishing insight — Struers.com*. URL: https://www.struers.com/en/Knowledge/ (visited on 05/10/2023).

[11] *Grinding and Polishing Guide - Buehler - Metallography Equipment & Supplies for Sample Preparation*. Section: Technical Article. Nov. 15, 2021. URL: https://www.buehler.com/blog/grinding-and-polishing-guide/ (visited on 05/10/2023).

[12] Yousef Imani, M. K. Besharati Givi, and Michel Guillot. "Improving Friction Stir Welding between Copper and 304L Stainless Steel". In: *Advanced Materials Research* 409 (2012). Publisher: Trans Tech Publications Ltd, pp. 263–268. ISSN: 1662-8985. DOI: 10.4028/www.scientific.net/AMR.409.263. URL: https://www.scientific.net/AMR.409.263 (visited on 05/10/2023).

[13] Shubham Verma and Joy Misra. “A Critical Review of Friction Stir Welding Process”. In: Jan. 1, 2015, pp. 249–266. ISBN: 978-3-902734-05-1. DOI: 10.2507/daaam.scibook.2015.22.

[14] Norah Alsairy. “Microstructural Modification and Mechanical Properties Evaluation of an Austenitic Stainless Steel Subjected to Friction Stir Based Repair”. PhD thesis. Idaho Falls, ID, USA: University of Idaho, 2023.

CHAPTER 5

Conclusion

In this thesis, I have reported the results and analyses of a preliminary investigation of friction stir processed techniques as a method for crack repair and fortification against chloride induced stress corrosion cracking. Analysis using cyclic polarization was used to observe that friction stir processing was beneficial at improving corrosion resistance, especially pit nucleation when compared to the 304L base metal. However, the FSP 304L+316L and FSP 304L+Mo samples did not have improved pitting potential when compared to FSP 304L sample. The FSP 304L+316L and FSP 304L+Mo samples did have improved corrosion current and the FSP 304L+Mo had significantly improved linear polarization resistance. U-bend test revealed the FSP 304L+316L and FSP 304L+Mo samples did not fail even after 2472 hours in a 2.5 M sulfuric acid and 0.5 M sodium chloride solution where as the 304L sample failed after 267.5 hours. Light optical microscopy revealed that the FSP samples had higher surface crack densities.The U-bend potentiostatic analysis revealed that the FSP 304L+Mo samples had improved passivation kinetics when compared with the other samples. The U-bend potentiostatic analysis of 304L revealed a strong intergranular attack when examined with optical and scanning electron microscopy. The U-bend potentiostatic analysis of FSP 304L+316L revealed a general corrosion type of attack when examined with the scanning electron microscope. The U-bend potentiostatic analysis of FSP 304L+Mo revealed a relatively smooth topography with evidence of pitting. Surface defects were observed in the FSP 304L+316L and FSP 304L+Mo samples in the form of porosity and powder that was unmixed with the rest of the material.

Future Work

In future work, the parameters of the friction stir process should be examined to determine if there is an ideal technique for mixing additives into Fe-Cr alloys. This line of inquiry will investigate possible reasons and solutions for porosity and unmixed powder. An examination of the limits molybdenum that can be added via friction stir processing would also be of great importance to the research community. This could be done by using pure molybdenum wire in place of sintered 304L+Mo pellets. Investigation into the maximum amount high stacking fault energy can be increased via friction stir alloying.